# Integration and Wireless Control Methods for Micromachined Shape-Memory-Alloy Actuators and their MEMS Applications

by

Mohamed Sultan Mohamed Ali

B. Eng., Universiti Teknologi Malaysia, 2006

M. Eng., Universiti Teknologi Malaysia, 2008

A THESIS SUBMITTED IN PARTIAL FULFILLMENT

OF THE REQUIREMENTS FOR THE DEGREE OF

DOCTOR OF PHILOSOPHY

in

The Faculty of Graduate Studies

(Electrical and Computer Engineering)

THE UNIVERSITY OF BRITISH COLUMBIA

(Vancouver)

July, 2012

© Mohamed Sultan Mohamed Ali (2012)

# Abstract

Bulk-shape memory alloy actuators have great potential to be used in various microdevices. Previous studies show that this material is very attractive due to its very large force, high mechanical robustness with a simple structure and biocompatibility. These properties have resulted in its commercialization for various applications including those in biomedical field. Yet their advantages have not been fully utilized. For example, the commonly used actuation mechanism using Joule heating which requires wired interfaces limits their application especially in those instances where access and space are very limited. In addition, their incompatibility with the standard MEMS fabrication process further limits their potential for use in microscale devices.

This thesis presents a novel technique for the wireless control of shape-memory alloy microactuators and the method for integrating bulk-micromachined shape memory alloy material into the MEMS fabrication process. The wireless control of shape memory alloy actuators using radiofrequency magnetic field wireless heating through resonant planar coils to directly drive the actuator without the use of conditioning circuits is demonstrated. An electroplating bonding technique is developed to integrate the bulk-micromachined shape-memory alloy to the planar heater and the bonding strength is evaluated. A shape-memory alloy microgripper is fabricated and reported using developed actuation and the integration technique. Multiple actuator control is demonstrated using frequency modulated signals and its application in a form a microsyringe employing three actuators is reported. To improve the temporal response of the actuator, the wireless resonant heater circuit is fabricated using a shape-memory alloy to form an out-of-plane spiral coil which acts as the receiver coil as well as the actuator. Wireless displacement control and monitoring is also demonstrated using the fabricated device.

The presented radiofrequency wireless control method also provides a platform to investigate the wireless actuation of the thermal based actuators other than the shape-memory alloy. The reported integration method also provides a means to exploit bulk materials into the MEMS fabrication process.

# Preface

This thesis is based on the contributions that have been reported in the following papers:

**Journal papers:**

1. M.S. Mohamed Ali and K. Takahata, "Frequency-Controlled Wireless Shape-Memory-Alloy Microactuators Integrated using an Electroplating Bonding Process," *Sensors and Actuators A: Physical*, vol. 163(1), pp 363-372, 2010. (Part of Chapter 3)
2. M.S. Mohamed Ali and K. Takahata, "Wireless Microfluidic Control with Integrated Shape-Memory-Alloy Actuators Operated by Field Frequency Modulation" *Journal of Micromechanics and Microengineering*, vol. 21, 075005-1–075005-10, 2011. (Part of Chapter 4)
3. M.S. Mohamed Ali, B. Bycraft, C. Schlosser, B. Assadsangabi, and K. Takahata, "Out-of-Plane Spiral-Coil Inductor Formed using Locally Controlled Bimorph Actuation" *Micro and Nano Letters*, vol. 6 (12), pp. 1016–1018, 2011. (Appendix)
4. M.S. Mohamed Ali, B. Bycraft, Anas Bsoul, and K. Takahata, Radio-Controlled Out-of-Plane Microactuator using Shape-Memory-Alloy Spiral-Coil Inductor, submitted to *Journal of Microelectromechanical System*. (Part of Chapter 5)

**Conference papers:**

1. M.S. Mohamed Ali and K. Takahata, "A Wirelessly Controlled Shape-Memory-Alloy MEMS Gripper Microfabricated using an Electroplating-Based Bonding Process," *Solid-State Sensor, Actuator and Microsystems Workshop (Hilton Head 2010)*, Hilton Head Island, SC, USA, 2010, pp. 396-399. (Part of Chapter 3)
2. M.S. Mohamed Ali and K. Takahata, Selective RF Wireless Control of Integrated Bulk-Micromachined Shape-Memory-Alloy Actuators and Its Microfluidic Application, *Proceeding IEEE MEMS*, Cancun, Mexico, Jan 23-27, 2011, pp 1269-1272. (Part of Chapter 4)

**Book Chapter:**

M.S. Mohamed Ali and K. Takahata, Radio-Controlled Wireless MEMS Actuators and Applications, in *Micro Electro Mechanical System (MEMS): Technology and Applications*, CRC Press, in press. (Part of Chapter 3 and Chapter 4)

In addition, a patent application ("Wireless Microactuators and Control Methods" Application No.: 13/324587) is also filed based on the results reported in this thesis.

Exact quotations from Journal papers 1 and 2, and book chapter may appear in Chapters 1 and 2. Necessary permission has been obtained from the respective publishers to reproduce the reported results in this thesis.

Here, I clarify that I am the principle researcher and main author in all the above mentioned publications. I conducted the literature survey, design, simulations, process development and fabrication. I also prepared the experimental setup and performed all of the measurements.

All the manuscripts were co-authored by my supervisor, Dr. Kenichi Takahata who has guided me in each and every aspect of my research. He provided me with the general idea for my research, and with guidance and continuous input and feedback throughout the research period. He also assisted me in writing the manuscripts.

Journal paper 3 (related to the result reported in the Appendix) has also been co-authored by Brad Bycraft, Colin Schlosser and Babak Assadsangabi. Brad Bycraft and Colin Schlosser have assisted me with the fabrication work, while Babak Assadsangabi has assisted me in the measurements reported in Figure 6 of the Appendix. Brad Bycraft and Anas Bsoul co-authored Journal paper 4 (related to Chapter 5). Brad Bycraft has assisted me with the fabrication work, while Anas Bsoul has assisted me with the simulation results reported in Figure 5.2 (c). These co-authors' work is acknowledged in the respective papers.

# Table of Contents

**Abstract** ........ **ii**

**Preface** ........ **iii**

**Table of Content** ........ **v**

**List of Tables** ........ **viii**

**List of Figures** ........ **ix**

**Acknowledgements** ........ **xvi**

**Dedication** ........ **xvii**

**Chapter 1: Introduction** ........ **1**

1.1 MEMS Actuator ........ 1

1.2 Shape-Memory Alloy ........ 3

1.3 Shape-Memory Alloy Actuators ........ 7

1.4 Wireless Microactuators ........ 8

1.5 Integration of Bulk-Micromachined SMA ........ 10

1.6 Research Objectives ........ 12

1.7 Potential Impact of the Research ........ 13

1.8 Research Methodology ........ 14

1.9 Thesis Overview ........ 18

**Chapter 2: Wireless Power Transfer: Background, Theory and Analysis** ........ **19**

2.1 Introduction ........ 19

2.2 Background ........ 20

2.3 Design and Fabrication of Planar Resonant Circuit ........ 22

2.4 Results ........ 26

2.4.1 Resonant Frequency ........ 26

2.4.2 Coil Resistance ........ 28

2.4.3 Quality Factor ........ 31

2.4.4 Coupling Coefficient ........ 34

2.4.5 Wireless Power Transfer ........ 37
2.4.6 Wireless Heating ........ 41
2.4.5 Distance Characterization ........ 50
2.5 Conclusion ........ 52

**Chapter 3: A Wireless Bulk-Micromachined Shape-Memory Alloy Microgripper and the Integration Method ........ 54**
3.1 Introduction ........ 54
3.2 Working Principle of the Device ........ 55
3.3 Design and Fabrication ........ 56
3.4 Experimental Results and Discussion ........ 61
3.4.1 SMA Phase Transition Characteristics ........ 62
3.4.2 Wireless Actuation Tests ........ 63
3.5 SMA Integration and Characterization ........ 67
3.5.1 Characterization of Bonding Strength ........ 67
3.5.2 Effect of the Silicon Dioxide Layer in Bonding ........ 69
3.6 Conclusion ........ 72

**Chapter 4: Selective Wireless Control of Shape-Memory Alloy Actuators using Frequency Modulation and its Microfluidic Application ........ 73**
4.1 Introduction ........ 73
4.2 Device Principle and Design ........ 74
4.3 Device Fabrication ........ 77
4.4 Experimental Results and Discussion ........ 80
4.4.1 Selectable Activation of Wireless Heater Array ........ 81
4.4.2 Heat Distribution in the SMA Cantilever Actuator ........ 84
4.4.3 Wireless Test for the Microsyringe Device ........ 87
4.5 Conclusion ........ 90

**Chapter 5: Radio-Controlled Out-of-Plane Microactuators using Shape-Memory Alloy Spiral-Coil Inductor ........ 91**
5.1 Introduction ........ 91

5.2 Working Principle of the Device ..... 92
5.3 Device Fabrication ..... 96
5.4 Experimental Results and Discussion ..... 101
5.4.1 Characteristics of SMA Spiral-Coil Inductor ..... 101
5.4.2 Wireless Tests of the SMA Actuator ..... 102
5.4.3 Wireless Displacement Monitoring ..... 109
5.4.4 Coil Optimization ..... 112
5.5 Conclusion ..... 114

**Chapter 6: Conclusion ..... 116**
6.1 Contributions ..... 116
6.2 Future Work ..... 120

**Bibliography ..... 121**
**Appendix A: Out-of-Plane Spiral-Coil Inductor Self-Assembled By Locally Controlled Bimorph Actuation ..... 138**
**Appendix B: Parameters used for $T_f$ Calculation in Chapter 2 ..... 149**

# List of Tables

Table 1.1 Actuation mechanism, working principles and work density ............ 2
Table 1.2 Actuation mechanism, working principles and work density ............ 4
Table 1.3 Alloys with shape-memory effects and their temperature properties ............ 6
Table 1.4 Polymer based bonding properties ............ 11
Table 2.1 Parameters for coils with different number of turn ............ 26
Table 2.2 Parameters for coils with different fill ratio ............ 27
Table 2.3 Electrical parameters for the coils with different number of turns ............ 31
Table 2.4 Electrical parameters for the coils with different fill ratios ............ 31
Table 2.5 Transmitter coil parameters ............ 35
Table 2.6 Numerical values used for heat flow calculation ............ 45
Table 2.7 Numerical values used for steady state temperature $T_f$ calculation ............ 48
Table 3.1 The dimensions of the gripper structures ............ 57
Table 4.1 Measured actuator response at 0.15 and 0.3 W power levels ............ 85

# List of Figures

Figure 1.1 Changes in the crystalline orientation of the SMA at different phases .............. 4
Figure 1.2 The phase transformation and hysteresis properties of the SMA ....................... 5
Figure 2.1 Working principle of wireless power transmission between two coils ............ 21
Figure 2.2 LC resonant circuit ........................................................................... 23
Figure 2.3 Square type spiral planar coil .............................................................. 23
Figure 2.4 Fabrication process of LC circuit ......................................................... 25
Figure 2.5 Fabricated LC circuits ........................................................................ 25
Figure 2.6 Changes in $f_r$ for coil with different numbers of turns and a comparison between the measured and theoretical values ................................................ 27
Figure 2.7 Changes in $f_r$ for coil with different fill ratios and a comparison between the measured and theoretical values ..................................................... 28
Figure 2.8 Frequency-dependent characteristic of the coils with different number of turns ..................................................................................................... 29
Figure 2.9 Frequency-dependent characteristic of the coils with different line width ....... 30
Figure 2.10 Q-factor of fabricated LC resonant circuits with different number of turns ..... 32
Figure 2.11 Q-factor of fabricated LC resonant circuits with different line width .............. 33
Figure 2.12 Coupling coefficient between transmitter coil and the receiver coils with different numbers of turn .................................................................... 35
Figure 2.13 Coupling coefficient between transmitter coil and the receiver coils with different line width ........................................................................... 36
Figure 2.14 Voltages measured in the wirelessly powered receiver coil with different numbers of turns; (a) voltage vs. time and; (b) peak voltage ($v_p$) vs. number of turns ....................................................................................................... 38
Figure 2.15 Voltage measured in the wirelessly powered receiver coil with different fill ratios; (a) voltage vs. time and; (b) peak voltage ($v_p$) vs. line width ................ 38
Figure 2.16 Power transfer efficiency for receiver coil with different number of turns ...... 40
Figure 2.17 Power transfer efficiency for receiver coil with different fill ratio .................. 41
Figure 2.18 Heat loses at the planar heater ........................................................... 42
Figure 2.19 Comparison of heat flow component in the planar heater ............................... 46

Figure 2.20 Steady state temperature of coils with different numbers of turns ..................48

Figure 2.21 Steady state temperature of coils with different line widths............................49

Figure 2.22 Coupling coefficient vs. distance of the transmitter and the receiver coil........51

Figure 2.23 Calculated and measured efficiency and measured voltage vs distance...........51

Figure 2.24 Steady state temperature of the coils when distance increased........................52

Figure 3.1 (a) Wirelessly controlled SMA micro-gripper and (b) working principle of the device ..........................................................................................................55

Figure 3.2 (a) The SMA gripper design and (b) sample layout of the LC circuit design...57

Figure 3.3 Fabrication process flow(cross-sectional view except steps 6 and 7)...............58

Figure 3.4 (a) Samples of the LC resonant circuit fabricated using copper-clad PI film, and (b) an SMA gripper component fabricate with μEDM (prior to separation from the original sheet)........................................................................59

Figure 3.5 Fabrication results for device-1 (4-mm-long gripper): (a) Gripper beams split using μEDM with a close-up showing the inner sidewall of the beam; (b) the SMA pad bonded by electroplated copper; (c) overall shape of a fabricated device ..........................................................................................................61

Figure 3.6 Measured heat flow vs. temperature for the SMA material used for the device fabrication .....................................................................................................62

Figure 3.7 A set-up for wireless actuation tests ................................................................63

Figure 3.8 Measured circuit temperature and gripper openings vs. field frequency (inset images show tip openings of the gripper at corresponding frequencies ...........64

Figure 3.9 Measured circuit temperature and gripper actuation with a temporal application of an external RF magnetic field whose frequency was aligned to the resonant frequency of the circuit ........................................................................65

Figure 3.10 Manipulation of CNT forest ($f_m$ and $T$ in each image are the field frequency and the circuit temperature, respectively): (a) Approaching the forest; (b) tips opened by tuning $f_m$ closer to the device's resonant frequency of 140 MHz; (c) making contact with the forest, and the tips closed by shifting $f_m$ to 150 MHz; (d) gripped part of the forest pulled; (e) the forest part continues to be pulled; (f) gripper holds the separated forest part ........................................................66

Figure 3.11 Measurement of shear bonding strenth: (a) Cross-sectional view of the measurement set-up; (b) layout of SMA samples used for the measurement...68

Figure 3.12 Measured shear forces vs. displacement for type-A (with $SiO_2$ layer) and type-B (without the layer) samples, showing the shear strengths calculated using the bonding surface area of 0.304 $mm^2$ ........ 69
Figure 3.13 SEM images of the broken interface in a type-B sample: (a) The backside of the SMA showing the bowl-like electroplated copper structure grown from the edges of the perforation narrowing the opening; (b) the electroplated copper bump structure formed on the copper-clad layer underneath the bowl-like structure in (a) ........ 70
Figure 3.14 Cross-sectional diagram of copper structures in (a) the type-A sample (with $SiO_2$ layer) and (b) the type-B sample (without the layer) formed by the electroplating bonding process ........ 71
Figure 3.15 Optical images of the broken interface in a type-A sample: (a) $SiO_2$ surface on the SMA showing that the portion of copper-clad layer bonded to the SMA through the copper structure electroplated in the perforation came off (together with some parts of PI) with the SMA when bonding failed; (b) the copper-clad layer where the failure occurred showing the PI surface exposed ........ 71
Figure 4.1 Working principle: In this example, Actuators-2 and -3 are selectively activated by modulating the field frequency ($f_M$) to the resonant frequencies of the two wireless heaters ($f_{R2}$ and $f_{R3}$) coupled with the actuators ........ 74
Figure 4.2 (a) The microsyringe/injector design; (b) A COMSOL model of the SMA actuator showing an approximate displacement of 308 μm at the free end due to the force provided by a 3.5-μm-thick $SiO_2$ compressive layer on the backside of the SMA, indicating the space created underneath the actuator large enough to accommodate the 130-μm-thick parylene reservoir ........ 76
Figure 4.3 Cross sectional view of the fabrication process for (a) wireless resonant circuit (steps 1-3), reservoir formation (step 4), and SMA actuator assembly; (b) the SMA actuator component ........ 78
Figure 4.4 Fabrication results: (a) Sacrificial photoresist mold patterned for the reservoir, and copper bonding pads for the SMA actuator assembly; (b) SMA component fabricated by wet etching and μEDM; (c) fabricated device with close-up of the parylene reservoir ........ 80

Figure 4.5 Experimental setup for wireless testing of the fabricated devices .................... 81

Figure 4.6 (a) Array of four wireless heaters; (b) Measured resonant frequencies of the four heaters .......................................................................................... 82

Figure 4.7 (a) IR image showing selective wireless activation of Heaters-2 and -4; the image was captures at the 8th second after the activation. (b) Temperature distribution accross the array of the four heaters along the line A-A' indicated in figure 4.7(a)........................................................................................ 83

Figure 4.8 IR image of the SMA cantilever actuator with the wireless heater captured at the 13th second after the heater activation ....................................................... 84

Figure 4.9 Measured temporal changes in the temperature of the SMA cantilever actuator at the four points (Figure 4.8) when the heater is wirelessly resonated with RF output power of (a) 0.15 W and (b) 0.3 W. (c) Temporal changes in temperature gradients between the bonding cavity (point 1) and the free end of the cantilever (point 4) for the 0.3-W and 0.15-W cases obtained from the results in Figures 4.9(a) and 4.9(b) .................................................................. 86

Figure 4.10 Side views of the SMA cantilever actuator in (a) the inactive state and (b) the active state showing the SMA squeezing the reservoir.................................... 87

Figure 4.11 pH changes and released amounts of pH buffer (measured and calculated) vs. actuators activated ......................................................................................... 89

Figure 5.1 (a) Conceptual diagram and working principle of the 3D SMA spiral-coil actuator; (b) bimorph actuation of a single segment of the coil; and (c) additive height gain from two consecutive segments of the coil .................................... 93

Figure 5.2 (a) Design of the SMA actuator showing the backside; (b) design of the SMA actuator showing the front side; (c) a FEA result showing an out-of-plane displacement of 492 μm at room temperature, obtained with a model that defines a 3.5-μm-thick $SiO_2$ layer deposited at 420 °C and patterned............. 95

Figure 5.3 Fabrication process; (a) coil formation in SMA sheet using $\mu$EDM; (b) $SiO_2$ layer deposition on both sides; (c) bottom $SiO_2$ layer patterning; (d) top $SiO_2$ layer patterning; (e) SU-8 coating and patterning; (f) sacrificial photoresist patterning; (g) Cr/Cu seed layer deposition; (h) photoresist mold patterning; and (i) Cu electroplating and seed layer and photoresist removal .................... 97

Figure 5.4 (a) EDMed SMA spiral coil and (b) SMA coil after backside $SiO_2$ reset layer have been patterned (before top side $SiO_2$ layer patterned) ............................. 98

Figure 5.5 Fabrication results; (a) SEM image of the 3D SMA coil and a close-up view of the center of the coil; (b) SEM image of the $SiO_2$ reset layer patterned on the backside of the coil with a close-up view; (c) optical image of the backside of the device in its planar state prior to releasing from the base; (d) optical image of the front side of the released SMA actuator showing its 3D shape ........... 100

Figure 5.6 Inductance and Q-factor of the fabricated SMA spiral coil measured for its planar and 3D states as a function of frequency ........................................... 101

Figure 5.7 Experimental set-up used for wireless actuation tests .................................. 103

Figure 5.8 Measured actuator's temperature and displacement vs. $f_M$ ............................ 104

Figure 5.9 Measured $f_R$ of the SMA LC tank at the planar and 3D states ........................ 105

Figure 5.10 Measured force generated by each of the SMA and $SiO_2$ layers vs. $f_M$ (inset images show the set-ups used for both measurements) ................................ 106

Figure 5.11 Measured actuator's temperature and displacement caused by repeated excitations of the actuator implemented using an RF field at $f_M = f_R$ ............ 108

Figure 5.12 IR images of the actuator; (*a-c*) during heating cycle when an RF field with $f_M$ = 231 MHz and 1-W power is applied; (*d-f*) during cooling cycle after the full actuation ........................................................................................ 109

Figure 5.13 Measured $f_r$ vs. out-of-plane displacement when $f_m$=231 MHz ..................... 110

Figure 5.14 Wireless resonant tracking when $f_m$= 180 MHz, 200 MHz and 225MHz ...... 111

Figure 5.15 A SMA coil coated with Cu ......................................................................... 113

Figure 5.16 Electrical characterization of SMA coil before and after Cu layer coating; (a) resistivity measurement and (b) L and Q-factor measurement ...................... 114

Figure A1 Formation of 3D spiral-coil inductor; (a) Overall structure and displacement; (b) Bimorph actuation of single segment; (c) Additive height gain from consecutive segments of the microcoil ........................................................ 140

Figure A2 Device layout and actuation behavior; (a) Design of the 3D bimorph coil; (b) FEA result showing a ~520-μm out-of-plane displacement at 600 °C provided by Cr stress layer patterned on Cu coil; (c) Stress-strain relationship of the coil material at different $T_H$ values.................................................................... 141

Figure A3 Fabrication process; (a) $SiO_2$ deposition; (b) Cr/Cu seed layer deposition; (c) Electroplating of thick Cu layer; (d) Coil formation; (e) Sacrificial etching of $SiO_2$ and Cr layers (cross sectional view); (f) Cr deposition and patterning .. 143

Figure A4 Fabricated sample device; (a) Cu coil formed by μEDM; (b) Cr stress layer patterned on the Cu coil prior to annealing process; (c) SEM image of the Cu-Cr bimetallic coil showing its 3D shape resulted by annealing at 800 °C with a close-up image ........ 144

Figure A5 Thermal dependence of 3D coil formation; (a) Fabricated coils processed at four different $T_H$ levels showing varying heights; (b) Measured out-of-plane displacement and inductance of the coils as a function of $T_H$ ........ 145

Figure A6 Measured frequency dependence; (a) Inductance and (b) Q-factor ........ 146

# Acknowledgements

I am greatly indebted to Allah (Pure and Exalted is He) on His mercy and blessings in making this research successful.

I would like to express my deepest gratitude and thanks to Professor Kenichi Takahata, my honourable supervisor, for giving me the opportunity to work in his wonderful research group. His continuous guidance, committed support and invaluable advice throughout my studies have made the completion of this work possible. His enthusiasm and hard work caused me to awake every day with enthusiasm for what I was to do next. I have learned a great deal from him on every aspect of academics including teaching, research, manuscript writing, grant applications and management skills and I hope to learn much more from him.

I sincerely thank all the professors and lecturers who have taught me for their invaluable lessons. I am indebted to WangNing Yuan for all his support in my courses and research throughout my PhD studies. I would also like to thank Brad Bycraft and Colin Schlosser for their assistance in my research work. My deep appreciation goes to Mario Beaudoin and Alina Kulpa for their feedback on and help with my fabrication work.

Sincere thanks to my qualifying, departmental and university exam committee members: Professors David Michelson, John Madden, Boris Stoeber, Edmund Cretu, Shahriar Mirabbasi, Peyman Servati, Alireza Nojeh, Mu Chiao, Robert Rohling and Bernard Laval. Also thanks to the external examiner, Prof. Karl Böhringer from University of Washington for his valuable comments.

I would like to acknowledge the financial support of the Ministry of Higher Education of Malaysia and the Universiti Teknologi Malaysia. Also thanks to CMC Microsystems for their financial support for my fabrication works.

In addition, I would also like to thank all of my friends: Anas Bsoul, Tanveer Salleh, Dan Brox, Masoud Dahmardeh, Babak Assadsangabi, Muntakim Anwar and Gudivada Venkada Thulasi Prasad: Thank you for sharing with me your useful ideas and information and offering moral support during the course of my studies.

Last but not least, I would like to express my sincere appreciation and gratitude to my father, my wife Rosniza Wati Said and my daughters Aliya Zahirah, Amira Safia and Anisa Afia who are always there for me when it matters the most.

# Dedication

***To my family...***

# Chapter 1

# Introduction

Microactuators are used in the microelectromechanical system (MEMS) to generate mechanical motion that can be utilized to perform a specific task. Microactuators have been successfully applied to various devices such as radio frequency (RF) switches [1], inkjet heads [2, 3] and digital micromirror devices [4]. Their potential to operate in a very limited space, with very limited access has attracted tremendous interest in the biomedical field and has been successfully engaged for use in surgical tools [5, 6], drug delivery devices [7] and artificial organs [8].

In this chapter, various actuation mechanisms in MEMS are discussed, including their advantages and disadvantages. Since this research is related to the shape-memory alloy (SMA) actuators, their advantages, working principles and the actuation mechanisms are reported in detail. The wireless actuation method of the SMA and the use of the RF magnetic field to control actuation are discussed. In addition, the method for integration of the bulk-micromachined SMA into MEMS fabrication is also presented. At the end of this chapter, the research objectives, methodology and overview of this thesis are discussed.

## 1.1 MEMS Actuator

MEMS actuators offer various actuation mechanisms that can be classified into several categories including thermal, electrostatic, magnetic, piezoelectric, and SMA actuations. Table 1.1 presents a brief review of the different actuation mechanisms of MEMS actuators and their work density.

**Table 1.1**: Actuation mechanism, working principles and work density [9].

| Method | Principle | Work Density (J/m$^3$) |
|---|---|---|
| Electrostatic | Attractive forces between two plates with different electrostatic charges | ~$10^5$ |
| Piezoelectric | An electrical field leading to mechanical deformation | ~$1.2 \times 10^5$ |
| Magnetic | Interaction between magnetic fields | ~$4 \times 10^6$ |
| Thermal | Different CTEs of two materials | ~$5 \times 10^5$ |
| SMA | Crystal phase transformation with macroscopic shape change | ~$10^7$ |

In microsystems, the electrostatic actuation principle is often favored [10] due to its simple structure, minimal energy loss and compatibility with integrated circuit processes [11, 12]. However, its stroke is usually small [13] and a very high voltage is required over narrow gaps between its electrodes which limits the application of the device. Moreover, its high voltage requirement reduces the lifetime of the actuator due to the side effects of the dielectric charging [14] and possible sparks during actuation [15].

The piezoelectric actuator is based on the mechanical deformation of the piezoelectric material when an electric field is applied which leads to the actuation. The piezoelectric actuator is well known for its high-force potential and energy density, compactness, fast dynamic response time, repeatability, low input power and low driving voltage [16]. Despite its advantages, integration of piezo material is challenging because of the need for its high temperature thermal processing. In addition, the actuation range is very small, which makes the piezoelectric actuator often undesirable [17].

Magnetic actuators utilize the interaction of the actuator with the magnetic field generated by permanent magnets or coils. An electromagnetic principle has the advantage of a large

force, high frequency and low driving voltage [18]. It also can be operated in a liquid because of the non-existence of an electric charge [19]. However, process and material compatibility, and the integration of the magnetic material into the overall fabrication process are common issues when one wishes to employ this actuation principle.

The desirable property of thermal actuation is the simplicity of the fabrication method and its large displacement. However, in general, thermal actuation tends to have higher power consumption and a slow response time. It is also very sensitive to environmental influences. One of the most common thermal actuator types is the bimorph, which utilizes the difference in the coefficient of thermal expansion (CTE) of two different materials for actuation. The displacement can be determined by choosing an appropriate CTE combination and also by controlling the temperature. The SMA actuator is one of the thermal actuators that undergoes phase changes as the temperature changes and causes the macroscopic deformation of the actuator. The SMA actuators posses the highest degree of work density from among the MEMS actuators as described in Table 1.1. The SMA's working principle is discussed in the next section.

## 1.2 Shape-Memory Alloy

The actuation of the SMA basically involves the straightforward principle of shape-memory effects. The SMA exhibits characteristic shape transformations when within particular temperature ranges. SMAs undergo crystal transformations or atomic rearrangements when materials are heated or cooled to their austenitic and martensitic phase transformation temperatures, respectively [20]. Their material properties differ in these two phases in terms of their electrical resistivity, Young's modulus, coefficient of thermal expansion (CTE), and thermal conductivity as described in Table 1.2.

**Table 1.2**: SMA properties at martensite and austenite phases.

| Property | Martensite Phase | Austenite Phase |
|---|---|---|
| Young's Modulus (GPa) | 40 | 75 |
| Thermal Expansion (μ/°C) | 6.6 | 11 |
| Thermal Conductivity (W/m °C) | 18 | 16.3 |
| Electrical Resistivity (μ Ω-cm) | 76 | 82 |

At the martensite phase, the material's less symmetric atomic structure makes it more flexible and thus more easily deformable. Following distortion of the crystalline orientation of the material, its original shape can be recovered by heating it to higher than the austenite phase temperature, driving the molecular rearrangement to construct its original cubic symmetric shape. Figure 1.1 shows a simplified illustration of the changes in the crystalline form of the SMA that result in the shape-memory effects at different phases.

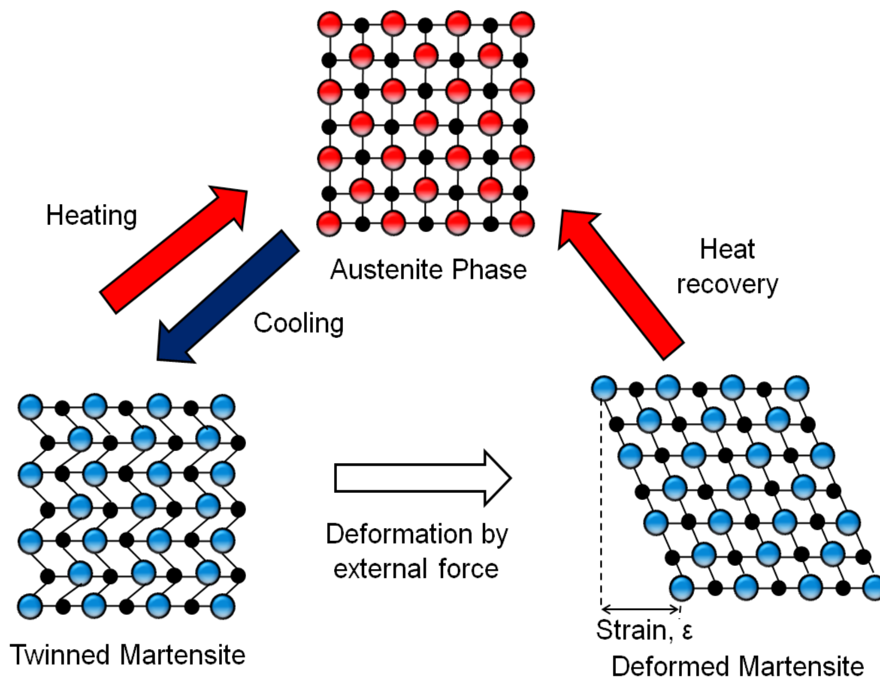


**Figure 1.1**: Changes in the crystalline orientation of the SMA at different phases.

This material is rigid, hard and difficult to deform when it is hot. When the material undergoes a cooling process to below its martensite phase transformation temperature and no external force has been applied, the physical shape of the material will be the same as that in the hot austenite phase shape. However, the atomic layer will tilt in alternating directions between each layer [21]. This state is known as twinned martensite, and the SMA can be deformed by applying an external force or by using the bias spring effect to achieve reversible motion [22]. There are several phase transformation temperatures that need to be considered in the selection of the SMA depending on their applications. Figure 1.2 shows the phase transformation and the hysteresis property of the SMA.

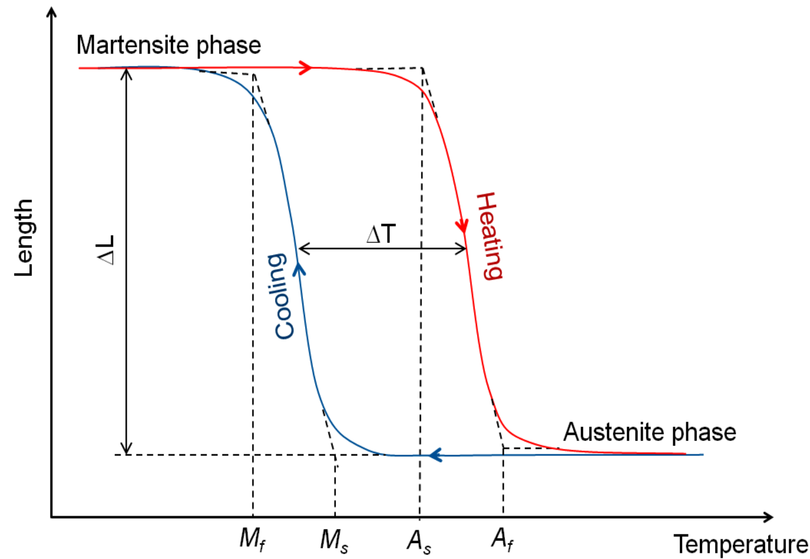


**Figure 1.2**: The phase transformation and hysteresis properties of the SMA.

During the shape recovery process, transformation from the martensite cold state to the austenite hot state commences at the austenite starting temperature, $A_s$, and ends at the austenite finishing temperature, $A_f$. On the other hand, the transformation from the hot austenite phase to the cold martensite phase starts at the martensite starting temperature, $M_s$, and ends at the martensite finishing temperature, $M_f$. Another important parameter in the

phase transformation of the SMA is the hysteresis, Δ*T*, between the phases. Hysteresis is often unfavorable in SMA actuations as it delays the phase change from martensite to austenite and vice versa [23].

The transformation phase temperature of the SMA depends on its material composition. The SMA encompasses few elements. The composition level between these elements will essentially determine the transformation temperature. Thus, the composition can be adjusted in order to achieve the specific transformation temperature. This offers great flexibility and a wide range of options when applying SMA to various applications depending on their suitable temperature range. Table 1.3 shows different types of SMAs and their properties. Among them, Cu based SMA and a NiTi alloy, known as Nitinol, have been practical options for most engineering uses as others involve very expensive elements such as Au, Pt and Cd.

**Table 1.3**: Alloys with shape-memory effects and their temperature properties [24].

| Aloy | Composition | Transformation temperature range (°C) | Transformation hysteresis (°C) |
|---|---|---|---|
| AgCd | 44 - 49 at % Cd | -190 ~ -50 | ~ 15 |
| AuCd | 46.4 - 50 at % Cd | 30 ~ 100 | ~ 15 |
| CuAlNi | 14 - 14.5 wt % Al<br>3 - 4.5 wt % Ni | -140 ~ 100 | ~ 35 |
| CuSn | ~ 15 at % Sn | -120 ~ 30 | |
| CuZn | 38.5 - 41.5 wt % Zn | -180 ~ -10 | ~ 10 |
| CuZuX (X=Si/Sn/Al) | few wt % X | -180 ~ 200 | ~ 10 |
| InTl | 18 - 23 at % Tl | 60 ~ 100 | ~ 4 |
| NiAl | 36 - 38 at % l | -180 ~ 100 | ~ 10 |
| NiTi | 49 - 51 at % Ni | -50 ~ 110 | ~ 30 |
| FePt | ~ 25 at % Pt | ~-130 | ~ 4 |
| MnCu | 5 - 35 at % Cu | -250 ~ 180 | ~ 25 |
| FeMnSi | 32 wt % Mn, 6 wt % Si | -200 ~ 150 | ~ 100 |

*wt = weight, at = atomic

Nitinol has been the most favorable type employed for biomedical applications due to its biocompatible properties, and has been utilized in various biomedical applications such as stents, orthodontics and catheters [25]. Due to the high demand on Nitinol type SMAs, this material is commercially available in various forms including those of tubes, sheets and wires.

## 1.3 Shape-Memory Alloy Actuators

SMA actuators in MEMS area are usually fabricated in two different forms: thin film SMA actuators [26-32] and bulk-micromachined SMA actuators [33-36]. Thin film SMA actuators are often formed through the sputter deposition process. SMA films undergo crystallization and shape setting through heat treatments. The thickness of these actuators is commonly in the order of from hundreds of nanometers to several microns. These types of actuators are easy to pattern and compatible with the MEMS fabrication process. However, they often exhibit very low actuation force and the fact that their transformation temperatures are dependent on their deposition conditions results in their unpredictable material properties.

Bulk-micromachined SMA actuators exhibit attractive features including very large forces, high mechanical robustness with simple structures, and biocompatibility [25, 37-40]. In addition SMA actuators are also ductile and corrosion resistant [41-43]. These properties make an SMA actuators very competitive and they have been successfully demonstrated in many applications including robotics [44-46] and microfluidics [47-48]. Nitinol, a biocompatible Ti-Ni SMA, has been used extensively in medical fields, facilitating the creation of a variety of implantable devices and surgical tools [25, 38, 40, 49-62]. However, their potential has yet to be fully exploited since research on the actuation methods, reversible motion and wafer level integration of these SMAs is still ongoing.

The reversible actuation of the SMA has mainly been considered in terms of two

mechanisms: one-way memory assisted by external forces provided by cold-state reset layers [22] and two-way memory [63]. One-way memory has been more commonly utilized for actuation due to its greater reliability as compared with the two-way memory method, which requires a long thermal cycling period for the material's training and is not very stable.

Various actuation mechanisms for SMA microactuators have been investigated. Joule heating by passing currents through heaters [64] or directly through SMA parts [65, 66] is among the most widely used method for their actuation. In this case, however, the mobility of the devices is severely constrained by the need for a wired interface, limiting the application range for the devices. In order to address this constraint, wirelessly controlled SMA microactuators have been studied.

## 1.4 Wireless Microactuators

Wireless microactuators provide a broad range of application opportunities. One promising area is in biomedical applications, including therapeutic implants and microsurgical tools. MEMS technology has been applied to develop wireless drug-delivery devices [67-70], which implement drug release by wirelessly triggering the breakage of the sealing membranes of drug reservoirs. Traditional actuators such piezoelectric [71-74], electrostatic [75-77], thermal [78, 79] and magnetic [80, 81] actuators are often limited by their need to be powered by wire interfaces. One major approach to the wireless control of microactuators is to utilize active circuitry, often powered by batteries [82-89]. In this approach, however, the actuators tend to develop a relatively large overall size, with limited longevity when batteries are used, and these constraints deteriorate as the number of actuators employed increases [89].

Passive actuation mechanisms eliminate the need for active circuitry and batteries and are thus potentially advantageous in terms of size, longevity, cost, and robustness. Passively operated wireless microactuators have been reported to use several mechanisms, including electrostatic actuations induced by surface acoustic waves [90] and magnetic fields [91], and energy-beam-assisted heating (for SMA [92-95], and bimorphs [96-98]). However, they pose various practical issues, such as possessing a small actuation force and stroke, employing high voltage, their micromachining, and actuator/system packaging. The magnetic actuation method has been applied to wirelessly control the actuators [99-105]. Even though a magnetic actuator is known to provide a large actuation force, this is only true in macro-scale cases. In micro-scale devices, a very high magnetic field is required to attract actuators [106], making this method undesirable. Moreover, the integration of magnetic material has yet not become an easy process in MEMS fabrication. The control of multiple actuators using magnetic actuation will further intensify the existing issues related to this method. Wireless control of multiple actuators using the electrostatic actuation method is reported in [107, 108]. This technique, however, requires a very high driving voltage for actuation and is not suitable to be applied for powering implantable devices in biomedical applications. Another limitation of the electrostatic actuation principle is its very limited actuation force. This problem becomes more apparent when the actuator is fabricated at the micro-scale level where force is dependent on the electrodes' surface area [109].

The ability to selectively and wirelessly control multiple microactuators will be a key to achieving novel functionalities while enhancing their performance. For implantable drug-delivery actuators, for example, this ability may be utilized to enable the controlled and selective delivery specific mixtures of diverse types of drugs. To the best of the author's knowledge, only a few of the techniques that use energy-beam-assisted heating for thermal

actuations reported the control of multiple microactuators [94, 95, 98]. In these types of wireless actuation techniques, however, overall systems employing beam sources and optics for beam conditioning tend to be large and complicated. In cases when the target actuator moves, typical in microrobotic applications, the beam control system needs to include an automated function that precisely directs the beam to the moving target to ensure its continuous actuation. These difficulties become further exacerbated when multiple actuators are involved. Moreover, these actuators are ineffective when an object obstructs the beam's path, and they are evidently inapplicable for actuations inside the body.

Another passive actuation approach that can potentially address the above mentioned issues is to use RF magnetic fields for the powering and control of thermal actuators. SMA actuators are promising candidates in this approach. A macro-scale implantable SMA valve passively operated using an RF power transfer was reported [110, 111]. The RF actuation approach potentially offers a means to enable multiple actuator operation by exploiting its frequency selectivity capability associated with SMAs. Designing each actuator to operate at a specific resonant frequency allows each of them to be controlled selectively or simultaneously using modulated frequency signals. In this study, wireless heaters in a form of passive planar inductor-capacitor (LC) resonant circuits that are controlled by RF magnetic fields are used to drive the SMA actuators.

## 1.5 Integration of Bulk-Micromachined SMA

Despite the favorable features of the bulk-SMA materials mentioned above, they have not been widely adopted in MEMS largely due to their incompatibility with standard batch microfabrication techniques, and difficulties in their wafer-level assembly. Recently, wafer-scale integration methods have been reported for SMA wires using SU-8 [112], and for bulk-

SMA devices using benzocyclobutene (BCB) bonding [113]. However, in these cases, the bonding strengths between the SMAs and the substrates have not been characterized. Other polymer-based adhesives utilized for wafer-level MEMS assembly that are potentially applicable to bulk-micromachined SMA bonding include polyimide (PI) [114], parylene [115] and epoxy [116]. SU-8 [117] and BCB [118] bonding have also been reported for wafer level MEMS packaging. Table 1.4 summarizes the properties of these polymer based bonding methods. In order to achieve high bonding strength, however, many of them require high-temperature processing that tends to introduce residual stress after bonding especially when there is a large mismatch in the coefficient of thermal expansion (CTE) between the materials bonded together. Void formation due to outgassing, which degrades bonding uniformity and strength, is also an issue with polymer adhesives.

With respect to applications for SMA bonding, polymer adhesives inherently pose challenges in achieving efficient heat transfer from heat sources to SMAs. For example, the thermal conductivity of polyimide (0.52 W/(m·°C)) is ~770 times smaller than that of Cu (401 W/(m·°C)). They also electrically isolate SMAs from the substrates, which can limit not only the applications of SMA devices but also their actuation methods when the direct Joule heating technique is used.

**Table 1.4**: Polymer based bonding properties.

| | Polyimide [114] | Epoxy [116] | BCB [118] | SU-8 [117] | Parylene [115] |
|---|---|---|---|---|---|
| Bonding time (minutes) | 60 | 30 | ~16 | N/A | 30 |
| Bonding pressure (kPa) | 200 | 3 | 10 | 0.6 | 900 |
| Bonding temperature (°C) | 160 | 150 | 250 | 90 | 230 |
| Bonding strength (MPa) | 8.2 | 14 | 30 | 20.6 | 3.6 |
| Void source | Solvent release | Solvent release | Solvent release | Bonding agent | Dirt particles |

Electroplating can be a means of bonding that potentially clears these issues associated with polymer adhesives. An electroplating bonding method was used for the fabrication of MEMS solenoid coils [119] in which electrical contacts were formed using electroplating. In addition to its use for electrical bonding reported in [119], electroplating is potentially an effective path to achieving robust mechanical bonding as well as high thermal coupling between a heat source and an SMA component, promoting the use of bulk-SMA materials for MEMS applications.

Another potential approach to enhance the use of bulk-micromachined SMAs in MEMS fabrication is to build the layers onto the SMA. In these cases the SMA will act as a substrate, the actuator as well as a part of the circuit will eventually form standalone devices. Furthermore, the direct integration of the heat source to the SMA part will improve the temporal response of the actuator compared to the case where the SMA and the heat source are built as two different parts that are then bonded together, which causes a delay in heat transfer. Furthermore, the direct integration approach is expected to allow batch fabrication of the bulk-SMA devices, where the heat source can be directly built onto the SMA.

## 1.6 Research Objectives

Although significant work has been conducted by many researchers on the bulk-SMA actuator, this material has not been exploited well in MEMS as noted earlier, and there are still many challenges on their actuation mechanisms and integration methods for successful applications. The main objective of this research was to study the integration and wireless control methods for bulk-micromachined SMA actuators. The focus was on wireless power transfers to the devices using external RF magnetic fields for their actuation, as well as the control of multiple SMA actuators, both in a passive manner that eliminates the need for

batteries and active circuitry. In terms of the integration of the bulk-micromachined SMA to the receiver electronics circuit, the research focus was to develop a unique planar integration method that provides good thermal conductance and strong bonding between the planar circuit and the SMA part. The objective was also to use the SMA as part of the circuit and also as an actuator, forming the SMA coil which would act as an out-of-plane actuator as well as the circuit so as to achieve a better temporal response as compared with the cases where the circuit is bonded to the SMA. In addition, the displacement of the SMA actuator needs to be wirelessly monitored and controlled to achieve a more precise operation, which was also investigated as part of the study.

## 1.7 Potential Impact of the Research

The applications of MEMS-based actuators/devices in biomedical areas are currently very limited due to various factors. These factors include the powering method, limited actuation force, overall device size, and biocompatibility issues as described in previous sections. The use of passive RF wireless control method to drive bulk-micromachined SMA actuators will uniquely allow us to address these issues effectively and will open a variety of application opportunities. One of the promising application areas is the implantable drug delivery devices [51, 62], in which the longevity and the overall size are very crucial to ensure the long term operation and minimal invasiveness of the devices. The ability to control multiple microactuators integrated in a device selectively in wireless manner will be another important feature for applications in surgical tools [50, 55] and catheters [58, 65], where this ability will enable more complex tasks and motions with them. The successful outcomes from this research are expected to promote advances in these device technologies in biomedical fields and beyond.

## 1.8 Research Methodology

Consequent to the discusssion in the previous section, the development of the MEMS SMA device particularly involves the wireless control of SMA actuators using RF signals, the integration of the SMA to the planar circuits, the selective actuation of multiple actuators, out-of-plane SMA actuators, wireless displacement tracking, thermal and temporal performance analyses, and optimization.

The research described in this dissertation can be divided into three main streams: a) A study of the wireless power transfer and the heat generation mechanism on planar coils to drive the SMA actuator; b) The development of wireless bulk-micromachined SMA actuators and their integration method; and c) The application, demonstration and characterization of the fabricated actuators. The following approach was carried out to achieve the research objectives:

**A. Wireless power transfer and heat generation characterization**

As noted earlier, passive resonant circuits can serve as wireless heaters for the remote control of thermal actuators including SMAs. Experiments and analyses were carried out to evaluate RF power transfer and heat generation efficiency and their dependence on receiver coil size, the distance between the transmitting coil and the receiver, and the line width (resistance change) of the coils for the wireless resonant heater. The simplified models were then used to evaluate the experimental result.

**B. Design and simulation of a SMA actuator**

In the initial stage of the research, the effort for design and fabrication focused on a single SMA actuator and the integration of bulk-SMAs into the MEMS fabrication process. As

part of this effort, simulation work was performed to determine the displacement of the actuators and based on this result the fabrication steps were developed. The materials for the fabrication including that of the SMAs were determined.

**C. Development of planar assembly and the bonding technique of bulk-micromachined SMA actuators, and their characterization**

In order to address the issues involved in SMA integration, a planar assembly technique based on photo-defined selective electroplating was developed and used to bond the SMA actuators to the heater circuits. The setup to perform the bonding strength test was developed and the bonding strength of the proposed method will be characterized. Using the developed integration method, a bulk-micromachined SMA gripper operated through frequency-selectable wireless excitation using external RF magnetic fields was fabricated and demonstrated. Detailed measurement including the thermal and temporal response of the actuator was performed. The result was then compared with the measured phase transformation properties of the SMA used for the fabrication of the device.

**D. Control of multiple SMA actuators using frequency modulated signals**

The study was then extended to the wireless SMA actuation using the RF signal principle that achieves multiple-microactuator control while addressing the issues possessed by other wireless actuation principles such as the laser beam and electron beam techniques. This is an essential step to ensure that the wireless SMA actuation using the RF signal can be adapted to various possible applications by employing multiple actuators. This step also involves the design, simulation and fabrication of the device. A proof-of-concept device that employs three actuators based on this principle was then fabricated and its microfluidic application was demonstrated.

**E. Batch integration of SMA actuators and thermal characterization**

In this step, a detailed characterization of the developed bonding technique based on photo-defined electroplating that may be leveraged for the microfabrication of arrayed SMA actuators by scaling up the technique was performed. The multiple actuations of the devices using frequency modulated RF signals as well as heat transfers from a wireless heater to the SMA through electroplated Cu was evaluated. In addition, the thermal coupling and the heat distribution between the actuators was measured to verify the effect of the heat produced on the nearby actuators. The time the response of the actuators for various power levels was evaluated.

**F. Direct integration of wireless heat source with SMA actuators**

In the previous stages, the actuator is bonded to a separate heater component, i.e., the passive resonant circuit, to provide heat to the actuator. As discussed earlier, it is expected that the direct integration of the heat source onto the SMA structures improves the temporal response and achieve uniform heating of the device. Moreover, it would further miniaturize the device. For the direct integration of the LC circuit (i.e., wireless heater) on the SMA, however, the adverse effects of Eddy currents produced in the SMA and their negative impact on the RF power transfer to the circuit may be involved in the device. These potential issues may be effectively circumvented if the receiver coil (the inductor of the LC circuit) itself is formed using the SMA that simultaneously behaves as an actuator. In this stage, an SMA coil that forms an out-of-plane actuator was designed and fabricated using the localized bimorph actuation method. The whole LC circuit was fabricated on the SMA to improve the temporal response of the actuator. The impact of the miniaturization and direct integration of the SMA on the temporal response was characterized. In addition,

the forces generated by the SMA and the bimorph layer were measured and analyzed. As an extension of this study, this new out-of-plane actuator concept also provided different microdevice application opportunities beyond SMA actuators and was applied to the development of three-dimensional (3-D) micromachined inductors.

### G. Wireless displacement monitoring

This step involves the wireless displacement tracking of the out-of-plane spiral actuator. As described in the previous section, it is important to establish a means to implement high-precision displacement control for an accurate operation and continuous monitoring. The SMA actuator in the form of an out-of-plane coil with a capacitor forms a resonant circuit which gives the flexibility to wirelessly track its resonant frequency. When the coil is actuated, the change in the displacement modifies the inductance value of the coil and causes a shift in the resonant frequency of the device. This change in the resonant frequency can be tracked by employing an external coil to determine the actual displacement because its discrete frequency value corresponds to a specific degree of displacement. This might be a useful property for enabling the built-in function for displacement monitoring. In this stage the change in the displacement and the resonant frequency was characterized.

### H. Optimization

In this step, the focus was on the Q-factor improvement for achieving better resonant frequency tracking. The SMA has a relatively high electrical resistance which reduces the Q-factor of the coil. This resistance will be further increased as the SMA is heated to the austenite phase. This issue was addressed by adding an additional material that has a very

high electrical conductivity onto the SMA coil. The resistance change and Q-factor improvement were measured and reported.

## 1.9 Thesis Overview

This dissertation is divided into 6 chapters. The research background, objectives and research methodology are described in Chapter 1. Chapter 2 focuses on the background theory of the planar LC circuit, wireless power transfer and heat generation in the planar coils as well as on experimental verification (A in Section 1.7). Chapter 3 focuses on the design, fabrication and characterization of a wireless bulk-micromachined SMA microgripper. This chapter also discusses the development and characterization of the electroplating bonding technique that was used to integrate bulk-micromachined SMAs to the planar LC circuit (B and C in Section 1.7). Chapter 4 describes the design and development of the wireless control of multiple SMA actuators, and its application and detailed characterization (D and E in Section 1.7). In Chapter 5, the direct integration of the LC circuit using SMA is reported. In addition, this chapter also discusses out-of-plane displacements using localized bimorph actuations, wireless frequency monitoring for displacement tracking and quality factor improvement (F, G and H in Section 1.7). The last chapter, Chapter 6, discusses the findings and contributions and provides direction for future work in this research field. Mentioned in the appendix, an additional investigation that was performed using the out-of-plane displacement method employing localized bimorph actuation as reported in Chapter 5, to form a 3-dimentional out-of-plane Cu coil is described.

# Chapter 2

# Wireless Power Transmission: Background, Theory and Analysis

## 2.1 Introduction

Over past decades, the study of wireless power transmission has gained tremendous interest [120-124]. So far, wireless power transmission using electromagnetic coupling has been applied to and demonstrated for many applications include consumer electronics products such as smart phones, computer peripherals and wireless sensors [125]. However, wireless power is more prominently employed in cases where the use of interconnecting wires would be inconvenient, hazardous, or impossible. Thus, much attention has been applied to the wireless empowerment of biomedical applications such as implantable medical devices that need continuous monitoring and/or operation [126-130].

Wireless power transfer, especially in microscale devices, often encounters challenges due to the requirement for conditioning circuitries to rectify and regulate the power that received at the receiver section. This requirement causes an undesirable increase in the overall size of such devices, and remains one of their main issues. As well, the use of additional electronic components causes additional power losses and makes overall power transfer inefficient. Another important fact is that power loses from heat generated at the receiver coil further deteriorate the efficiency of the power transfer.

Considering all of the above motioned issues, the use of wireless power transfer to control thermo-responsive materials such as SMA actuators by utilizing the heat generated

at the receiver coil could be very beneficial. This also eliminates the losses associated with the conditioning circuitries. On top of that, it is also reduces the overall size of the devices.

In this chapter, a study on the wireless power transfer through RF magnetic coupling and heat generation are reported. The receiver microcoil is fabricated to have various sizes and dimensions. The coupling coefficient between the transmitting and receiving coils are theoretically and experimentally analyzed and compared. The relationship between the coil size, resistivity and Q-factor with the heat generated in terms of the steady state temperature is also studied and reported.

## 2.2 Background

There are numerous studies that describe the underlying physics of RF wireless power transfer, including efficiency and design considerations [131, 132]. The wireless power transmission using magnetic coupling between sets of coils can be found in almost any electronic device that uses transformer. In transformer, two coils are coupled using a magnetically conducting core such as iron. However, it is not practical to use metal cores in cases where coupling between coils is performed over large distances.

Using a similar concept to that utilized in the transformer, power transfer is accomplished using two coils without the use of a metal core, a transmitter coil that supplies energy in the form of a magnetic field and receiver coil that collects energy from this field [133]. Since no magnetic core is employed to focus and concentrate the magnetic field, the transmitter and receiver coil are aligned so that maximum power transfer will occur. Figure 2.1 depicts the working principle of inductive coupling and wireless power transmission between a transmitter coil and the receiver planar coil.

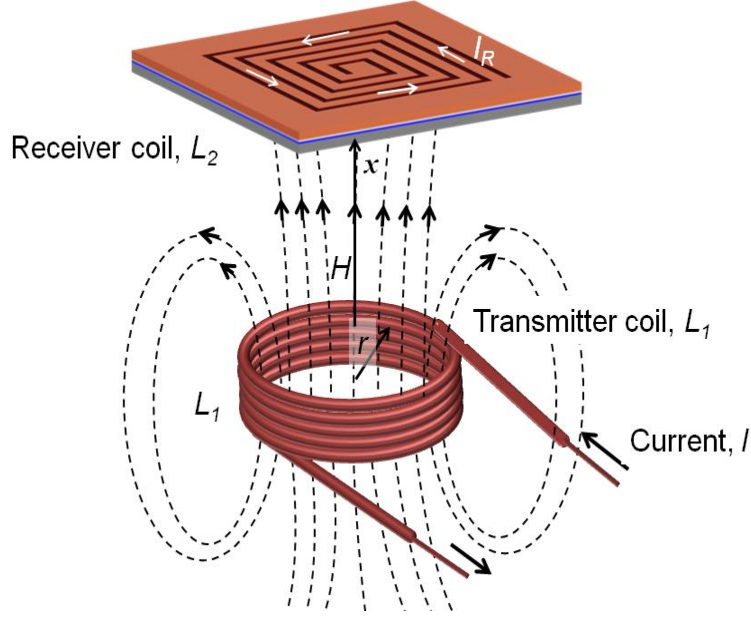


**Figure 2.1:** The working principle of wireless power transmission between two coils.

The magnetic field is generated at the transmitting coil when an alternating current, $I$, flows through the coil turns. Based on Ampere's Law, the magnetic field strength, $H$, is proportional to the current supplied to the transmitting coil. The magnetic field strength, $H$, as a function of a specific distance, $x$, can be expressed as [122];

$$H(x) = \frac{I \cdot n_t \cdot r^2}{2\sqrt{\left(r^2 + x^2\right)^3}} \tag{2.1}$$

where $I$, $n_t$ and $r$ are the circulating current, the number of turns and the radius of the transmitting coil, respectively. Both transmitter coil, $L_1$ and receiver coil, $L_2$ form a magnetically coupled mutual inductance, $M$. An electromotive force, $v$ will be induced at the receiving coil when it is placed within the magnetic field produced by the transmitting coil. The $v$ induced in the receiver coil can be estimated using Faraday's law [122];

$$v = \mu_0 H \omega n_p A_p \tag{2.2}$$

where $\mu_0$ is the magnetic constant, $\omega$ is the operating angular frequency, and $n_p$ and $A_p$ are the number of turns and the area of the receiver coil, respectively.

In order to drive the thermal actuators using magnetic wireless power transmission, the objective of this research, receiver coil is designed to have a resonant frequency, $f_r$, that matches the frequency of the magnetic field induced by the transmitter coil, $f_m$. In this case, the power will be efficiently converted as Joule heat as will be described in Section 2.4.5. The coupling coefficient, $k$, between the transmitter and the receiver coils and also the Q-factor, are important parameters that need to be considered in wireless power transmission for efficient power transfer. The coefficient, $k$, Q-factor and the heat generated by the coil are also discussed in this chapter. The design of the receiver coil is discussed in Section 2.3.

## 2.3 Design and Fabrication of the Planar Resonant Circuit

In MEMS, planar coils are very important elements and are being widely used especially for the generation of magnetic fields [134-138]. This is mainly due to the simplicity of their fabrication methods. Extensive work has been done on the modeling and design of planar coils [139-141]. The focus of this section is on the design of the planar resonant circuit, which will be used as a receiver coil for wireless power transmission, using a simplified model.

Generally, passive resonant circuits are formed from connecting a planar inductor, $L$, and a parallel plate capacitor, $C$, in parallel as depicted in Figure 2.2. The resonant frequency of this circuit is given as $f_r=1/(2\pi\ (LC)^{-1/2})$. When $L$ is fabricated in a planar coil form, the resonant circuit can be magnetically coupled by bringing it into the vicinity of the magnetic field generated by the transmitting coil as described in the previous section. The values of $L$ and $C$ depend on their shape and dimensions.

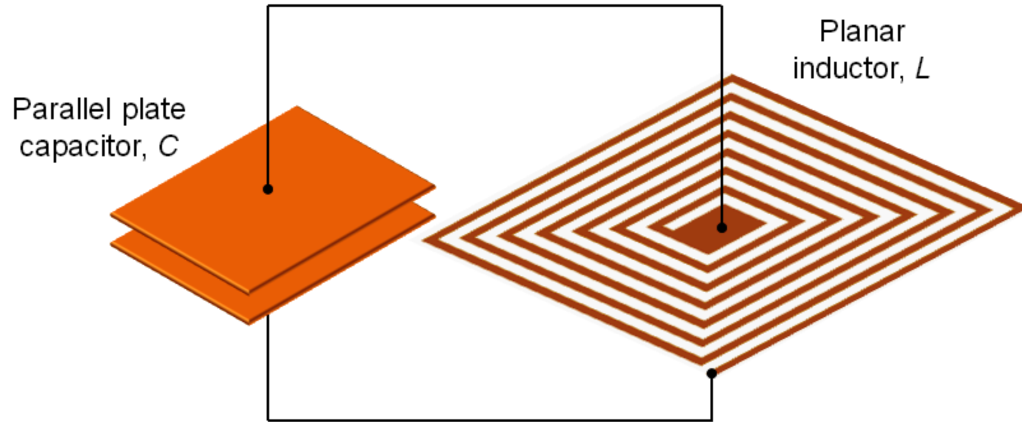


**Figure 2.2:** LC resonant circuit.

Significant work has been accomplished on the modeling of planar coils using lumped circuit models [139, 140]. In [142], an accurate representation of spiral coil is reported. However, the model presented does not expressed directly by the simple dimensions of the coils. A simplified accurate model for the planar spiral inductor based on the Wheeler model [143] has been reported in [141] to facilitate the design of planar coils. Figure 2.3 illustrates an example of a square spiral planar coil that is used as a model for inductance calculations based on the simplified Wheeler model.

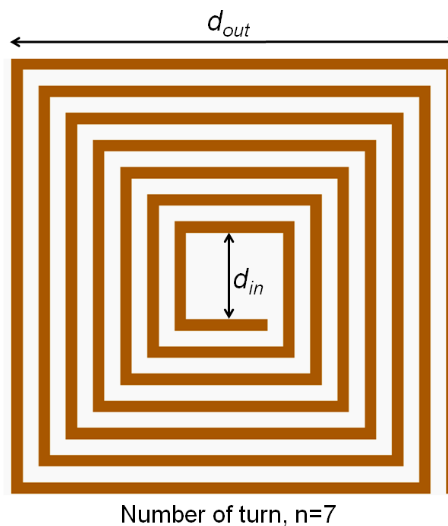


**Figure 2.3:** Square type spiral planar coil.

The $L$ value of the square spiral coil as illustrated in Figure 2.3 is given by [141];

$$L = K_1 \mu_0 \frac{n^2 d_{avg}}{1 + K_2 \rho_f} \tag{2.3}$$

where $K$ is the layout dependent constant. $K_1$ and $K_2$ are 2.34 and 2.75, respectively. The fill ratio, $\rho_f$, is defined as $(d_{out} - d_{in}) / (d_{out} + d_{in})$ and the average diameter $d_{avg}$ is given by $0.5(d_{out} + d_{in})$. $d_{out}$ and $d_{in}$ are define in Figure 2.3.

The value of $C$ is basically determined by the area, $A$, the separation gap, $d$, and the dielectric constant of the dielectric material, $\varepsilon_r$, between the two parallel plates that are used to form the capacitor. A parallel plate capacitor's effective capacitance is simply expressed as $C = \varepsilon_o \varepsilon_r A/d$, where $\varepsilon_o$ is the vacuum permittivity.

Based on the above mentioned models for estimating $L$ and $C$ values, planar resonant circuits that have specific resonant frequencies are fabricated. The LC resonant circuit is fabricated on the Cu-clad PI substrate that offers a simple and cost effective implementation. In addition, PI is being widely used in implantable devices due to its biocompatibility property [144]. Furthermore, Cu-clad PI is the basis of the flex-circuit technology that is well established for electronic circuit fabrication.

Figure 2.4 illustrates the fabrication process of the LC resonant circuit. A single-sided Cu-clad PI (Shehdahl Co., MN, USA) with 50-µm thick PI and 5-µm thick Cu is used in this effort. The photolithography for the circuit fabrication is performed with liquid and dry-film photoresists (SPR 220-7, Rohm and Hass Co., PA, USA and 15-µm-thick MacDermid SF 306). The first capacitor electrode is formed by wet etching of the Cu-clad layer using patterned SF306 photoresist as a mask (step 1). Next, the PI film is etched using a KOH-based solution to create the via contact hole in the film (step 2). Then, a Ti-Cu seed layer

(thickness of 200 nm and 1 μm for Ti and Cu, respectively) is deposited on the PI side using e-beam evaporation.

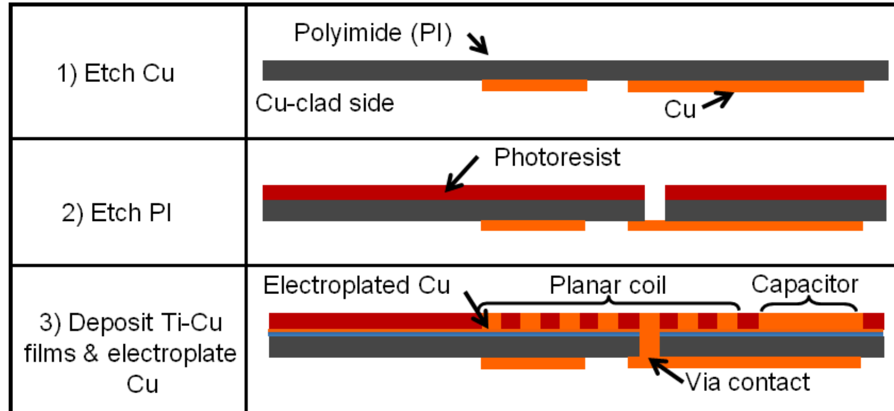


**Figure 2.4:** Fabrication process of the LC circuit.

Next, Cu electroplating in the patterned SPR 220-7 photoresist mold is performed in a sulfuric-acid-based bath for 10 minutes to form the coil and the other capacitor electrode with a thickness of 8-10 μm (step 3). The photoresist is then stripped in concentrated sodium carbonate solution. The fabrication of the LC circuit is completed by etching the seed Cu-Ti layers. Figure 2.5 shows an example of the fabricated LC circuits.

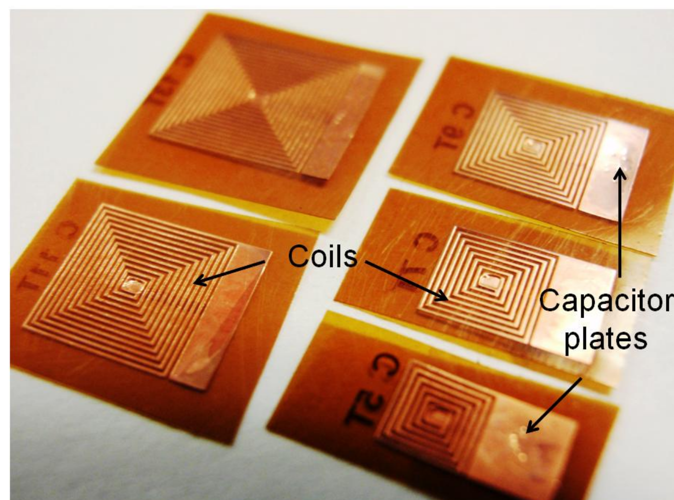


**Figure 2.5:** Fabricated LC circuits.

## 2.4 Results

Planar coils have been widely studied by many researchers in terms of their Q-factor [145], induced magnetic fields [146], and applications [147, 148]. The planar coils also have been extensively studied for wireless power transmission [149, 150]. In this section, we report a study for wireless power transfer to the planar LC resonant circuits with coils with varying line width and numbers of turns to evaluate the wireless power transfer efficiency, and heat generation in the coils which could be benefited to wirelessly drive the thermal actuators. The study also includes the measurement of their $f_r$, frequency-dependent resistivity, and Q-factor. In addition, the coupling coefficient between the planar LC resonant circuits and the transmitter coil are evaluated and reported.

### 2.4.1 Resonant Frequency

Two different sets of LC circuits are fabricated; the coils in the first set have different numbers of turn, $n$ (5, 7, 9, 11 and 13 turns), as illustrated in Figure 2.5. The coils in the second set have different fill ratios achieved by adjusting its line width, $l_w$ (50, 75, 100, 125, 150 and 175 μm). All the LC circuits are designed to have the same $C$ value of $5$ pF by keeping the electrodes area constant. All the capacitors are fabricated using a 50-μm thick PI sheet as their dielectric separation layer (dielectric constant, $\varepsilon_r$ of 3.4). The parameters of both types of coils are described in Tables 2.1 and 2.2.

**Table 2.1:** Parameters for coils with different numbers of turns.

| No. of turns, $n$ | $d_{in}$ (mm) | $d_{out}$ (mm) | Line width, $l_w$ (μm) | Line spacing (μm) | Coil dimensions (mm$^2$) |
|---|---|---|---|---|---|
| 5 | 0.8 | 3.1 | 100 | 150 | 3.1 x 3.1 |
| 7 | 0.8 | 4.1 | 100 | 150 | 4.1 x 4.1 |
| 9 | 0.8 | 5.1 | 100 | 150 | 5.1 x 5.1 |
| 11 | 0.8 | 6.1 | 100 | 150 | 6.1 x 6.1 |
| 13 | 0.8 | 7.1 | 100 | 150 | 7.1 x 7.1 |

*All coils have the same capacitor area of 8.4 mm$^2$.*

**Table 2.2:** Parameters for coils with different fill ratios.

| Line width, $l_w$ (μm) | Line spacing (μm) | Fill ratio, $\rho_f$ | $d_{in}$ (mm) | $d_{out}$ (mm) | No. of turns, $N$ |
|---|---|---|---|---|---|
| 50 | 200 | 0.15 | 0.9 | 5.6 | 10 |
| 75 | 175 | 0.23 | 0.85 | 5.6 | 10 |
| 100 | 150 | 0.31 | 0.8 | 5.6 | 10 |
| 125 | 125 | 0.39 | 0.75 | 5.6 | 10 |
| 150 | 100 | 0.47 | 0.7 | 5.6 | 10 |
| 175 | 75 | 0.55 | 0.65 | 5.6 | 10 |

*All coils have the same capacitor area of 8.4 mm$^2$ and the same coil dimensions of 5.6 mm × 5.6 mm.*

The resonant frequencies, $f_r$, of the fabricated coils are measured using a network-spectrum-impedance analyzer (Agilent 4396B) and compared with the calculated values. Figure 2.6 plots $f_r$ of the coils with $n$ of 5 to 13 turns. The calculated and measured values show a very good fit with less than 4% error. The coils with higher $n$ posses a lower $f_r$ as there is an increase in $L$. The coil with $n$ of 13 has $f_r$ of 86 MHz and $f_r$ increases exponentially as $n$ decreases. The coil with $n$ of 5 has $f_r$ of 299 MHz which is more than 3 times increase in $f_r$ compared to the case with $n$ of 13.

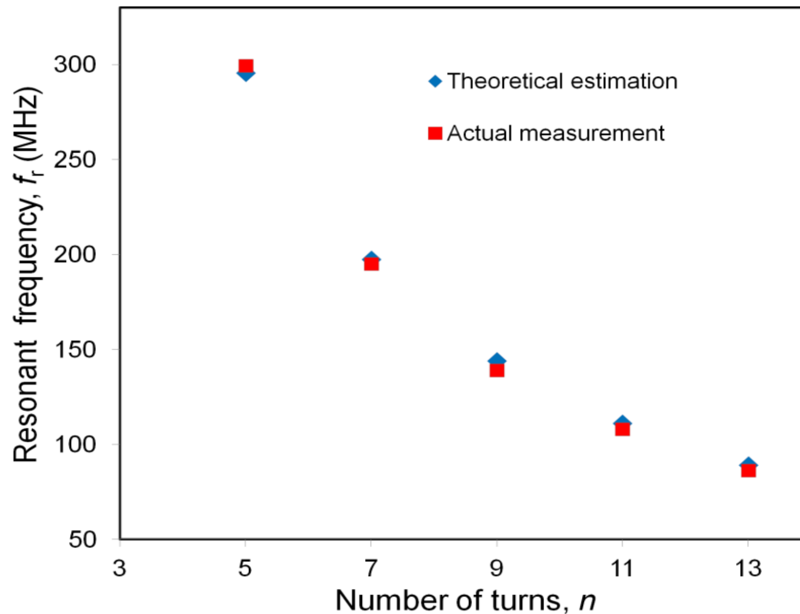


**Figure 2.6:** Changes in $f_r$ for coil with different numbers of turns and a comparison between the measured and theoretical values.

Figure 2.7 shows $f_r$ for coils with different fill ratios. The coils $l_w$ increases from 50 to 175 µm with a 25 µm increase in each step (Note: the relationship between $l_w$ and fill ratio, $\rho_f$ is shown in Table 2.2). The calculated $f_r$ values have relatively good agreement with measured values with less than 5 % error. As observed in the plot, $f_r$ has a proportional relationship with $l_w$ of the coil which is due to a reduction in $L$. The coil with a larger $l_w$ has a smaller $L$ since the inner turns of the coil are closer to the centre of the spiral and thus contribute more negative and less positive mutual inductance [141]. Even though there is an increasing trend in $f_r$ the actual increase is only around 3.6 % when $l_w$ is doubled from 50 µm (118.6 MHz) to 100 µm (122.9 MHz) while keeping the $d_{out}$ and the $n$ constant.

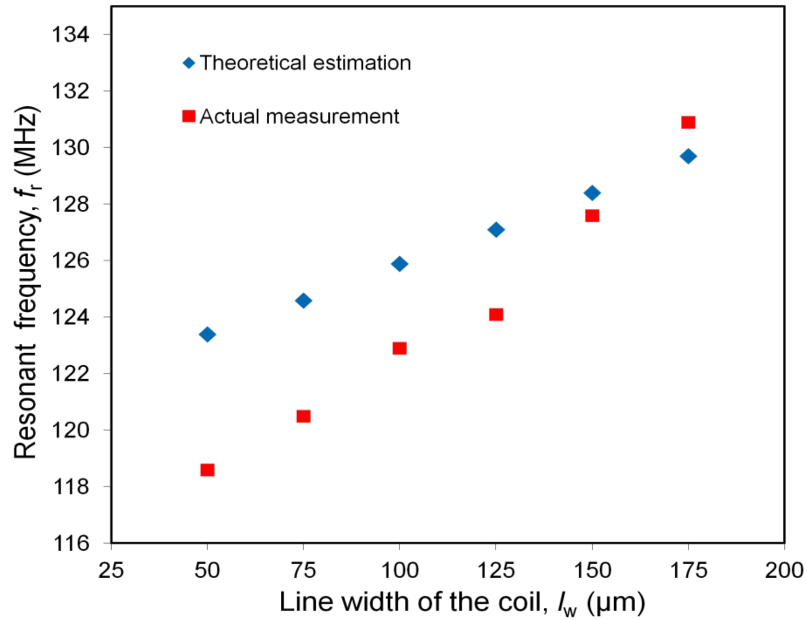


**Figure 2.7:** Changes in $f_r$ for coil with different fill ratios and a comparison between the measured and theoretical values.

### 2.4.2 Coil Resistance

Another important factor in wireless power transfer is that the resistance of the planar coil, $R_o$. $R_o$, can be expressed as $\rho l/A$, where $\rho$ is the resistivity of the material that is used to

construct the coil, $l$ is the length of the coil line, and $A$ is the cross-sectional area of the wire. As $R_o$ of the coil increases, the Q-factor of the coil, given by $Q = \sqrt{L}/(R_o\sqrt{C})$, is degraded and eventually affecting the overall efficiency of the wireless power transfer. The measurement of $R_o$ was performed using the Agilent impedance analyzer to determine the frequency characteristic of $R_o$. The frequency dependence of $R_o$ is caused by strong time-varying magnetic fields produced by an alternating current passing through the conductor. This induces a current that is normal to the magnetic field and in the opposite direction to the supplied current. This phenomenon is called Eddy currents, which is an undesirable element in wireless power transfer. When the coil operates at a higher frequency, the current shifts to the surface of the coil, and results in an uneven current redistribution in the coil lines. This effect which is known as the skin effect leads to an increase in the coil's $R_o$. The measured $R_o$ for the set of coils with different $n$ and $l_w$ values are plotted in Figures 2.8 and Figure 2.9, respectively.

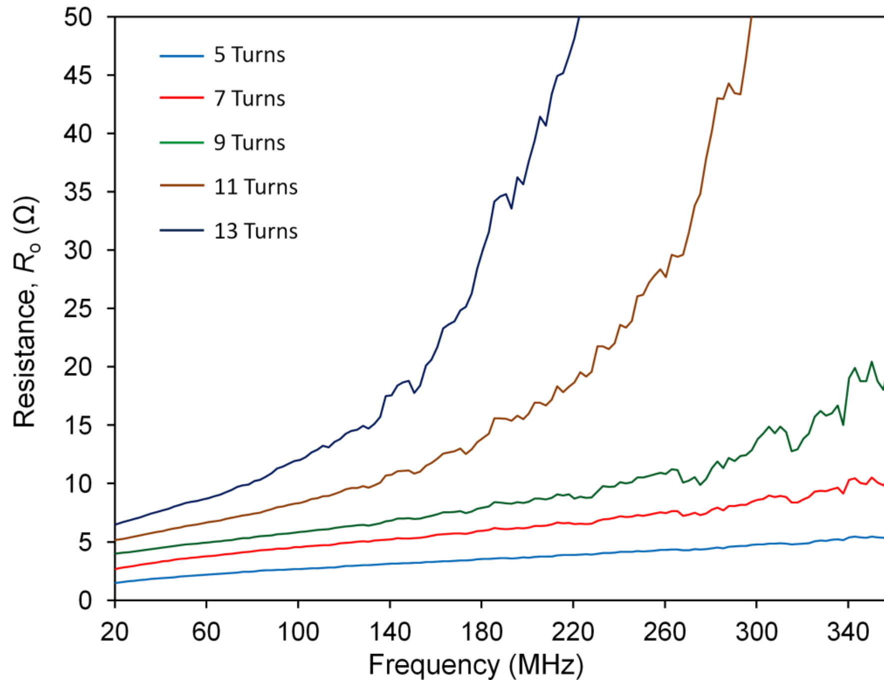


**Figure 2.8:** Frequency-dependent characteristics of coils with different numbers of turns.

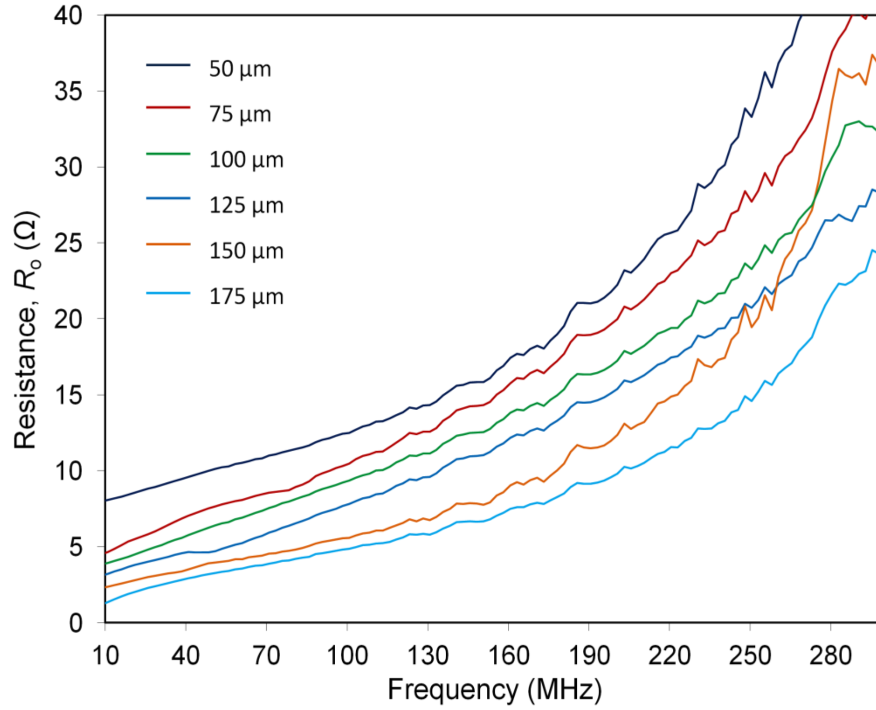


**Figure 2.9:** Frequency-dependent characteristics of coils with different line widths.

As shown in Figures 2.8 and 2.9, $R_o$ of the coils shows an increasing trend toward a higher frequency due to the Eddy current and skin effects described earlier. In both cases, the increase in $n$ and the fill ratio modification through varying $l_w$, measurements agrees with the resistance model.

In the varying $n$ case as plotted in Figure 2.8, the coil with a higher $n$ possesses a higher $R_o$. This is due to an increase in the total length of the coil wire when the coil has a larger $n$. For example, the coil with $n$ of 13 has $R_o$ of 5.8 Ω as compared with a coil with $n$ of 5 which has 1.3 Ω at a 10 MHz frequency. As described in the resonant frequency measurement section, the above coils have $f_r$ values of 87 and 299 MHz for $n$ of 13 and 5, respectively which suggests that the actual resistances for these coils during the operation are ~11 Ω and 5 Ω, respectively. The values of measured $f_r$, $L$, $C$ and $R_o$ of the fabricated coils at operating frequency are described in Table 2.3.

**Table 2.3:** Measured electrical parameters for the fabricated coils with different numbers of turns.

| Number of turns, $n$ | Resonant frequency, $f_r$ (MHz) | Inductance, $L$ (nH) | Capacitance, $C$ (pF) | Resistance, $R_o$ (Ω) |
|---|---|---|---|---|
| 5 | 299.3 | 50.1 | 5 | 4.81 |
| 7 | 195.2 | 118 | 5 | 6.1 |
| 9 | 139.2 | 242.5 | 5 | 7.2 |
| 11 | 108.3 | 410.9 | 5 | 8.86 |
| 13 | 86.5 | 610.4 | 5 | 10.5 |

As can be verified in Figure 2.9, $R_o$ decreases as the fill ratio is increased. For the coil with $l_w$ of 50 μm, $R_o$ is ~14 Ω at its $f_r$ (118 MHz) while the coil with $l_w$ of 100 μm has $R_o$ of 11.1 Ω (at $f_r$, 123 MHz). Although $l_w$ is doubled from 50 to 100 μm, $R_o$ does not show the same amount of change in this case. This might be caused by the skin effect where the current is pushed to the edge or side of the wire and the increase in $l_w$ has less effect on $R_o$. The values of $f_r$, $L$, $C$ and $R_o$ of the fabricated coils at $f_r$ are described in Tables 2.3 and 2.4.

**Table 2.4:** Measured electrical parameters for the fabricated coils with different fill ratios.

| Line Width, $l_w$ (μm) | Fill ratio | Resonant frequency, $f_r$ (MHz) | Inductance, $L$ (nH) | Capacitance, $C$ (pF) | Resistance, $R_o$ (Ω) |
|---|---|---|---|---|---|
| 50 | 0.15 | 118.6 | 350.2 | 5 | 14 |
| 75 | 0.23 | 120.5 | 340.9 | 5 | 12.5 |
| 100 | 0.31 | 122.9 | 325.4 | 5 | 11.1 |
| 125 | 0.39 | 124.1 | 322.9 | 5 | 9.16 |
| 150 | 0.47 | 127.6 | 304.2 | 5 | 7.75 |
| 175 | 0.55 | 130.9 | 290.7 | 5 | 6.54 |

### 2.4.3 Quality Factor

In achieving efficient power transfer, the Eddy current that causes power losses due to heating affecting the power transfer efficiency is considered as a detrimental factor. Although the heating due to Eddy currents could be beneficial in driving the thermal actuators, the increase in resistance causes a reduction in the Q-factor and affects the efficiency of the

power transfer to the coil. In addition, the increase in $R_o$ will reduce the current, $I$, in the coil with a given voltage, where $I$ has more influence on the coil power, $P$, as given by $I^2 R$, and results in less resistive heat generation in the coil.

The Q-factor is defined by the ratio of the energy stored to the energy dissipated in a resonator. The Q-factor of the fabricated resonant LC circuits was measured and plotted in Figures 2.10 and 2.11. The changes in the resonant circuits' Q-factor in these cases are only caused by the change in $L$ and $R_o$, as $C$ is kept constant for all the resonant circuits tested. As can be observed in both cases in Figures 2.10 and 2.11, Q-factor shows increasing trends as $n$ and $l_w$ increase, respectively.

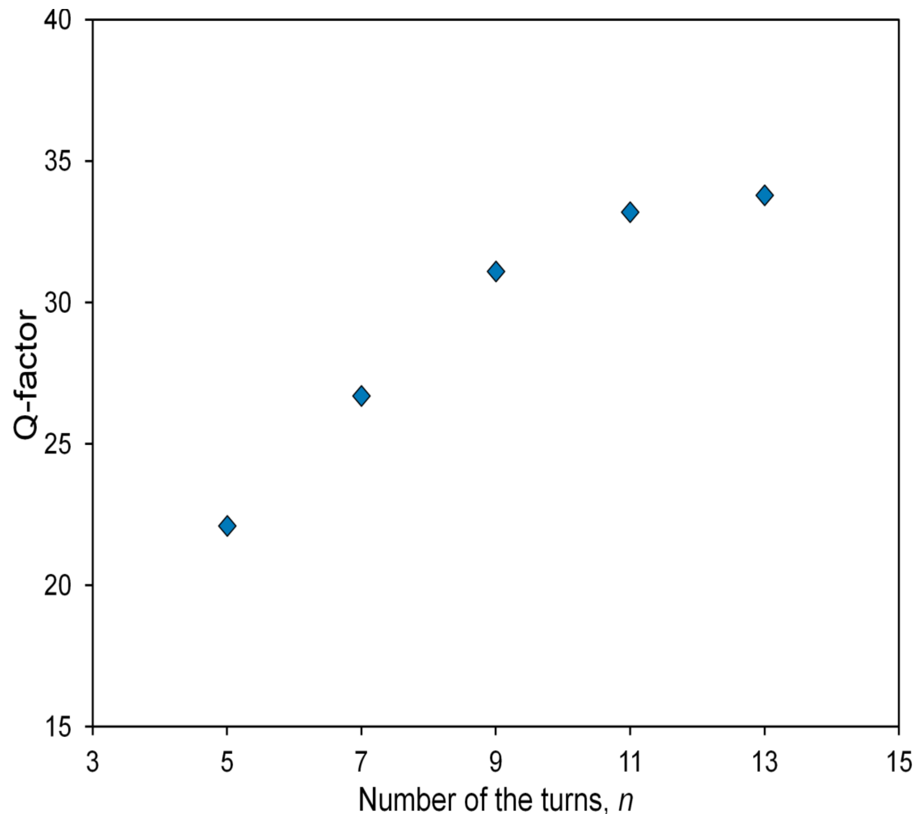


**Figure 2.10:** Q-factors of the fabricated LC resonant circuits with different numbers of turns.

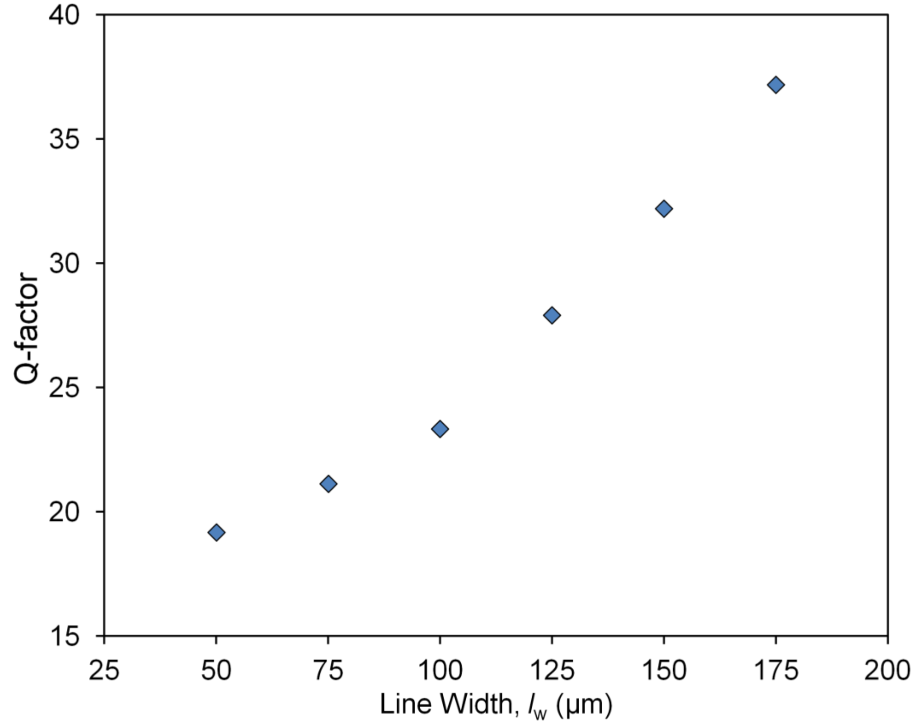


**Figure 2.11:** Q-factors of the fabricated LC resonant circuits with different line widths.

When $n$ is increased, the total inductance of the coil increases, resulting in an increase in Q-factor. Significant improvement in Q-factor from ~22 to ~31, at about a ~41% improvement, was observed as $n$ increased from 5 to 9. The Q-factor's trend, however, does not show much progress as $n$ further increases to 11 and 13, where the recorded Q-factor values are ~33 and ~34, respectively. This suggests an only 10% improvement when $n$ is increased from 9 to 13.This phenomenon is caused by the rise of $R_o$ with $n$ since the length of the coil wire increases significantly as the perimeter of the planar coil grows. Although there is also a boost in $L$, the dominant factor in the Q-factor is $R_o$, since $L$ is square-rooted in the Q-factor relationship, as previously demonstrated.

On the other hand, Q-factor shows continual improvement when the fill ratio of the coils is increased by increasing $l_w$ of the coil from 50 µm to 175 µm by a 25 µm stepwise increment. As shown on the plot in Figure 2.11, Q-factor is increased from ~19 to ~37 when

$l_w$ is increased from 50 to 175 µm. This corresponds to an improvement of ~95% from the original Q-factor. From the results reported in Table 2.4, there is a small reduction in $L$ as $l_w$ is increased that contributes to the drop in Q-factor. However, this decrease in $L$ is much lower than the dominant element, $R_o$, in the $Q$.

### 2.4.4 Coupling Coefficient

In wireless power transmissions using RF magnetic coupling, high efficiency between transmitter and receiver coils is usually achieved at distances of less than the diameter of the transmitting coil. In other words, the transmitter and receiver coils should be placed close to one another in order to achieve strong magnetic coupling between them. The transmitter coil generates a magnetic field and the receiver coil partially accepts it depending on the coupling coefficient, $k$, which is a quantitative description to represent how well the two coils are coupled together. The coupling coefficient is given by [133];

$$k = \frac{M}{\sqrt{L_T L_R}} \tag{2.4}$$

where $M$ is the mutual inductance between the transmitter and receiver coils, and $L_T$ and $L_R$ are the inductance of the transmitter and receiver coils, respectively. $k$ denotes a value from 0 to 1, where 1 indicates that both coils have perfect coupling.

A large $M$ is the main source for a good coupling between the transmitter and receiver coils and leads to an efficient power transfer. $M$ is dependent on the shape, distance and alignment of the transmitter and receiver coils which makes the modeling complex [151-152]. Since the modeling of $M$ is not the main focus of this research, this parameter is calculated based on the measurement results. $M$ can be calculated based on [153];

$$2M = L_{Total} - L_T - L_R \tag{2.5}$$

where $L_{\text{Total}}$ is the measured inductance value when both $L_T$ and $L_R$ are connected in series and aligned together as used in a wireless power transfer case. When they are aligned in-phase, the total inductance will be more than the sum of their individual inductances. The difference between the measured $L_{\text{Total}}$ and the sum of individual $Ls$ is twice the mutual inductance. The parameters of the transmitter coil are described in Table 2.5. Based on Equation 2.4, the $k$ coefficient between the transmitter, which is a wounded cylindrical coil (used as transmitter for all experiments) and receiver coils is computed using the measured $M$ between the coils. Figures 2.12 and 2.13 show $k$ between the transmitter and receiver coils (Table 2.1) when they are well aligned at a 1 mm distance.

**Table 2.5:** Transmitter coil parameters.

| Parameter | Value |
|---|---|
| Diameter | 6 mm |
| Inductance | 497 nH |
| Q-factor | 160 |
| Number of turns | 9 |

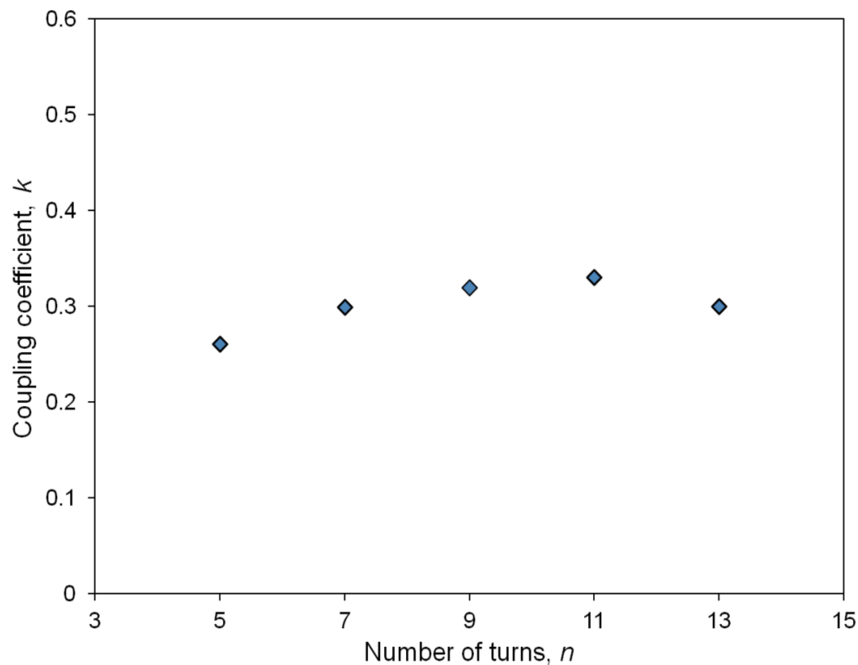


**Figure 2.12:** Coupling coefficient between transmitter and receiver coils with different numbers of turns.

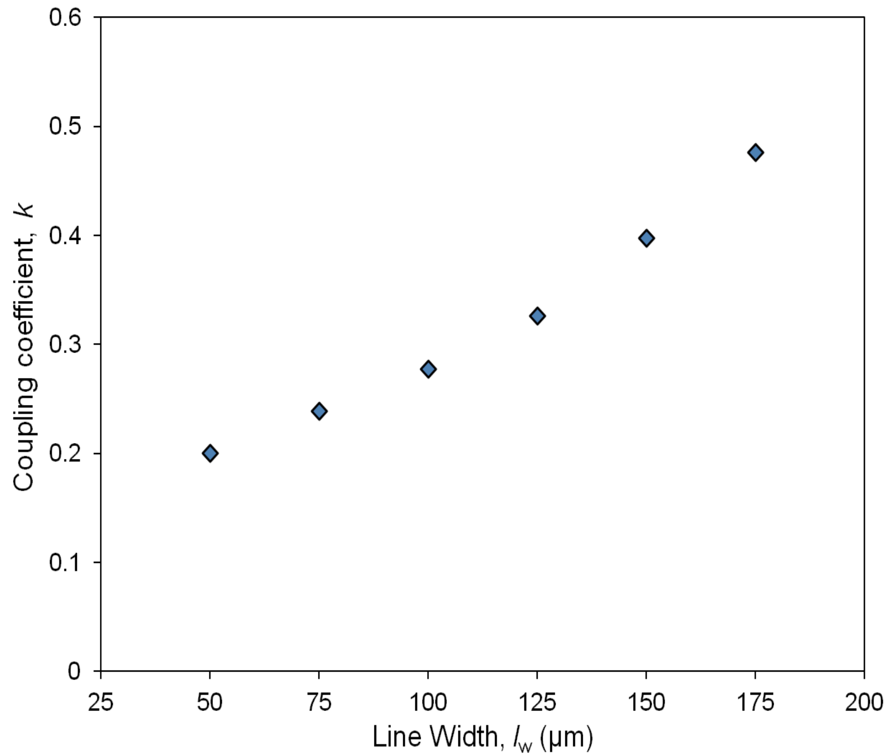


**Figure 2.13:** Coupling coefficient between transmitter and receiver coils with different line widths.

Figure 2.12 shows a small increase in $k$ when the number of the turns increases. $k$ increased about ~35 % when $n$ is increased from 5 to 11. However, $k$ drops about ~14 % from 0.35 to 0.3 when $n$ is further increased from 11 to 13. This is mainly due to the size of the receiver coil (Table 2.1) with $n$ of 13 (7.1 x 7.1 mm$^2$) which exceeds the size of the transmitter coil (with a 6-mm diameter).

When the fill ratio of the coils is modified by adjusting $l_w$, there is also change in $k$ as shown in Figure 2.13. The $k$ coefficient sustains a continuous increase when $l_w$ is increased. When $l_w$ is increased from 50 to 175 μm, $k$ increased about 135 % from 0.2 to 0.47. This shows that more power is absorbed by the receiver coil with higher line width which has a lower $R_o$ and a higher Q-factor (Table 2.4 and Figure 2.11).

### 2.4.5 Wireless Power Transfer

When the receiver coil is exposed to the magnetic field generated by the transmitter coil, an AC current is generated in the receiver coil which is essentially an LC circuit, due to the electromotive force induced by the field. The power consumed in the receiver coil, $P$, can be expressed as [154];

$$P(\omega) = \frac{R_o v^2}{\left[R_o + j(\omega L - 1/\omega C)\right]^2} \tag{2.6}$$

where $v$ is the electromotive force induced in the receiver coil. The reactance in Equation 2.6 is eliminated when the frequency of the AC current, or that of the magnetic field, matches $f_r$ of the circuit; the angular frequency at the receiver coil, $\omega_r$, can be expressed as $\left(\sqrt{LC}\right)^{-1}$. In this condition, the power transfer to the circuit is maximized, and Equation 2.6 can be rewritten as;

$$P(\omega_r) = \frac{v^2}{R_o}. \tag{2.7}$$

The power in the transmitter coil, $P_T$, is transferred to the receiver coil by way of mutual inductance coupling. The power received at the receiver coil, $P_R$, can be expressed as $P_T\,(M\,/\,L_T)$. Using Equation 2.4, $P_R$ can be rewritten as;

$$P_R = P_T \frac{k\sqrt{L_T L_R}}{L_T} \tag{2.8}$$

and the power transfer efficiency, $\eta$, can be expressed as;

$$\eta = \frac{P_R}{P_T} = k\sqrt{\frac{L_R}{L_T}}. \tag{2.9}$$

In the experimental test, the frequency of the signal supplied to the transmitter, $f_m$, is tuned to $f_r$ of the coil being tested (Tables 2.3 and 2.4). A power of 1 W was fed to the transmitter coil, and each of the receiver coils were aligned with the transmitter coil and placed at 1 mm above the transmitter coil, just as in the measurement of $k$ between the coils. Figures 2.14 and 2.15 plot the measured $v$ at the receiver coils with different $n$ and $l_w$, respectively.

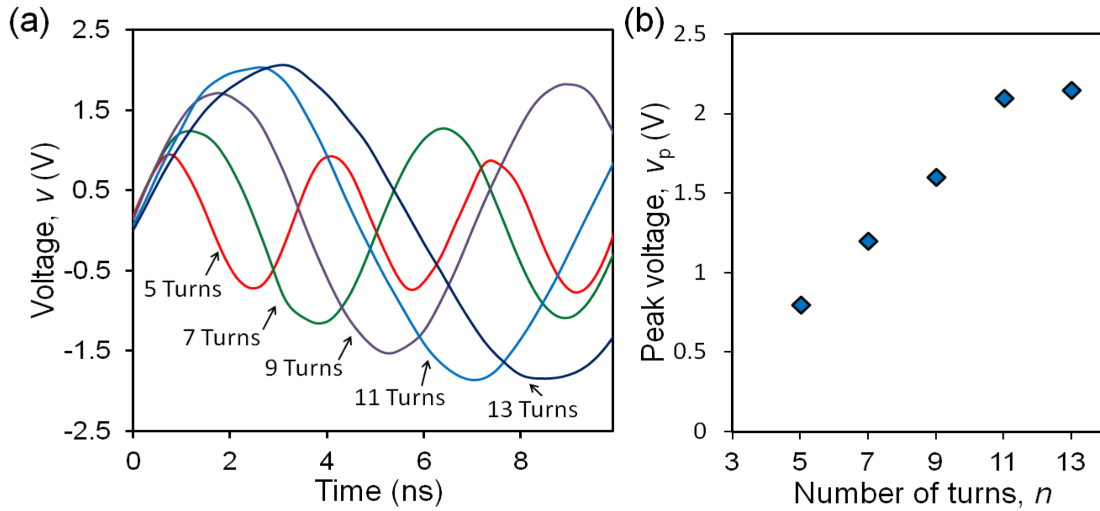


**Figure 2.14:** Voltages measured in the wirelessly powered receiver coil with different numbers of turns; (a) voltage vs. time and; (b) peak voltage ($v_p$) vs. number of turns.

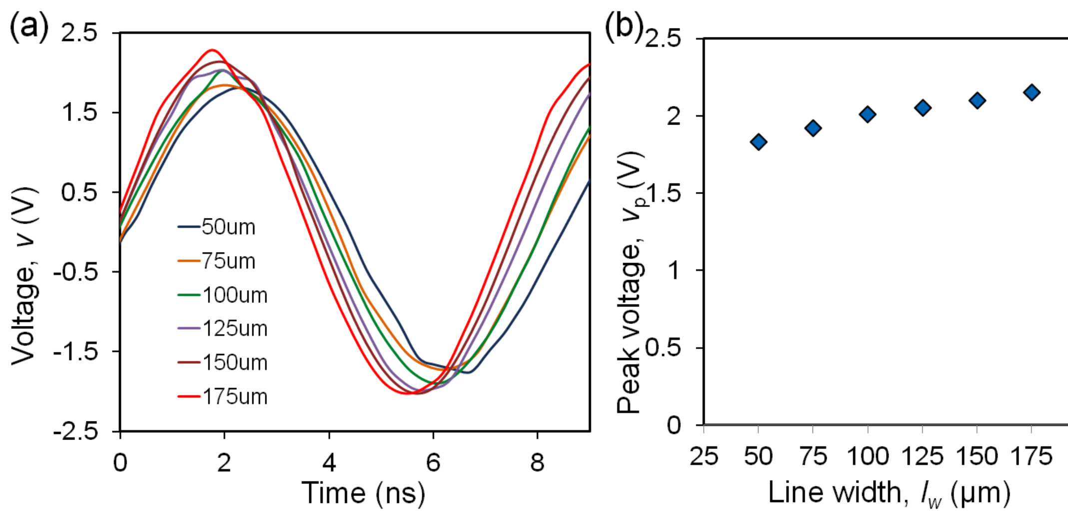


**Figure 2.15:** Voltage measured in the wirelessly powered receiver coil with different fill ratios; (a) voltage vs. time and; (b) peak voltage , $v_p$ vs. line width.

The results plotted in Figure 2.14 show that receiver coils with larger $n$ values induce higher voltages. As can be observed, the coil with $n$ of 5 induces $v_p$ of ~0.8 V, as compared with the coil with $n$ of 7, which induces $v_p$ of ~1.2 V. The coil with $n$ of 13 induces the highest $v_p$ of ~2.1 V. However, the voltage induced in these coil does not differ much as compared with the coil with $n$ of 11 which induces $v_p$ of ~2.05 V. This small difference is caused by the relationship in the size of the receiver coils and the transmitter coil, as described in Table 2.5 earlier. This suggests that, although a large coil can spatially capture or 'interact' with more magnetic fields generated by the transmitter coil, power transfer is not very efficient when the size of the receiver coil exceeds the dimensions of the transmitter coil.

Figure 2.15 shows voltage induced in the receiver coil when the fill ratio is varied by adjusting $l_w$. In this case, the coils with a larger $l_w$ induce higher voltage. However, the voltage result does not reveal a significant change when the line width is altered as compared with the case where $n$ is varied. When $l_w$ is increased from 50 to 175 μm, $v_p$ induced increases from ~1.8 to ~2.2 V which corresponds to a ~22% increase.

Based on the voltage measurement at the receiver coil and the coils' $R_o$ (Table 2.3 and 2.4), the power transfer efficiency, $\eta$ is computed. Both the theoretical and measured value of $\eta$ obtained by comparing the power at the receiver coil with a transmitted power, are plotted for receiver coils with different values of $n$ and $l_w$ in Figure 2.16 and 2.17, respectively. As shown in the plots, both calculated and measured efficiencies display similar trends with some discrepancies. These differences could be caused by some level of errors in positioning alignments of the receiver coils with transmitter coil during the measurement of $k$ and that of wireless power transfer.

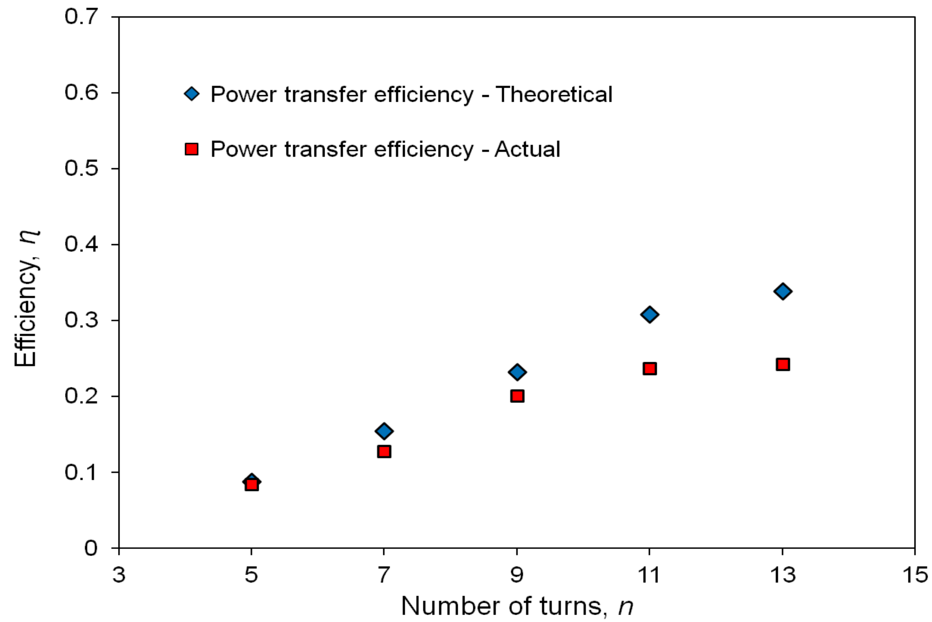


**Figure 2.16:** Power transfer efficiency for receiver coils with different numbers of turns.

The receiver coils with larger *n* numbers resulted in higher power transfer efficiency as shown in Figure 2.16. As can be observed, the power transfer efficiency shows a continuous improvement from ~0.1 to ~0.25 when *n* is increased from 5 to 11. This corresponds to an improvement of ~150 % in the power transfer efficiency. However, there is not much improvement when *n* is further increased to 13 where the measured efficiency is ~0.26, almost the same as the efficiency of coils with *n* of 11, which agrees with the trend of *k* as reported earlier. These results also come to the agreement with Equation 2.9 where $\eta$ proportional to *k*. Although there was a drop in *k* when *n* is increased to 13, the increase in the receiver coil's *L* compensates it and resulted in small increase in $\eta$. This result clearly demonstrates the importance of selection in transmitter and receiver coil sizes.

For coils with different fill ratios, efficiency increases from ~0.1 to ~0.37 with an improvement of 270 % when $l_w$ is increased from 50 to 175 µm as described in Figure 2.17. This shows that coils with larger $l_w$ which corresponds to higher *k* posses higher power transfer efficiency.

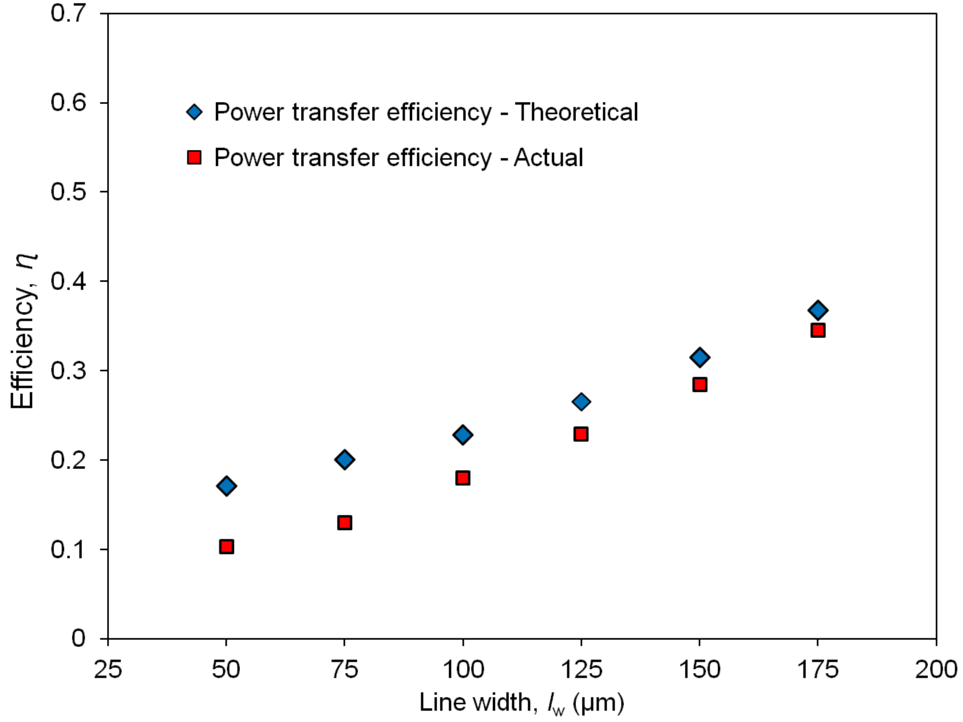


**Figure 2.17:** Power transfer efficiency for receiver coils with different fill ratios.

### 2.4.6 Wireless Heating

When the receiver coil is designed to resonate at the same frequency as the signal in the transmitter coil, the field energy is most effectively converted to Joule heat (Equation 2.7). The steady state temperature rise of the coil, $T_{ss}$, can be theoretically expressed as [155];

$$T_{ss} = \frac{R_T v^2 / R_o}{1 + \alpha_R R_T v^2 / R_o} \tag{2.10}$$

where $R_T$ is the thermal resistance between the heater and the surroundings of the circuit and $\alpha_R$ is the temperature coefficient of resistance of the coil. The heat resistance, $R_T$, is related to the amount of heat that will be retained without loss to the surroundings. There are three heat loss mechanisms that need to consider in thermal devices, i.e., thermal conduction, convection and radiation. Figure 2.18 shows the setup and the heat flow from the heater during the thermal measurement.

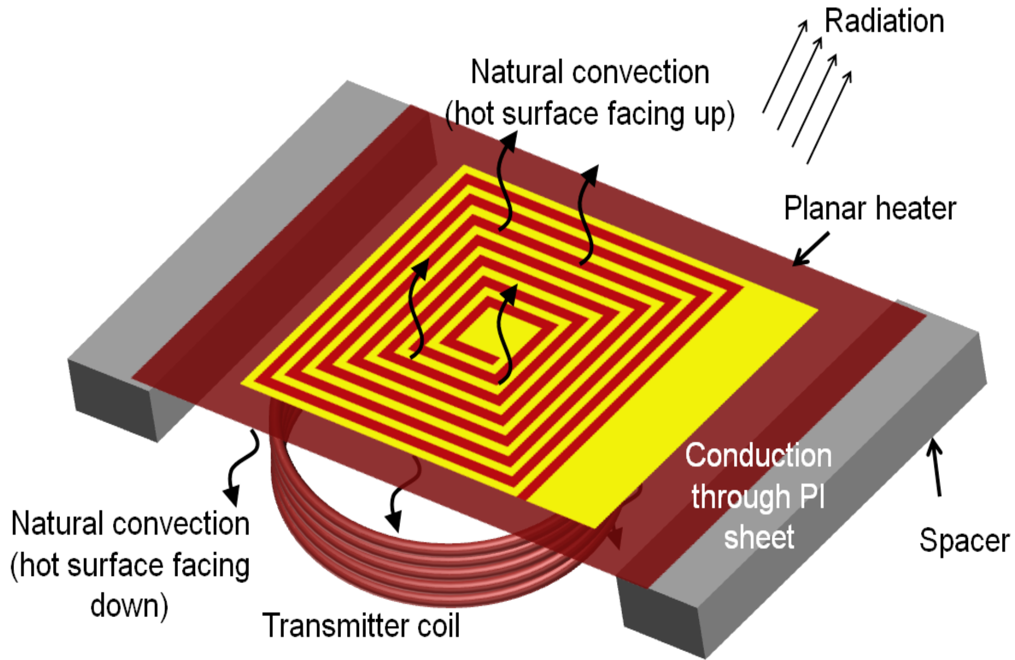


**Figure 2.18:** Heat losses at the planar heater.

## A. Conductive heat transfer

Heat flow through conduction occurs when there is a difference in temperature between the heater and another part that is in contact with the heater. The conduction heat flow, $q_{\mathrm{Cond}}$ is given by [156];

$$q_{Cond} = \frac{\Delta T}{R_{Cond}} \tag{2.11}$$

where $\Delta T$ is the temperature different between heater and the substrate and $R_{\mathrm{Cond}}$ is resistance of thermal conduction. $R_{\mathrm{cond}}$ can be expressed as [156];

$$R_{Cond} = \frac{L_t}{k_p A} \tag{2.12}$$

where $L_t$ is the thickness of the material in the direction of which the heat flows, $k_p$ is the thermal conductivity of the material and the $A$ is the surface area. In this work, the $L_t$ and $A$ correspond to the thickness of the PI (50 μm) and the surface area of the heater respectively.

### B. Convective heat transfer

Convection occurs when the medium that is in contact with the hot surface of a heater is not stationary for example air or liquid. The heat flow through convection, $q_{Conv}$ is expressed as [157];

$$q_{Conv} = h\Delta TA \tag{2.13}$$

where $h$ is the convection heat transfer coefficient. For air, $h$ can be expressed as [157];

$$h = \frac{k_a Nu_L}{L_C} \tag{2.14}$$

where $k_a$ is the thermal conduction of air, $Nu_L$ is the Nusselt number for laminar flow, and $L_C$ is the characteristic dimension [158]. For horizontal plate (e.g. planar heater) $Nu_L$ depends on the face of the heater; hot surface facing up and hot surface facing down [159]. For the hot surface facing up, $Nu_L$ is given by;

$$Nu_L = 0.54 Ra_L^{1/4} \tag{2.15}$$

and for a hot surface facing down, $Nu_L$ is given by;

$$Nu_L = 0.27 Ra_L^{1/4} \tag{2.15}$$

where $Ra_L$ is the Rayleigh number. $Ra_L$ is given by [160];

$$Ra_L = \frac{g\beta\Delta T L_C^{3}}{v\alpha} \tag{2.17}$$

where $g$ is the gravity acceleration, $\beta$ is the thermal expansion of the air, and $v$ and $\alpha$ are the kinematic viscosity and thermal diffusivity of the air respectively. $L_C$ for a horizontal surface is given by [160];

$$L_C = \frac{A_c}{P} \tag{2.18}$$

where $A_c$ is the surface area of the coil and $P$ is the perimeter. The heat resistance due to the natural convection loses, $R_{Conv}$ is given by [161];

$$R_{Conv} = \frac{1}{hA} \tag{2.19}$$

where $A$ is the surface area of the heater. Using Equations 2.14 to 2.19, the convective thermal resistance of the planar heater can be estimated depending on its dimensions.

### C. Radiative heat transfer

Radiation heat transfer is caused by the travel of electromagnetic waves [162]. Thermal radiation occurs in any object that has absolute temperature above 0 K and occurs directly through the components' surface, without any transfer medium. The rate of heat radiation, $q_{Rad}$, is given by [163];

$$q_{Rad} = \varepsilon\sigma A\left(T_1^4 - T_2^4\right) \tag{2.20}$$

where $\varepsilon$ is the emissivity of the surface, $\sigma$ is the Stefan-Boltzmann constant, and $T_1$ and $T_2$ are the temperature of the heater and that of the surrounding respectively.

### D. Conduction, convection and radiation heat loses

The magnitude of the heat loses through all the three heat loss mechanisms described above can be obtained by solving the heat flow equations. The parameters used in the

calculation are given in Table 2.6. The heat flows thorough conduction, convection, and radiation for a planar heater with *n* of 5 are estimated for a temperature range of 20 to 100 °C and plotted in Figure 2.19.

**Table 2.6:** Numerical values used for heat flow calculation.

| Parameter | Symbol | Value | Units |
|---|---|---|---|
| Surface area | A | $9.6\times10^{-6}$ | $m^{-2}$ |
| Thermal conductivity of PI | $k_p$ | 0.12 [164] | W/°C-m |
| Thickness of the PI sheet | $L_t$ | $50\times10^{-6}$ | m |
| Characteristic dimension | $L_c$ | $5.06\times10^{-5}$ | m |
| Gravity acceleration | $g$ | 9.81 | $m/s^2$ |
| Thermal conductivity of air | $k_a$ | 0.024 [157] | W/°C-m |
| Thermal expansion of air | $\beta$ | $3.41\times10^{-3}$[160] | $°C^{-1}$ |
| Kinematic viscosity of air | $v$ | $1.59\times10^{-5}$ [160] | $m^2/s$ |
| Thermal diffusivity of air | $\alpha$ | $2.25\times10^{-5}$ [160] | $m^2/s$ |
| Surface emissivity of Cu | $\varepsilon$ | 0.97 [157] | - |
| Stefan-Boltzmann constant | $\sigma$ | $5.676\times10^{-8}$ | $W/m^2$ |

As can be observed, the heat flow through conduction has the highest magnitude, followed by the natural convection. The loss through radiation is ~1000 times smaller than the heat loss through convection, suggesting very high thermal resistance. Since the radiative and convective losses occur in parallel, in the device of interest, the thermal loss through the radiative transfer is negligible. Although the heat loss through convection is just ~5 % of the conduction, the loss through convection is not negligible in the thermal resistance calculation since it is in series with conduction loss (for hot surface facing down case).

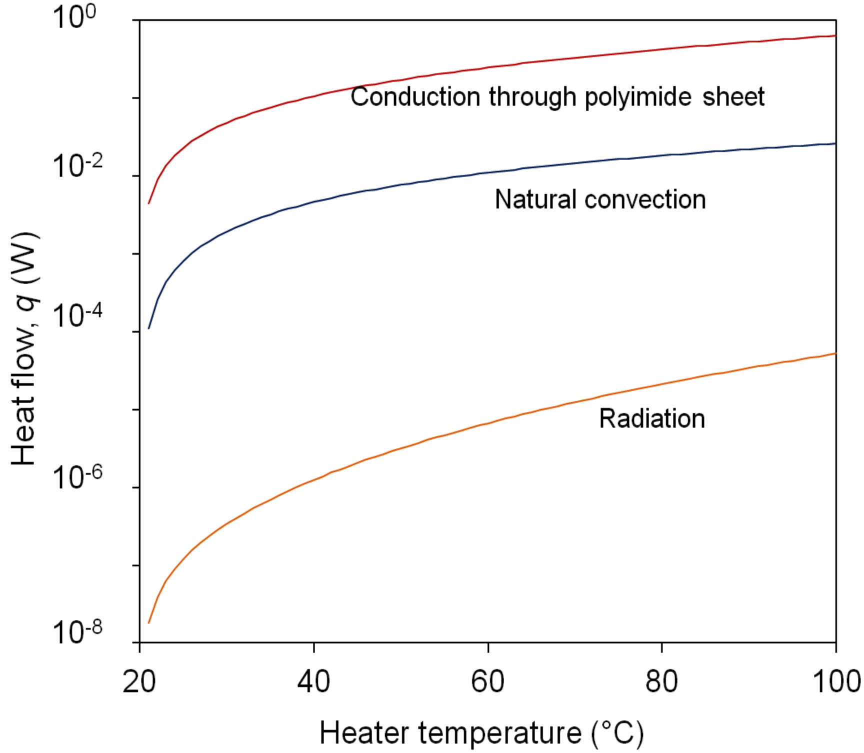


**Figure 2.19:** Comparison of heat flow components in the planar heater.

The surface heat resistance for the planar heater can be calculated based on the Equations 2.12 and 2.19. The conduction heat resistance takes place through the PI sheet substrate that used to form the heater, while the convection heat resistance will take place at top and the bottom surface of the heater as illustrated in Figure 2.18. For a horizontal plate hot surface, the heat resistance on the top surface for natural convection, $R_{\mathrm{Tu}}$ is given by;

$$R_{Tu} = \frac{1}{1.27\Delta T^{\frac{1}{4}} L_c^{-\frac{1}{4}} A} \tag{2.21}$$

assuming a laminar flow. The heat resistance at the bottom surface of the heater, $R_{\mathrm{Td}}$ is expressed as;

$$R_{Td} = \frac{1}{0.637\Delta T^{\frac{1}{4}} L_c^{-\frac{1}{4}} A} + \frac{L_t}{k_p A}. \tag{2.22}$$

The total heat resistance, $R_T$ to the surrounding area is given by;

$$R_T = \left( \frac{1}{R_{Tu}} + \frac{1}{R_{Td}} \right)^{-1}. \tag{2.23}$$

Since the thickness of the PI used as the coil substrate is very low (50 μm), the thermal resistance due to the PI in vertical and lateral direction is negligible. Thus the conductive heat resistance element in Eq. 2.19 may be eliminated to simplify the calculation. The $R_T$ now can be rewritten as;

$$R_T = \frac{0.52}{\Delta T^{\frac{1}{4}} L_c^{-\frac{1}{4}} A}. \tag{2.24}$$

The difference in the temperature $\Delta T$ can be also written as $T_{ss}$, the steady state temperature rise. $T_{ss}$ can be obtained by substituting Eq. 2.11 to Eq. 2.9;

$$T_{ss} = \frac{0.52\left(v^2 / R_o\right)}{T_{ss}^{\frac{1}{4}} L_c^{-\frac{1}{4}} A + 0.52\alpha_R \left(v^2 / R_o\right)}. \tag{2.25}$$

The steady state temperature of the coil, $T_f$ can be computed using;

$$T_f = T_R + \frac{0.52\left(v^2 / R_o\right)}{T_{ss}^{\frac{1}{4}} L_c^{-\frac{1}{4}} A + 0.52\alpha_R \left(v^2 / R_o\right)} \tag{2.26}$$

where $T_R$ is the room temperature. Table 2.7 describes the parameters used in the theoretical analysis of the steady state temperature, $T_f$. $T_f$ is calculated for the coils with different $n$ and $l_w$.

**Table 2.7:** Numerical values used for steady state temperature, $T_f$ calculation.

| Parameter | Symbol | Value | Units |
|---|---|---|---|
| Temperature coefficient of resistance (Cu) | $\alpha_R$ | 0.0043 [165] | °C$^{-1}$ |
| Room temperature | $T_R$ | 20 | °C |
| Resistance | $R_o$ | Table 2.3 and 2.4 | Ω |
| Voltage | $v$ | Figure 2.15 and 2.16 | $V_{RMS}$ |
| Characteristic length of the heater | $L_c$ | Appendix B | m |
| Surface area | $A$ | Table 2.1 and 2.2 | m$^2$ |

Heat generation was experimentally tested by feeding the transmitter coil with 1 W of RF power with the frequency tuned to $f_r$ of the receiver coil being tested (Tables 2.3 and 2.4). The receiver coils were aligned to the transmitter coil and placed at 1 mm above the transmitter coil just as in the measurement of $k$ between the coils, while the temperature was measured using an infrared (IR) thermal camera. The measured and calculated $T_f$ are plotted in Figures 2.20 and 2.21 for the coils with different $n$ and $l_w$ values.

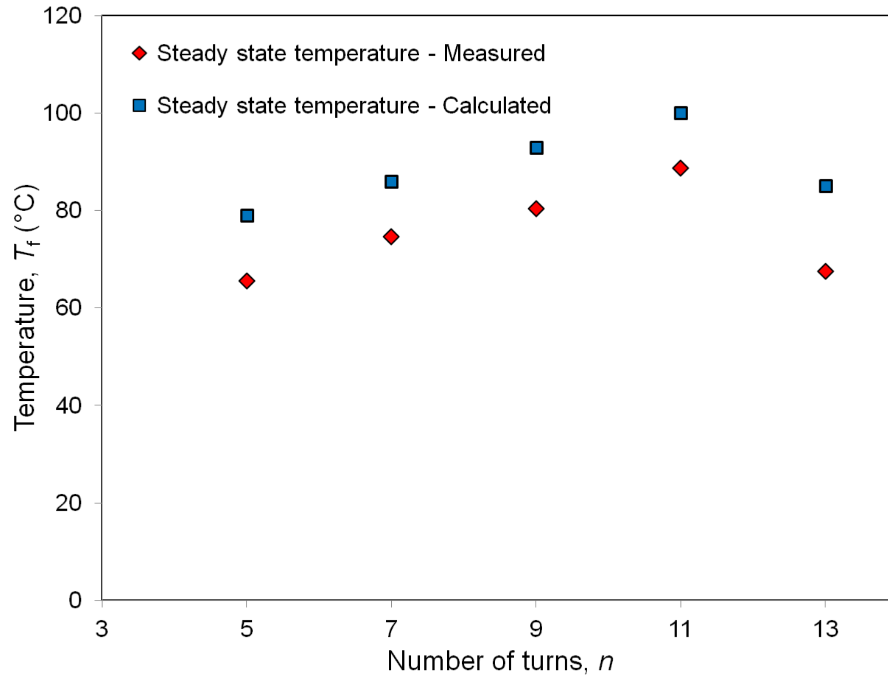


**Figure 2.20:** Steady state temperature of coils with different numbers of turns.

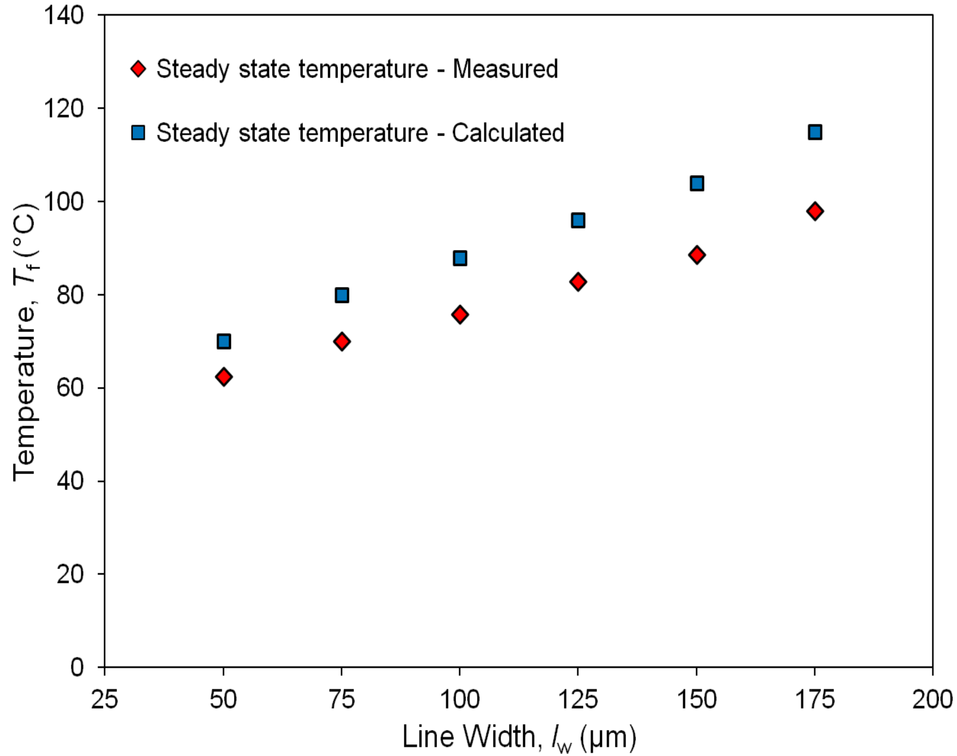


**Figure 2.21:** Steady state temperature of coils with different line widths.

In both of in Figures 2.20 and 2.21, the measured and calculated values have similar $T_f$ trends. As shown in Figure 2.20, $T_f$ increases as $n$ increases. The measured $T_f$ has an increment of ~39 % from 64 to 89 °C when $n$ is increased from 5 to 11. The drop in $T_f$ for coil with $n$ of 13 is mainly caused by the drop in $k$ which resulted in not much increase in $v$ in the coil. In addition, the increase in $R_o$, which increases when $l$ increases, limits the $I$ which is the main contributing element in power generation, $P$. Furthermore, the large area of the coil increasing the amount of heat lost to the surroundings contributes to the drop in $T_f$.

On the other hand, when $l_w$ increases, $T_f$ reveals a continuous increase (Figure 2.21). The measured $T_f$ is increased by about ~68 % from 62 to 98 °C when $l_w$ is increased from 50 to 175 µm. This significant increase in $T_f$ is due to the continuous improvement in $k$ and reduction in $R_o$ value when $l_w$ is increased. As described earlier, $I$ has an inverse proportion relationship with $R_o$. When $R_o$ is reduced, $I$ induced in the coil is increases. This contributes

to the higher resistive heating in the coil. The discrepancy between the measured and calculated $T_f$ in Figures 2.20 and 2.21 is may be related to the model used, which was assumed to neglect the heat loss by the conduction in the lateral direction (through the spacers).

### 2.4.5 Distance Characterization

The increase in the distance, $d$ between transmitter and receiver coils affects the power transfer efficiency due to the reduction in $k$. To characterize this relationship between $d$ and $k$, a coil with $l_w$ of 175 μm and $n$ of 10 was tested for $d$ of ~0 mm to 10 mm and results are plotted in Figure 2.22. The maximum coupling of 0.48 was observed when the receiver coil is placed within 0-1 mm from the transmitter coil. A significant drop was observed when $d$ between the transmitter and receiver coils was increased beyond 2 mm and almost no coupling existed between the coils when $d$ was increased to 7 mm and above.

The power transfer to the receiver coil was measured using the same setup as described in the precious sections. The transmitter coil was fed with 1-W of RF power with $f_m$ which was set at $f_r$ of the coil. The measured $v$ at the receiver coil, and the measured and calculated $\eta$ are plotted in Figure 2.23. A maximum $\eta$ of 0.37 was obtained when the receiver coil was within $d$ of 0 to 1 mm from the transmitter coil. An exponential decay in the measured $v$ and $\eta$ was recorded when the coil was moved more than 2 mm from the transmitter coil. The efficiency dropped to ~0 when the coils were separated at $d$ of more than ~7 mm. The measured $v$ and $\eta$ agrees with the trend of $k$ as plotted in Figure 2.22.

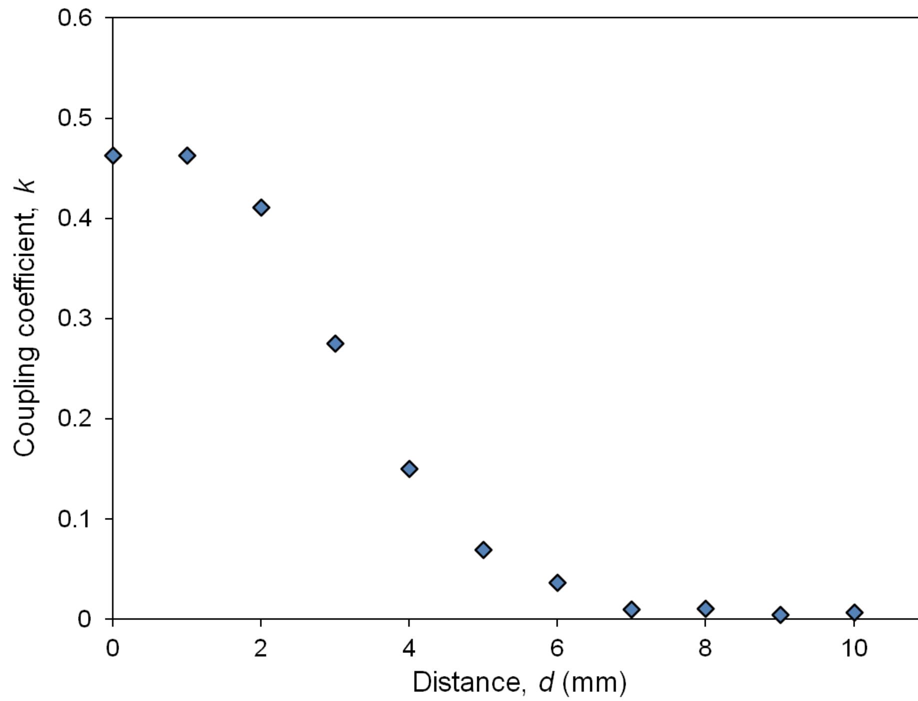


**Figure 2.22:** Coupling coefficient vs. distance of the transmitter and receiver coils.

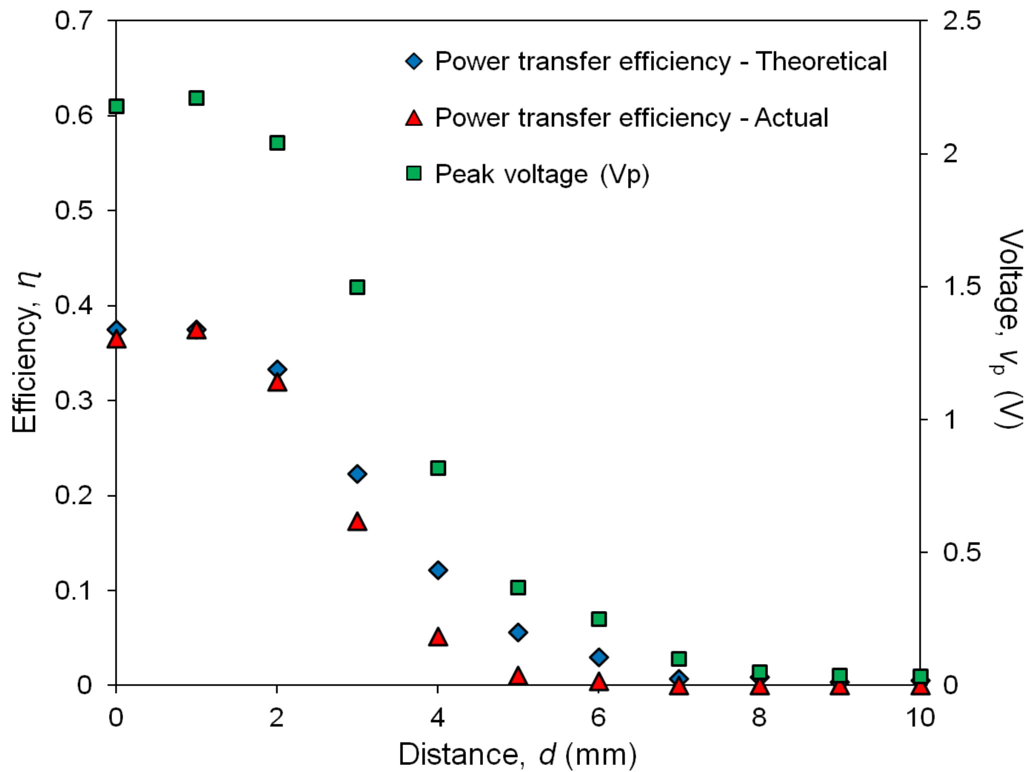


**Figure 2.23:** Calculated and measured efficiency and measured voltage vs distance.

The calculated and measured $T_f$ values are plotted in Figure 2.24. The highest $T_f$ of ~100 °C was recorded when the receiver coil is placed within $d$ of 0 to 1 mm from the transmitter coil. When $d$ was increased from 2 to 4 mm, $T_f$ dropped drastically from 87 to 34 °C. At $d$ beyond 6 mm, the coil does not show any response in terms of temperature rise. This shows that the operating range of the coil tested is from 0 to 5 mm and for efficient operations, $d$ must be kept within 0 to 2mm. The operation range of the heater could be improved by employing a larger transmitter and receiver coils.

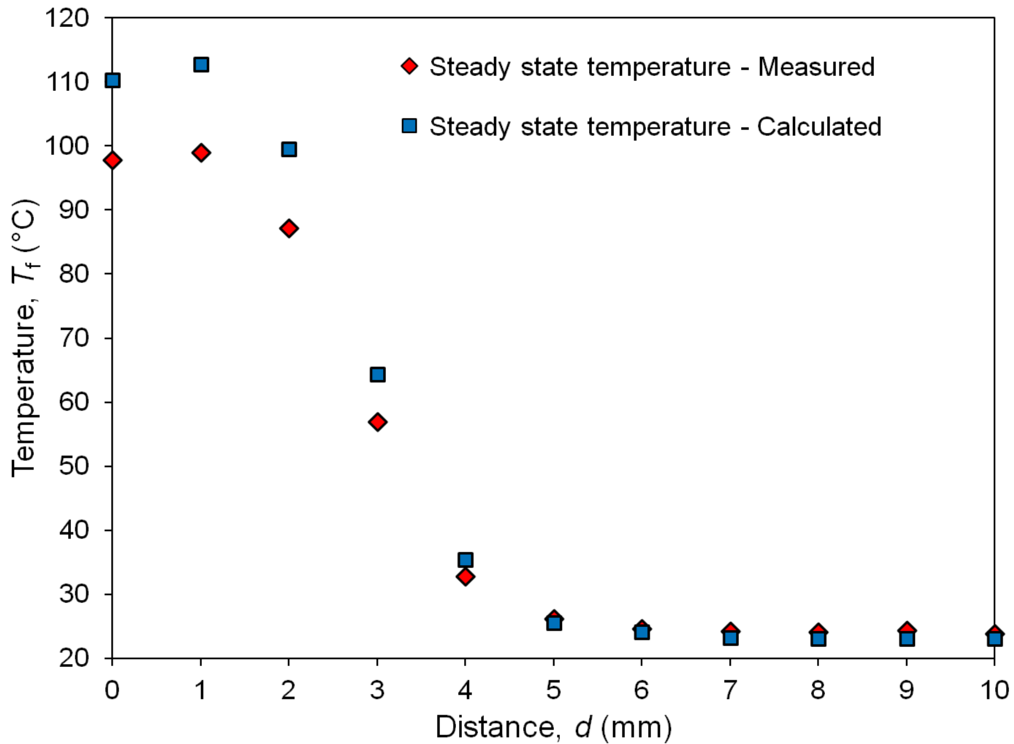


**Figure 2.24:** Steady state temperature of the coils when distance is increased.

## 2.5 Conclusion

This chapter discusses passive wireless heating using LC resonant circuits. The working principle, design, and modeling of the wireless heater is presented and experimentally

verified. The LC circuits with different $n$ and $l_w$ are fabricated and tested to evaluate $\eta$ and heat generation due to resistive heating. Maximum $\eta$ of ~0.37 is reported when a coil with $n$ of 10 and $l_w$ of 175-µm is used hence possesses the highest $T_f$. The measured $T_f$ and the theoretical estimation show similar trends in both coil sets with different $n$ and $l_w$. This resonant wireless heating provides a high frequency selectivity heating and could serve as a unique and effective path to wirelessly drive or control thermoresponsive actuators such as SMA actuators.

# Chapter 3

# A Wireless Bulk-Micromachined Shape-Memory Alloy Microgripper and the Integration Method

## 3.1 Introduction

This chapter[1] discusses the wireless control of bulk-micromachined SMA actuators using external RF magnetic fields and its application to microgrippers. The microgrippers are passively controlled through RF power transfer to resonant heater circuits (discussed in Chapter 2) with which the SMA actuators are coupled. In order to address the issues involved in SMA bonding, a batch-compatible planar assembly technique based on photo-defined selective electroplating is developed and used to bond the SMA actuators to heater circuits. Gripper devices employing the above mentioned SMA actuation method and possessing a one-way memory principle are designed and microfabricated using the developed bonding technique, and the devices have been experimentally characterized in this effort. The manipulation of vertically aligned carbon-nanotube (CNT) forests is presented as a demonstration of RF control of fabricated devices. This chapter also describes the mechanical strength provided by the bonding technique, along with its effects under different sample conditions.

[1] A version of this chapter has been published in a peer-reviewed journal (Reused with permission from "M. S. Mohamed Ali and K. Takahata, 'Frequency-Controlled Wireless Shape-Memory-Alloy Microactuators Integrated using an Electroplating Bonding Process,' *Sensors and Actuators A: Physical*, 163(1), pp 363-372, 2010", Copyright 2010, Elsevier) [166].

Parts of this chapter were also presented in The Solid-State Sensor, Actuator and Microsystems Workshop (Hilton Head 2010), Hilton Head Island, South Carolina, USA [167].

## 3.2 Working Principle of the Device

The micromachined SMA actuator developed in this effort is operated through an LC resonant circuit that serves as a frequency-sensitive wireless heater activated by an external RF magnetic field (Figure 3.1(a)) as demonstrated and characterized in the preceding chapter. Here, the heat generated at the frequency sensitive LC resonant heater is used to drive the SMA actuator i.e., the actuation is controlled with the frequency, rather than the field intensity.

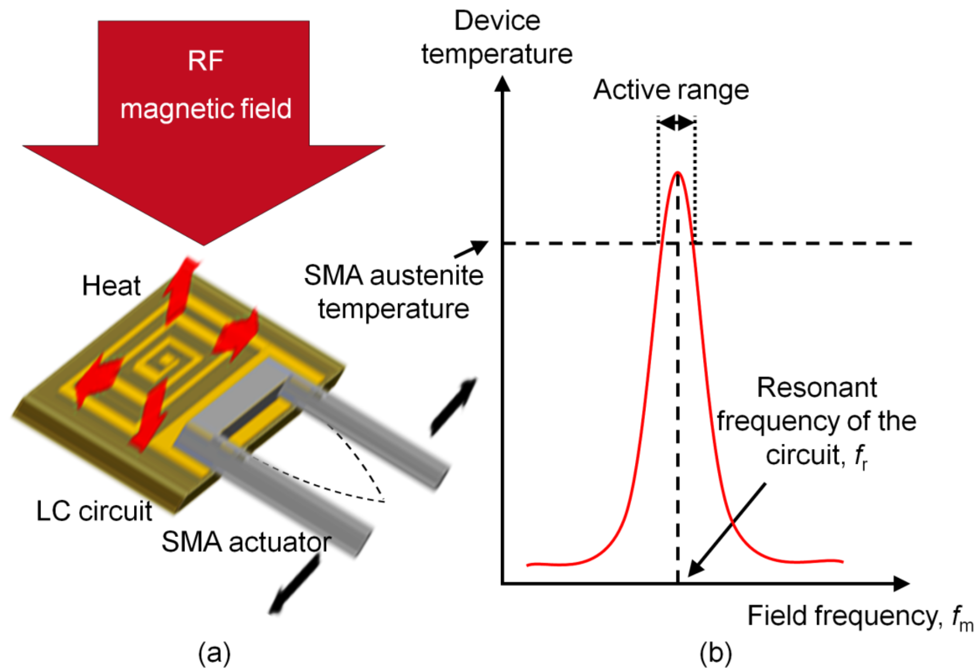


**Figure 3.1:** (a) Wirelessly controlled SMA micro-gripper and (b) working principle of the device.

The SMA gripper with two beams that have an identical rectangle cross section is fabricated so that one of the sidewalls of each of the beams is coated with the cold-state reset layer. When the temperature of the device exceeds the austenite-phase temperature of the SMA, the gripper is actuated as the material returns to its remembered shape (Figure 3.1(b)). The shape of the gripper will be restored to be the cold-state original shape when heat is

removed due to the force provided by the reset layer. The electroplating-based bonding method developed in this study (discussed in Section 3.5) is used to achieve not only high-precision assembly of the micromachined SMA gripper on the wireless heater with high mechanical bonding strength but also high thermal conductance between the two components.

## 3.3 Design and Fabrication

The grippers developed in this effort have a normally closed design with the gripper-beam length of either 4 mm (device-1) or 5 mm (device-2). The layout of the SMA gripper structure is shown in Figure 3.2(a). The gripper structures are formed using a 300-μm-thick Ti-Ni sheets with an austenitic-phase temperature of 65 °C (Alloy M, Memory Metalle GmbH, Germany). The outer sidewall of each of the two gripper beams is coated with a compressive $SiO_2$ layer. The dimensions of the gripper structures are summarized in Table 3.1. These configurations and dimensions for the two devices were determined using a finite element analysis (FEA) tool (COMSOL Multiphysics 3.5a) to ensure that bending of the beams is large enough to close the gripper at its cold state. (For example, the gap spacing of 570 μm between the beams for device-1 was determined by the total theoretical displacements of 582 μm obtained in the analysis for the device; the analysis utilized the data reported in [170] for temperature-dependent material properties such as CTE and Young's modulus for Nitinol.) The SMA components are configured to have a bonding pad with a cavity and perforations as shown in Figure 3.2(a). The LC circuit has a planar spiral coil with an overall size of 5×5 $mm^2$ and the line width and spacing indicated in Figure 3.2(b). The SMA component is bonded on either one of the capacitor electrodes of the LC circuit (as in Figure 3.2) or a separate Cu region located on the backside of the spiral coil that provides heat to the SMA through the bonded region.

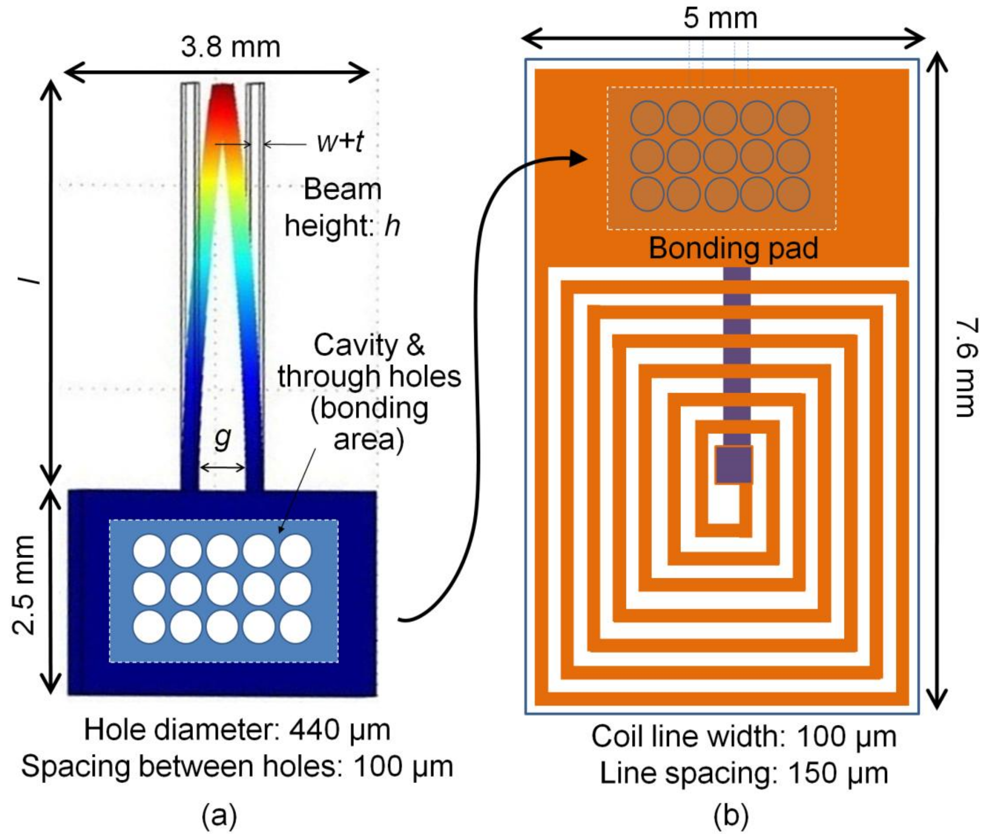


**Figure 3.2:** (a) The SMA gripper design and (b) a sample layout of the LC circuit design.

**Table 3.1:** The dimensions of the gripper structures.

| Dimensions | Device-1 | Device-2 |
|---|---|---|
| Beam length, *l* (mm) | 4 | 5 |
| Beam width, *w* (μm) | 62 | 70 |
| Beam height, *h* (μm) | 300 | 300 |
| $SiO_2$ thickness, *t* (μm) | 3 | 4.2 |
| Gap spacing between beams, *g* (μm) | 570 | 600 |

Figure 3.3 shows the developed fabrication process for the case that the SMA component is bonded on the capacitive electrode of the circuit. The planar LC circuit is fabricated using single-sided Cu-clad PI film with 50-μm thickness same as described in Chapter 2. The

photolithography for the circuit fabrication is performed with dry-film photoresists (15-μm-thick MacDermid SF306 and 38-μm-thick DuPont PM240).

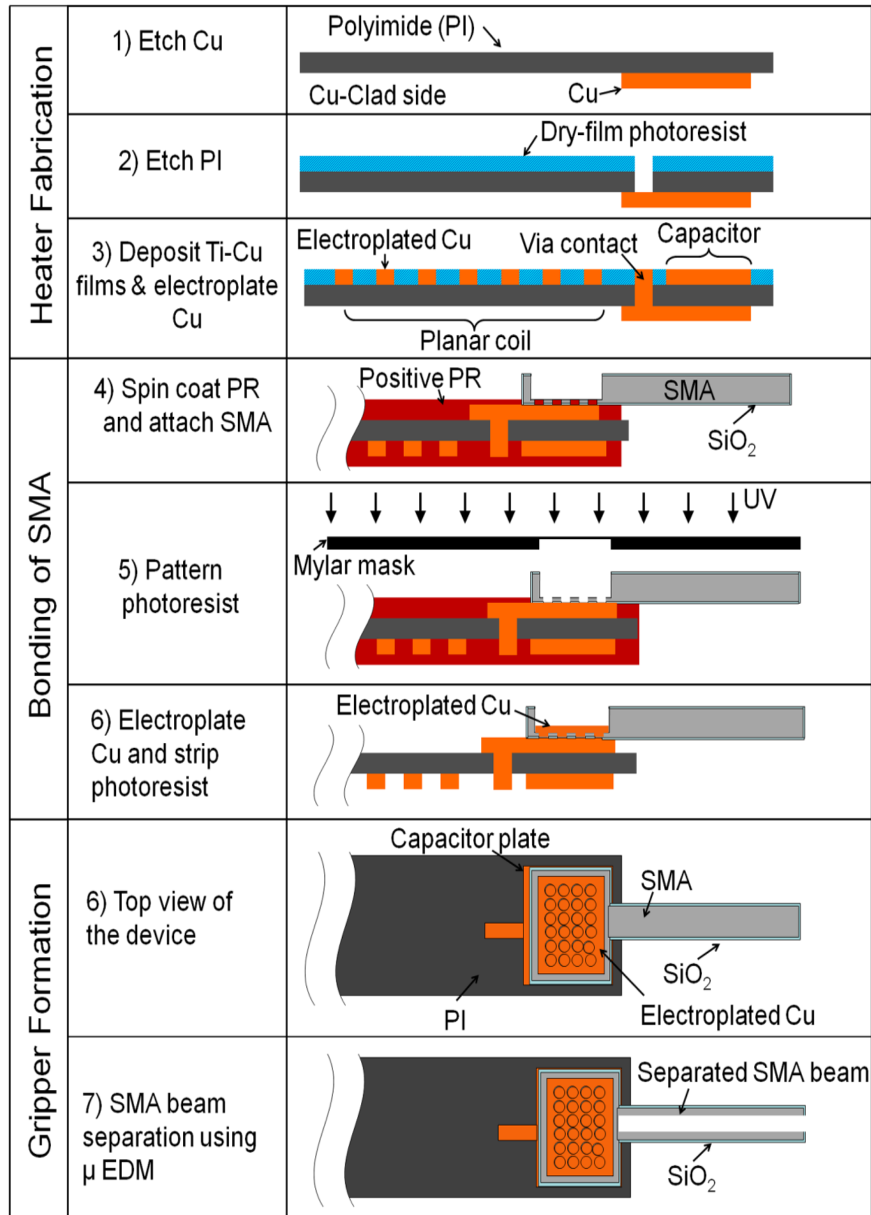


**Figure 3.3:** Fabrication process flow (cross-sectional view except steps 6 and 7).

First, one of the capacitor electrodes is formed by wet etching of the Cu-clad layer by using patterned SF306 photoresist as a mask (Figure 3.3, step 1). Next, the PI film is etched

using a KOH-based solution to create the via contact hole in the film (Figure 3.3, step 2). After depositing a CuTi-Cu seed layer on the PI side, Cu electroplating in the patterned PM240 photoresist mold is performed in a sulfuric-acid-based bath at a current density of 32.3 mA/cm$^2$ for 30 minutes to form the coil and the other capacitor electrode with a thickness of 30-35 μm (Figure 3.3, step 3).

Figure 3.4(a) shows the fabricated LC circuits. Both the circuits in the figure were measured to have the same inductance of 292 nH and different capacitances of 15.6 pF (left circuit) and 9.4 pF (right circuit) due to the different electrode sizes, providing $f_r$ of 74.5 MHz and 96 MHz, respectively.

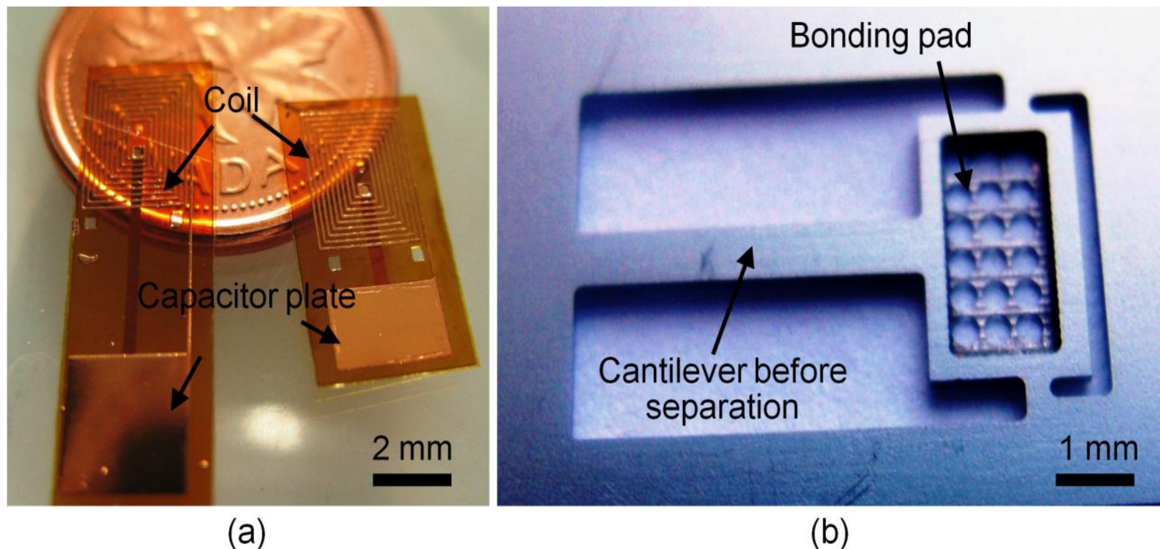


**Figure 3.4:** (a) Samples of the LC resonant circuit fabricated using Cu-clad PI film, and (b) an SMA gripper component fabricate with μEDM (prior to separation from the original sheet).

For the SMA gripper fabrication, the gripper component is first shaped to have the single beam structure in a piece of the SMA sheet by micro-electro-discharge machining process using a commercial system (μEDM, EM203, SmalTec International, IL, USA) [168, 169] μEDM. The machining was performed at voltage level, capacitance, and tool rotation speed of

100 V, 3.3 nF, and 3000 rpm, respectively. This is followed by the deposition of a $SiO_2$ layer that serves as the reset layer using plasma-enhanced chemical vapor deposition (PECVD) at 350 °C on each side of the SMA piece. The thickness of $SiO_2$ in each deposition is set to be a half of the final thickness of the layer listed in Table 3.1 so that the sidewalls of the beam have a $SiO_2$ layer with the target thickness upon the completion of the two-step depositions. The SMA component is then μEDMed to create the bonding pad with the cavity and perforations (Figure 3.4(b)). This μEDM step removes the $SiO_2$ layer from the pad region. The bonding pad of the SMA is fixed onto the capacitive electrode on the Cu-clad side of the circuit coated with photoresist (SPR 220-7) that is used as a temporary adhesive (Figure 3.3, step 4). The photoresist is then soft baked for 10 minutes at 90 °C, followed by the lithography to remove the photoresist in the pad region (Figure 3.3, step 5).

Cu electroplating is then performed with the condition described above in the pad region to grow 120-μm-thick bonding structures (Figure 3.3, step 6); Cu grown from the capacitor electrode through the pad's perforations is over-plated and connected to the portion plated on the pad, mechanically fixing the pad. In this step, the $SiO_2$ layer on the SMA beam acts as a mask for electroplating so that Cu is only deposited on the cavity of the SMA and on the capacitor electrode through the perforations in the cavity.

Figure 3.5(b) shows the pad of the SMA gripper component bonded on the circuit with this electroplating process. Finally, the single beam of the SMA is split into two beams using μEDM (Figure 3.3, step 7) to form the gripper structure with vertical sidewalls (Figure 3.5(a)). These split beams consequently have inner sidewalls without $SiO_2$ layers, resulting in bending and closing their tips due to the compressive $SiO_2$ layer present on the outer sidewalls of the beams. The final form of the device is shown in Figure 3.5(c).

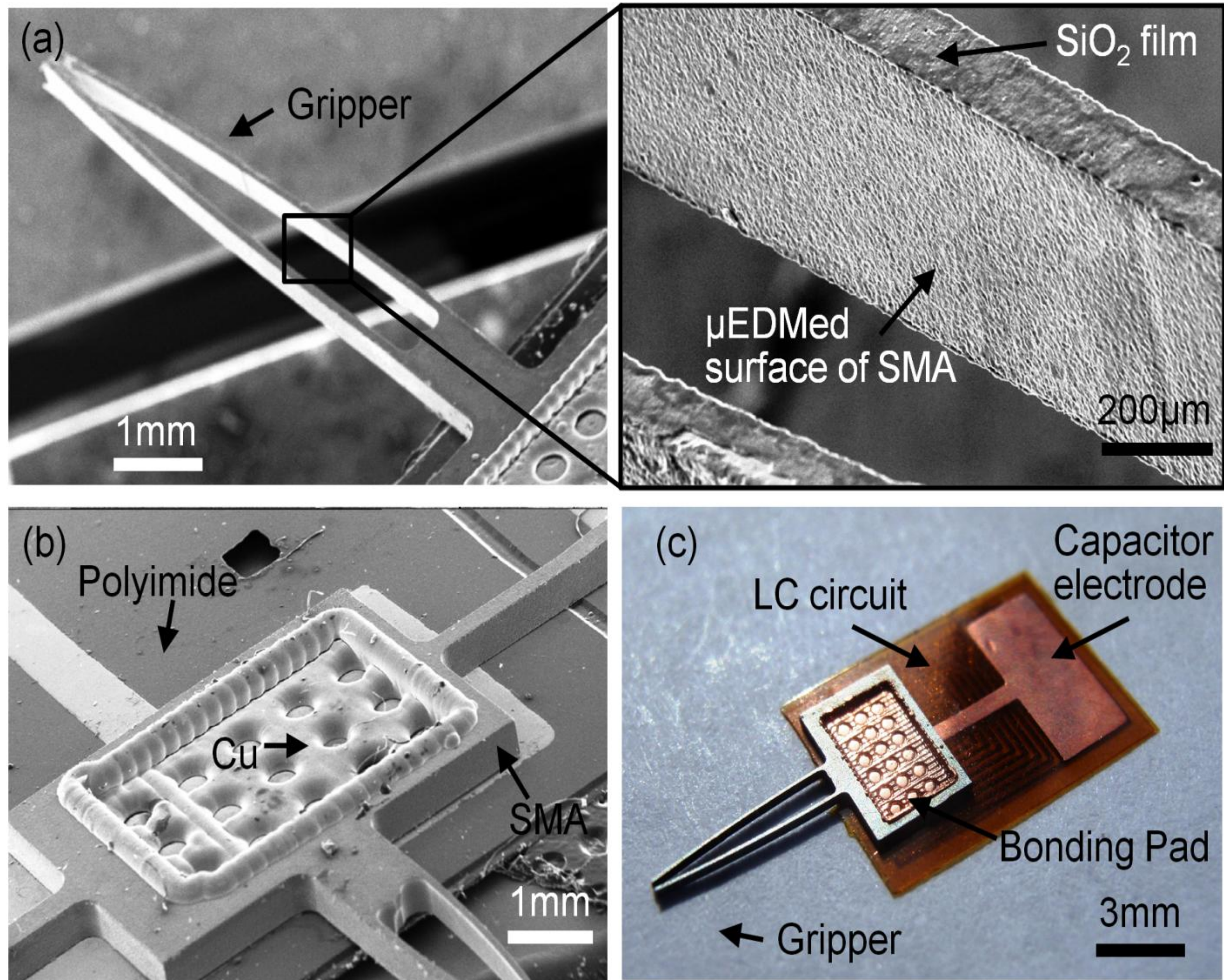


**Figure 3.5:** Fabrication results for device-1 (4-mm-long gripper): (a) Gripper beams split using μEDM and a close- up of the inner sidewall of the beam; (b) the SMA pad bonded by electroplated Cu; (c) overall shape of a fabricated device.

## 3.4 Experimental Results and Discussion

The characterization and experimental results for the SMA and fabricated devices are presented in this section. The performance of the devices is evaluated through wireless actuation tests as well as the manipulation of CNT samples. The results of the bonding strength characterization are also presented and discussed in this section.

### 3.4.1 SMA Phase Transition Characteristics

In order to predict behaviors of the fabricated devices, the SMA material used for the fabrication was characterized using a differential scanning calorimeter (DSC Q1000, V9.0, build 275, Universal 4.1 D, TA Instruments, DE, USA) that measures the phase transformation temperatures by detecting changes in heat flow through the material. The sample was encapsulated in the aluminum pan and scanned at 20 °C/min in both heating and cooling modes, analyzing the temperatures of austenitic start ($A_s$) and finish ($A_f$) as well as martensitic start ($M_s$) and finish ($M_f$). A typical measurement result is shown in Figure 3.6.

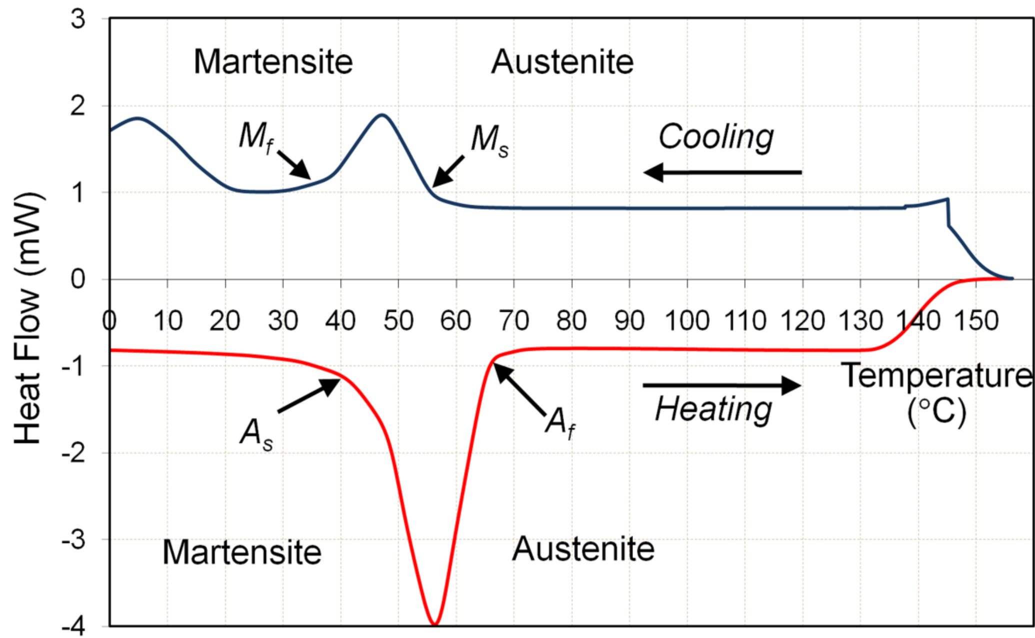


**Figure 3.6:** Measured heat flow vs. temperature for the SMA material used for the device fabrication.

It can be seen in the result that $A_s$, $A_f$, $M_s$, and $M_f$ for the SMA are approximately 40, 65, 55, and 35 °C, respectively. This indicates the transformation temperature hysteresis of 5-10 °C for the material.

### 3.4.2 Wireless Actuation Tests

Wireless tests for the fabricated devices were experimentally performed using the set-up illustrated in Figure 3.7. In this set-up, an amplified RF signal with an output power of up to 1 W was fed to the external coil (diameter ~6 mm, 497-nH inductance) to generate an RF magnetic field that excites the LC circuit of the device. The thermomechanical behavior of the gripper was characterized using a thermocouple that was attached to the devices (on the capacitor electrode of the circuit located on the opposite side of the electrode bonded with the SMA) as well as a measuring microscope with a resolution of 0.1 μm to characterize the displacement of the gripper. It was experimentally verified that the dependence of thermocouple reading on the presence of the magnetic field with the power level and frequencies used in the tests was minimal or undetectable.

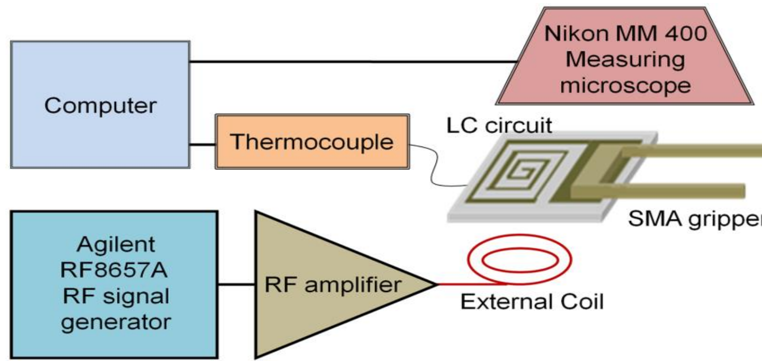


**Figure 3.7:** A set-up for wireless actuation tests and demonstration.

Figure 3.8 shows a typical response of device-2 (5-mm gripper). The device's LC circuit's $f_r$ was measured to be 140 MHz (with $L$ = 184 nH and $C$ = 7 pF). The circuit temperature and gripper displacement (tip opening) were simultaneously measured while scanning $f_m$ from 120 MHz to 155 MHz at a constant output power of 0.2 W in this case. The measurement results show a strong temperature peak (of 100 °C) when $f_m$ was aligned to $f_r$ which agrees with the

result reported in Chapter 2. The results also indicate that the gripper was activated and deactivated at about 48 °C and 37 °C, respectively, resulting in the active frequency range (to which the device responds) of 13 MHz, and that the maximum opening of 600 μm was reached and started to drop at about 92 °C and 68 °C, respectively.

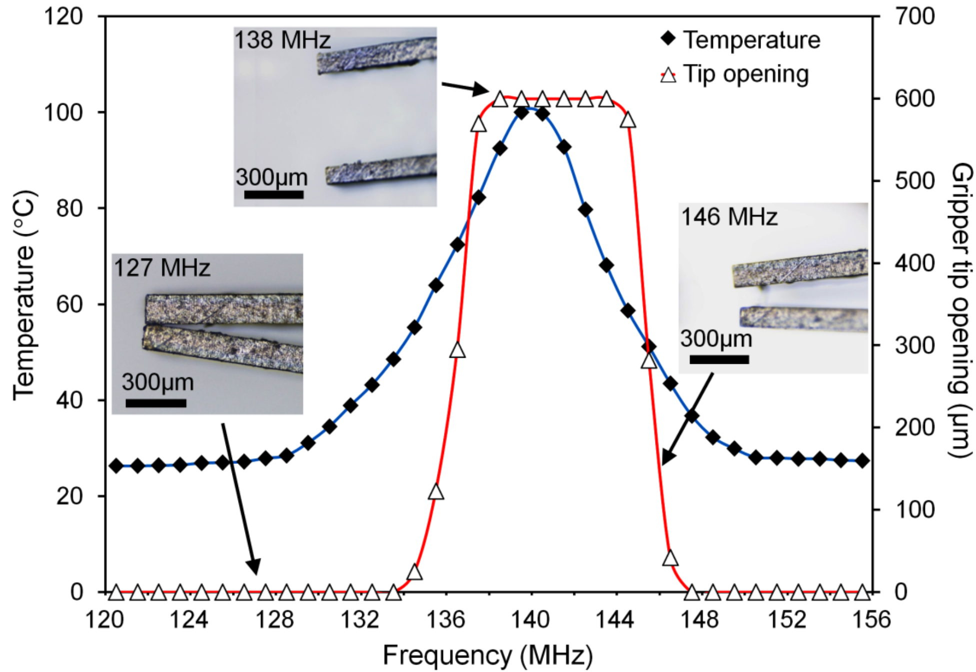


**Figure 3.8:** Measured circuit temperature and gripper openings vs. $f_m$ (inset images show tip openings of the gripper at corresponding frequencies).

It can be seen that these four measured temperatures, which in order correspond to $A_s$, $M_f$, $A_f$, and $M_s$, respectively, tended to be higher than the measured phase transition temperatures of the material used (refer to Section 3.4.1). This is most likely because the temperature was probed on the circuit at a distance from the SMA; in this case, the actual temperatures of the SMA are anticipated to be lower than the measured values in Figure 3.8 due to heat loss occurred between the probing location and the SMA. Comparing the temperature values from Figures 3.6 and 3.8, the gradient between the heater circuit and the gripper is suggested to be around 27 °C (the difference between the measured $A_f$ in Figure 3.6 and the corresponding

temperature in Figure 3.8 noted above) or less. Figure 3.9 shows measured circuit temperature and opening distance of the gripper tips when temporal excitation of the device was performed using an external field with 0.2-W output power at 140 MHz that matched $f_r$ of the device.

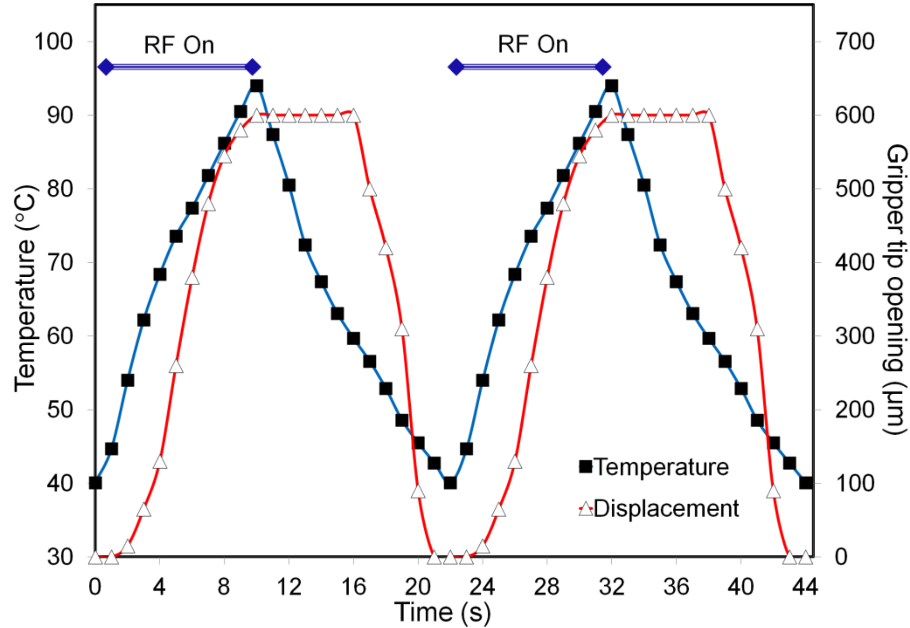


**Figure 3.9:** Measured circuit temperature and gripper actuation with a temporal application of an external RF magnetic field whose frequency was aligned to $f_r$ of the circuit.

As can be seen, the time for the gripper to achieve the maximum opening of 600 μm (at 94 °C) from its fully closed state (at 40 °C) after the field was turned on was approximately 9 seconds, whereas the time that the gripper returned to the fully closed state after the field was turned off was approximately 5 second. This suggests that the gripper may be operate for the full-range actuation at a frequency of ~0.07 Hz for this device. The time response of the actuation depends on the RF output power used for the device excitation as well as the device design/size including the SMA material (i.e. its austenitic-phase temperature) used.

The RF control of the gripper devices was demonstrated using samples of CNT forests. For this test, a gripper device with the same $f_r$ of 140 MHz was attached to a micro positioner

(Manipulator 750, Signatone Co., CA, USA) that was used to manually position the gripper device relative to a CNT forest sample. Figure 3.10(a) shows that the gripper approaches the forest sample while keeping the device temperature to be ~60 °C with $f_m$ of 135 MHz. In Figure 3.10(b), the device temperature is increased to ~70 °C by tuning $f_m$ closer to $f_r$ of the device, and the gripper continues to approach the sample. In Figure 3.10(c), the gripper makes contact with the CNT forest, and the tips are closed to grab a part of the forest by shifting $f_m$ to 150 MHz, bringing the device temperature down to 27 °C. From Figure 3.10(d) to Figure 3.10(e), the gripper is moved apart from the forest sample while gripping the part of the forest and continues to be pulled until the gripped part is separated from the sample. Figure 3.10(f) shows that the gripper holds the separated forest part that is manipulated through the above frequency-controlled gripping process.

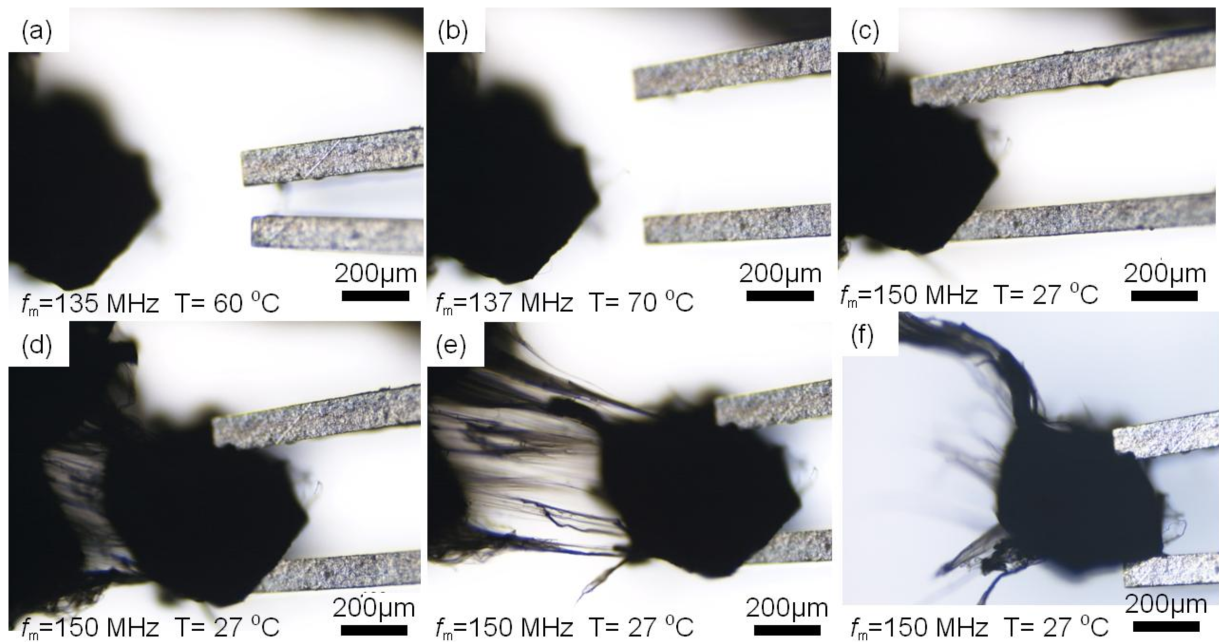


**Figure 3.10:** Manipulation of CNT forest: (a) Approaching the forest; (b) tips opened by tuning $f_m$ closer to the device's $f_r$ of 140 MHz; (c) making contact with the forest, and the tips closed by shifting $f_m$ to 150 MHz; (d) gripped part of the forest pulled; (e) the forest part continues to be pulled; (f) gripper holds the separated forest part.

## 3.5 SMA Integration and Characterization

It is important to understand the bonding strength available with the developed electroplating method in light of its application to MEMS and other micro mechanical devices. The adhesion strength of electroplated Cu films was characterized with peeling tests [171, 172]. The present study focuses on the shear strength of electroplated Cu microstructures formed by the developed method that was used to bond SMA components to Cu-clad PI substrate in this effort.

### 3.5.1 Characterization of Bonding Strength

The strength was experimentally characterized using a force gauge (UWE HS-30K, Intelligent Weighing Technology Inc., CA, USA) attached to a vertical positioning stage (Figure 3.10(a)). The layout of the samples used for this test is shown in Figure 3.10(b); each SMA component machined from a 300-μm sheet had two 440-μm-diameter perforations with 100-μm spacing in the 280-μm-deep 1×2-mm$^2$ cavity. Each SMA component was bonded to a Cu-clad PI substrate through the two perforations where Cu is electroplated for a thickness of 120 μm using the process described in Section 3.3. The sample placement is illustrated in Figure 3.11(a); a portion of the PI substrate was clamped down to the base of the stage and bent by 90° so that the SMA was directed upward and fixed to the force gauge. For each sample, shear forces applied to the sample were measured with the gauge while displacing the gauge along the upper direction using a micrometer until the bonding failed.

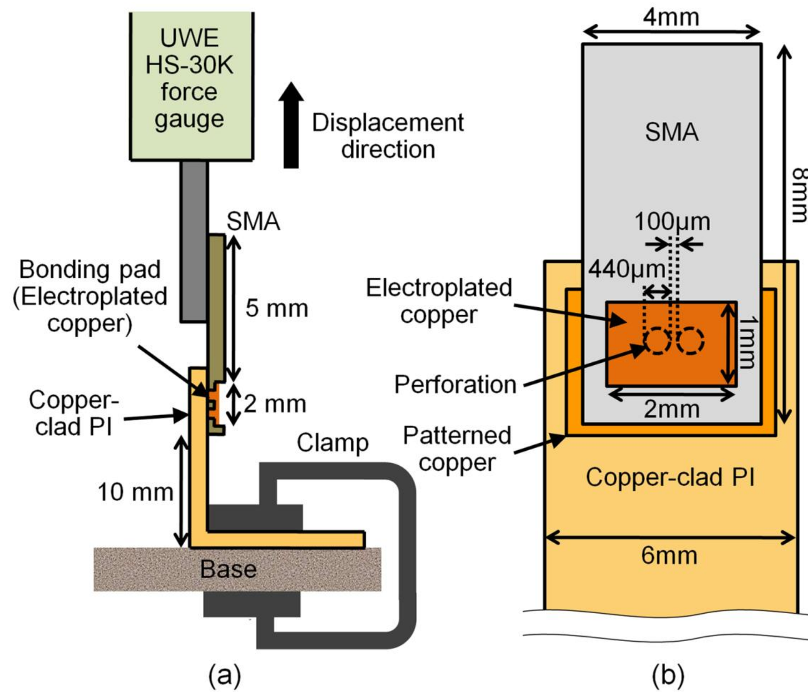


**Figure 3.11:** Measurement of shear bonding strenth: (a) Cross-sectional view of the measurement set-up; (b) layout of SMA samples used for the measurement.

In order to evaluate the effect of the $SiO_2$ insulation layer coated on SMA in the bonding process, samples with the $SiO_2$ layers (type-A) and without the layers (type-B) were prepared for the measurement. The type-A samples had the same configuration as the SMA gripper components used for the device fabrication, i.e., all the surfaces were first coated with $SiO_2$ then the cavity was machined to form the bonding pad (thus no $SiO_2$ on the bonding-pad surfaces) in each sample. The results from two samples identically fabricated for each type are plotted as a function of the displacement in Figure 3.12. As can be seen in the graph, the type-A samples with the $SiO_2$ layer provided much higher shear strengths than those with the type-B samples. The type-A samples were broken at 10.6-12.2 N, which correspond to shear strengths of 34.8-40.1 MPa calculated using the total area of the two perforations (0.304 $mm^2$). The type-B samples were observed to exhibit shear strengths of only 19.3-21.3 MPa.

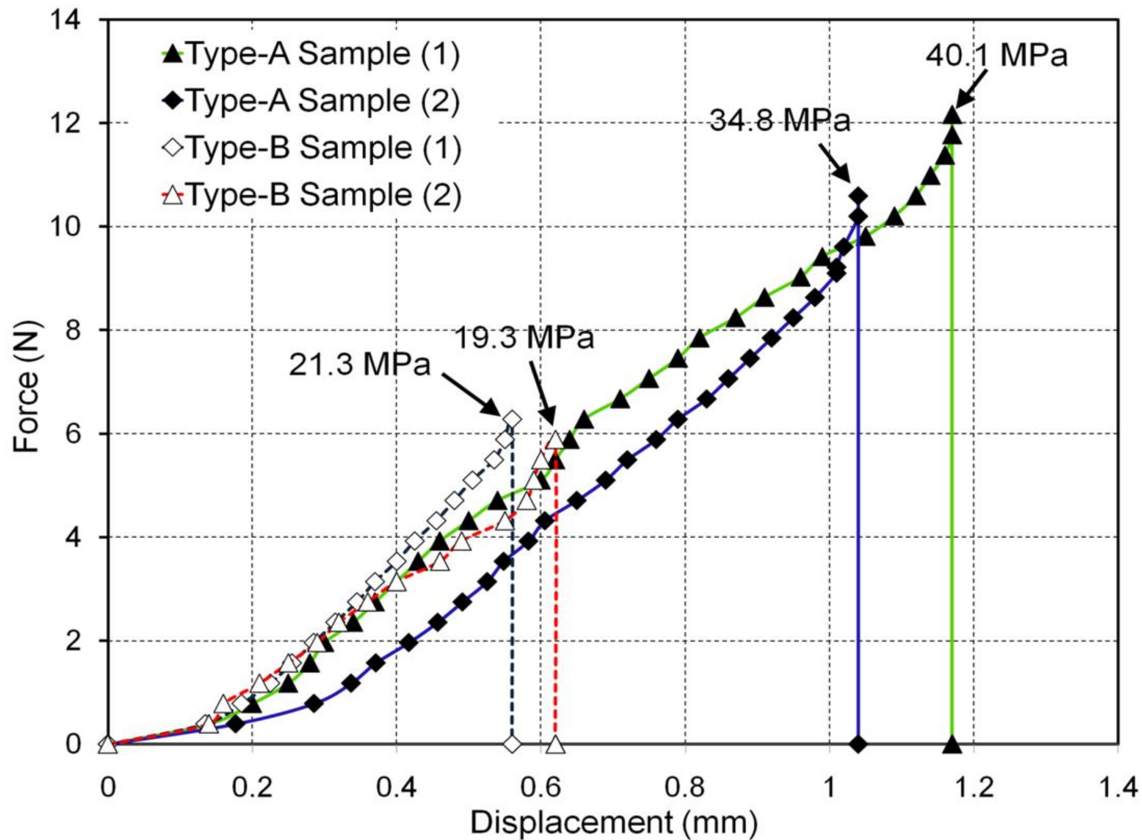


**Figure 3.12:** Measured shear forces vs. displacement for type-A (with $SiO_2$ layer) and type-B (without the layer) samples, showing the shear strengths calculated using the bonding surface area of 0.304 $mm^2$.

### 3.5.2 Effect of the Silicon Dioxide Layer in Bonding

It was discovered that this large difference in the bonding strength between the two types was attributed to the forms of Cu structures resulted from electroplating in the SMA perforations. Figures 13(a) and 13(b) show the broken interface structures of electroplated Cu seen on the backside of the SMA perforation and on the top surface of the Cu-clad PI substrate, respectively. It can be seen in Figure 3.13(a) that the Cu structure formed on the perforation has a bowl-like shape with the top opening narrowed by the grown Cu structure, whereas Figure 3.13(b) indicates a cone-shaped bump formed on the Cu-clad surface.

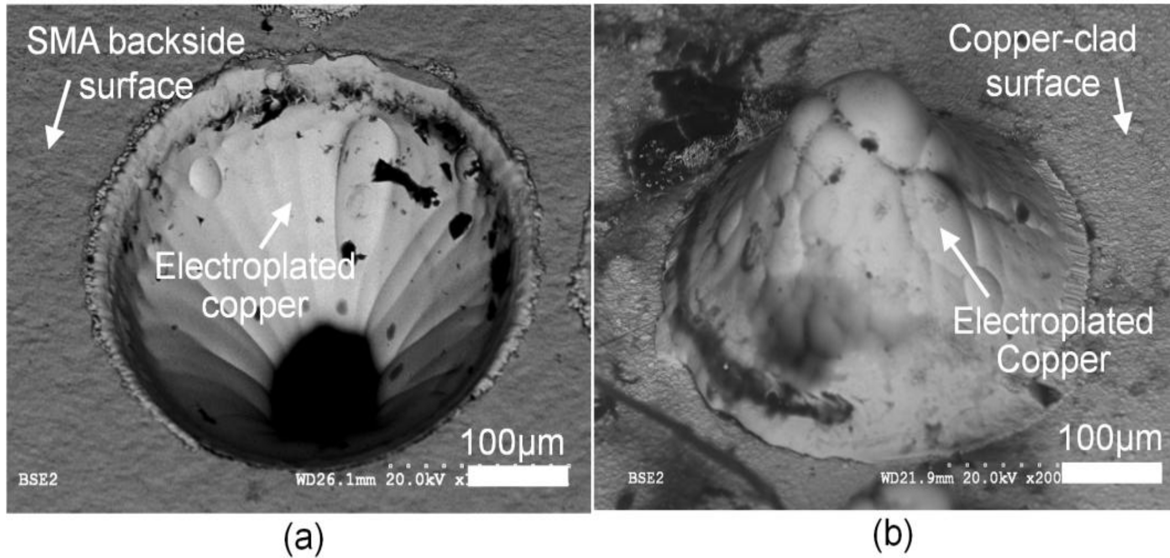


**Figure 3.13:** SEM images of the broken interface in a type-B sample: (a) The backside of the SMA showing the bowl-like electroplated Cu structure grown from the edges of the perforation narrowing the opening; (b) the electroplated Cu bump structure formed on the Cu-clad layer underneath the bowl-like structure in (a).

With this observation, as well as the fact that the SMA of type-B samples is electrically short circuited to the substrate because there is no $SiO_2$ layer present on the SMA, it is evident that Cu quickly grows on the SMA, which tends to close the top opening of the perforation, preventing further plating on the Cu-clad surface as illustrated in Figure 3.14(b).

In contrast, the SMA of type-A samples is initially isolated from the substrate due to the presence of the $SiO_2$ layer, prohibiting the Cu growth on top of the SMA and around the perforations. As the Cu structures in the perforations grow, they short circuit the SMA to the substrate and then Cu starts to grow on the SMA as well. With further plating, the Cu layer grown on the SMA is combined with the over-plated structures grown through the perforations, forming a solid, continuous bonding structure as shown in Figure 3.14(a).

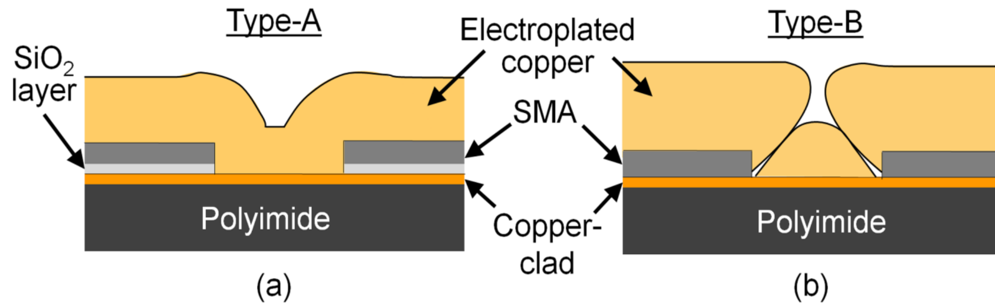


**Figure 3.14:** Cross-sectional diagram of Cu structures in (a) the type-A sample (with $SiO_2$ layer) and (b) the type-B sample (without the layer) formed by the electroplating bonding process.

The broken interfaces of the type-A samples indicate that the mechanical failure occurred at the interface between the Cu-clad layer and the PI substrate, not at the bonding interface (Figure 3.15). This means that the actual bonding strength is greater than the values (34.8-40.1 MPa) obtained in this test and that the bonding method provides adhesion strengths that are considerably greater than those available with the polymer-adhesive techniques mentioned earlier, which are reported to be approximately in the range of 8-30 MPa.

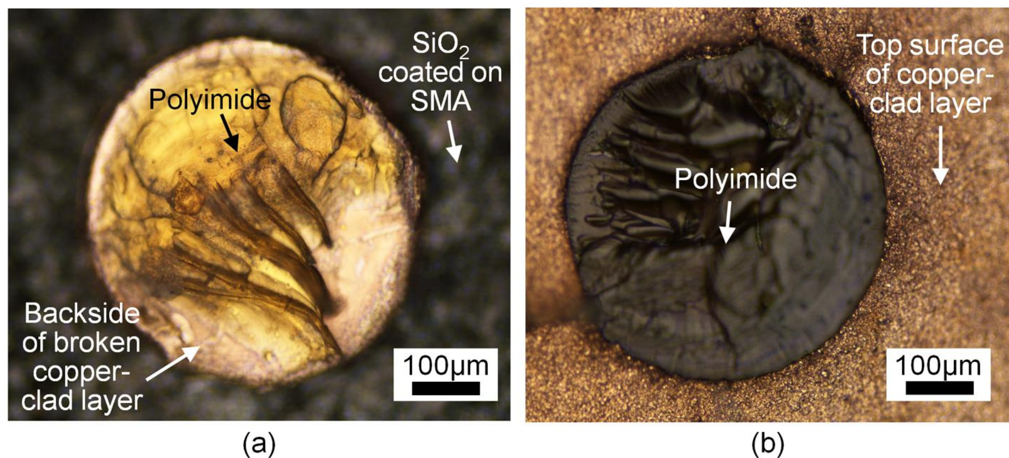


**Figure 3.15:** Optical images of the broken interface in a type-A sample: (a) $SiO_2$ surface on the SMA showing that the portion of Cu-clad layer bonded to the SMA through the Cu structure electroplated in the perforation came off (together with some parts of PI) with the SMA when bonding failed; (b) the Cu-clad layer where the failure occurred showing the PI surface exposed.

## 3.6 Conclusion

A fully passive, bulk-micromachined SMA gripper that is controlled using external RF magnetic fields has been developed. A normally closed SMA gripper with 4- or 5-mm length was coupled with a planar resonant LC circuit with a 5×5-mm$^2$ spiral coil that functions as a frequency-selectable wireless heater. The heater was activated only when the $f_m$ was tuned to $f_r$ of the LC circuit. An electroplating-based planar bonding technique was developed to achieve mechanical and thermal coupling of the SMA gripper components with the wireless heater circuits. The bonding strength tests revealed that the technique provided the strength of at least 40 MPa, which is greater than those provided with most polymer bonding methods. The operations of the fabricated grippers were successfully implemented through the RF frequency-tuning principle. The devices exhibited the tip opening of 600 μm when $f_m$ was at the heater's $f_r$ or nearby within a range of 6 MHz with a constant RF output power of 0.2 W. Frequency-controlled wireless gripping and manipulation of carbon nanotube forests were demonstrated. The frequency selectivity of the device provides an opportunity to implement simultaneous control of multiple SMA actuators that are bonded to the wireless heaters with different $f_r$; this aspect is investigated and reported in the next chapter. The developed bonding technique based on photo-defined electroplating may be leveraged for the microfabrication of arrayed SMA actuators by scaling up the technique.

# Chapter 4

# Selective Wireless Control of Shape-Memory Alloy Actuators using Frequency Modulation and its Microfluidic Application

## 4.1 Introduction

In Chapter 3, a wireless control of a single SMA actuator using RF magnetic field was demonstrated. This chapter[2] discusses the wireless microfluidic control enabled by the selective operation of multiple bulk-micromachined SMA actuators using external RF magnetic fields. Fully passive, integrated SMA microactuators that can be selectively controlled through field-frequency modulation is reported to show the feasibility of RF wireless actuation method to control multiple SMA actuators. The actuators' temporal and thermal responses are experimentally characterized. For the application of microfluidic devices including *in-vivo* drug-delivery applications, a prototype wireless microsyringe/injector device with ejection-amount controllability enabled by multiple-actuator control has been developed. Wireless control of liquid's pH level using a fabricated device is performed as an experimental demonstration of the developed RF actuation technique.

---

[2] A version of this chapter has been published in a peer-reviewed journal (Reused with permission from "M.S. Mohamed Ali, K. Takahata, 'Wireless Microfluidic Control with Integrated Shape-Memory-Alloy Actuators Operated by Field Frequency Modulation' *Journal of Micromechanics and Microengineering*, vol. 21, 2011, 075005 (10pp), 2011", Copyright 2011, IOP) [173].

Parts of this chapter were also presented in a proceeding (Reused with permission from M.S. Mohamed Ali, K. Takahata, Selective RF Wireless Control of Integrated Bulk-Micromachined Shape-Memory-Alloy Actuators and Its Microfluidic Application, *Proceeding IEEE MEMS*, Mexico, Jan 23-27, 2011, pp. 1269-1272", Copyright 2011, IEEE) [174].

## 4.2 Device Principle and Design

As discussed in Chapters 2 and 3, the *LC* circuit effectively produces heat when exposed to an AC magnetic field with $f_m$ that matches $f_r$ of the circuit [166, 167]. If multiple heaters are designed to have different $f_r$, one or more heaters, or SMA actuators coupled with them, can be selectively and simultaneously activated by modulating $f_m$ to the corresponding $f_r$ values in a time-sharing manner (Figure 4.1(a)).

When the temperature of the actuator exceeds the austenite-phase temperature of the SMA, the SMA is actuated as the material returns to its remembered shape (Figure 4.1(b)). The frequency-modulation pattern and excitation interval time are adjusted so that the achieved temperatures of the excited SMA structures exceed the threshold temperature using a fixed output field power high enough to reach the temperature. The shape of the actuator is restored to its original cold-state shape when heat is removed due to the force provided by the reset layer deposited on the SMA.

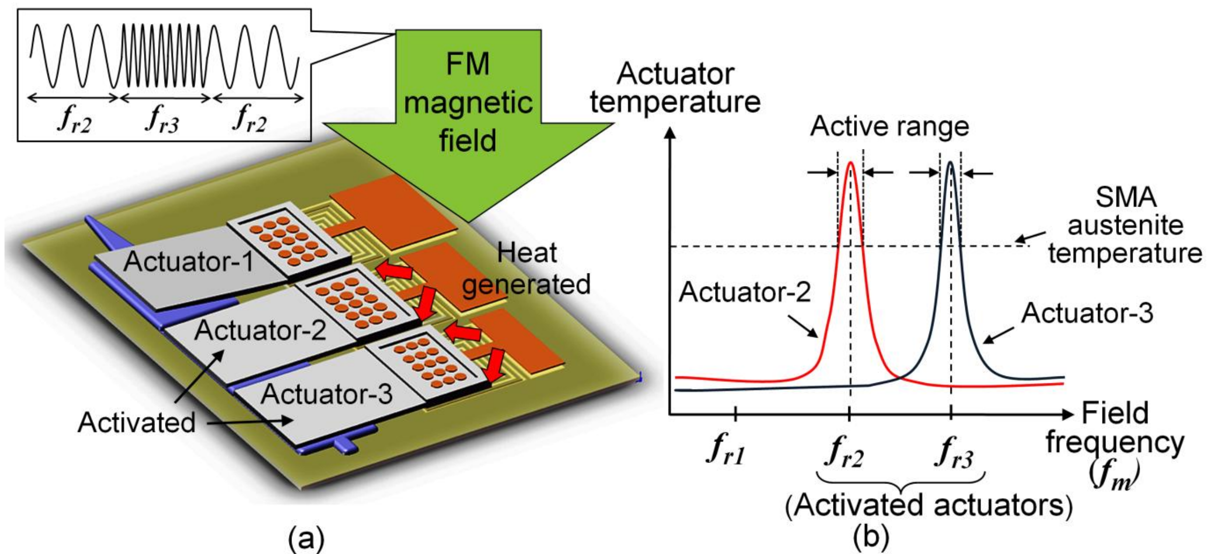


**Figure 4.1:** Working principle: In this example, Actuators-2 and -3 are selectively activated by modulating $f_m$ to $f_r$ of the two wireless heaters ($f_{r2}$ and $f_{r3}$) coupled with the actuators.

As a proof of concept, a microsyringe device was designed and developed (Figures 4.1(a) and 4.2(a)). In this device, a flexible reservoir filled with a selected liquid/gel is squeezed by three cantilever-type SMA actuators with identical dimensions (5 mm length and 4.1 mm width) arranged in an array to eject the fluid. The ejection amount is controlled by the number of actuators activated. Each SMA cantilever is micromachined to have a bonding cavity with perforations (Figure 4.2(a)), which are used to permanently bond the SMA cantilever onto the copper pads located on the backside of the coils using the electroplating bonding technique developed for the SMA structure assembly as reported in Chapter 3. The excited coil provides heat to the SMA for its actuation through the electroplated bonding region. The excited coil provides heat to the SMA for its actuation through the electroplated bonding region. A reservoir with a thickness of 130 μm is created on the backside of the coil as well, so that an array of the SMA actuators is arranged above the reservoir when the array is bonded to the circuits. The SMA structures are bulk micromachined in 300-μm-thick Ni-Ti sheets with an austenitic-phase temperature of 65 °C. The bottom side of the SMA is coated with a compressive reset layer at a temperature greater than 65 °C so that the layer is deposited on the flat cantilever at a trained state. After the deposition, at room temperature, the SMA cantilever will bend due to the compressive stress applied by the reset layer, and it returns to the trained flat shape when heated to a temperature greater than 65 °C. The dimensions of the actuator and the thickness of the reset layer are determined by analyzing the actuator's displacements using COMSOL Multiphysics$^{TM}$ 3.5a (Figure 4.2(b)).

The finite element analysis is to ensure that the cold-state bent SMA cantilever will have a space large enough to accommodate the reservoir underneath when bonded to the substrate. The wireless heater component is essentially an array of three *LC* tanks with the planar spiral coils that have an identical overall size of 3.8×4.4 mm$^2$ (theoretical inductance ~95 nH). The

$f_r$ values of the circuits are differentiated with an approximate separation of 30 MHz by varying the size of the capacitors of the tanks. This relatively large frequency separation was selected to minimize the cross talk between the tanks. Theoretical values of the capacitance and $f_r$ of the three tanks are indicated in Figure 4.2(a).

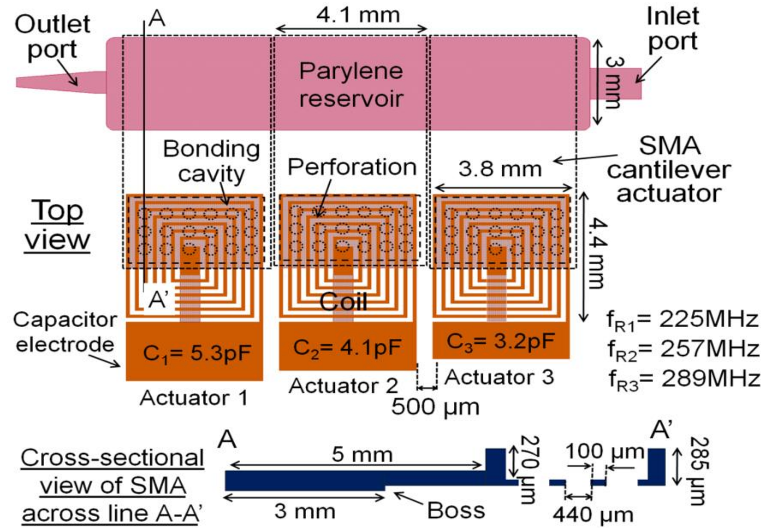


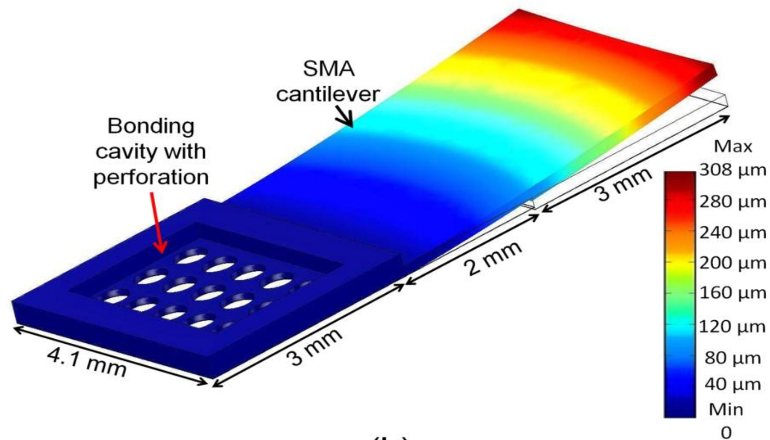


**Figure 4.2:** (a) The microsyringe/injector design; (b) A COMSOL model of the SMA actuator showing an approximate displacement of 300 μm at the free end due to the force provided by a 3.5-μm-thick $SiO_2$ layer on the backside of the SMA, indicating the space created underneath the actuator large enough to accommodate the 130-μm-thick parylene reservoir.

## 4.3 Device Fabrication

Figure 4.3 shows the fabrication process developed for the device. The planar *LC* circuit is fabricated using single-sided Cu-clad PI film with 50-μm thickness; details of this process (Figure 4.3(a), steps 1-3) were reported in Chapter 3. After electroplating Cu for the coil formation, the Cu seed layer is etched away, leaving the titanium layer that will be used to provide the electrical connection for the later electroplating bonding of SMA using the process discussed in the preceding chapter. (The Cu layer needs to be etched before the SMA bonding as the Cu etchant, ferric chloride solution, attacks the SMA.) A 130-μm-thick sacrificial mold for the reservoir formation is created on the backside of the substrate with three layers of spin-coated photoresist (SPR 220-7) (Figure 3(a) step 4). The photoresist mold is then hard baked for 2 hours at 120 °C. Figure 4.4(a) shows the patterned photoresist mold with the Cu-clad capacitor electrodes and bonding pads formed on the PI substrate. The reservoir walls are formed by depositing 10-μm-thick Parylene-C (Specialty Coating Systems, IN, USA). To improve the parylene adhesion, the surfaces of the PI substrate is roughened using $O_2$ plasma at 100 W for 3 minutes prior to the parylene deposition. (The adhesion promoter $H_2O$: IPA: A-174(γ-methacryloxypropyl trimethoxy silane) commonly used for parylene attacks the sacrificial photoresist.) The parylene layer on the electroplating bonding pads for the SMA assembly is dry etched using a photoresist mask (Figure 4.3(a), step 4).

For the fabrication of the SMA-actuator array (Figure 4.3(b)), a 300-μm-thick plate of the SMA noted in the previous section is first etched in hydrofluoric-nitric acid (HNA) solution (5wt% Hydroflouric acid and 30wt% Nitric acid mixed in DI water) [33] for 15 minutes to form a 15-μm-high boss structure (to be located at the tips of the cantilever actuators – Figure 4.2(a)) using a laminated dry-film photoresist mask (Figure 4.3(b), step 1). This boss is

necessary to compensate the thickness of the bonding pad on the substrate so that the SMA cantilevers achieve complete squeezing of the reservoir when actuated.

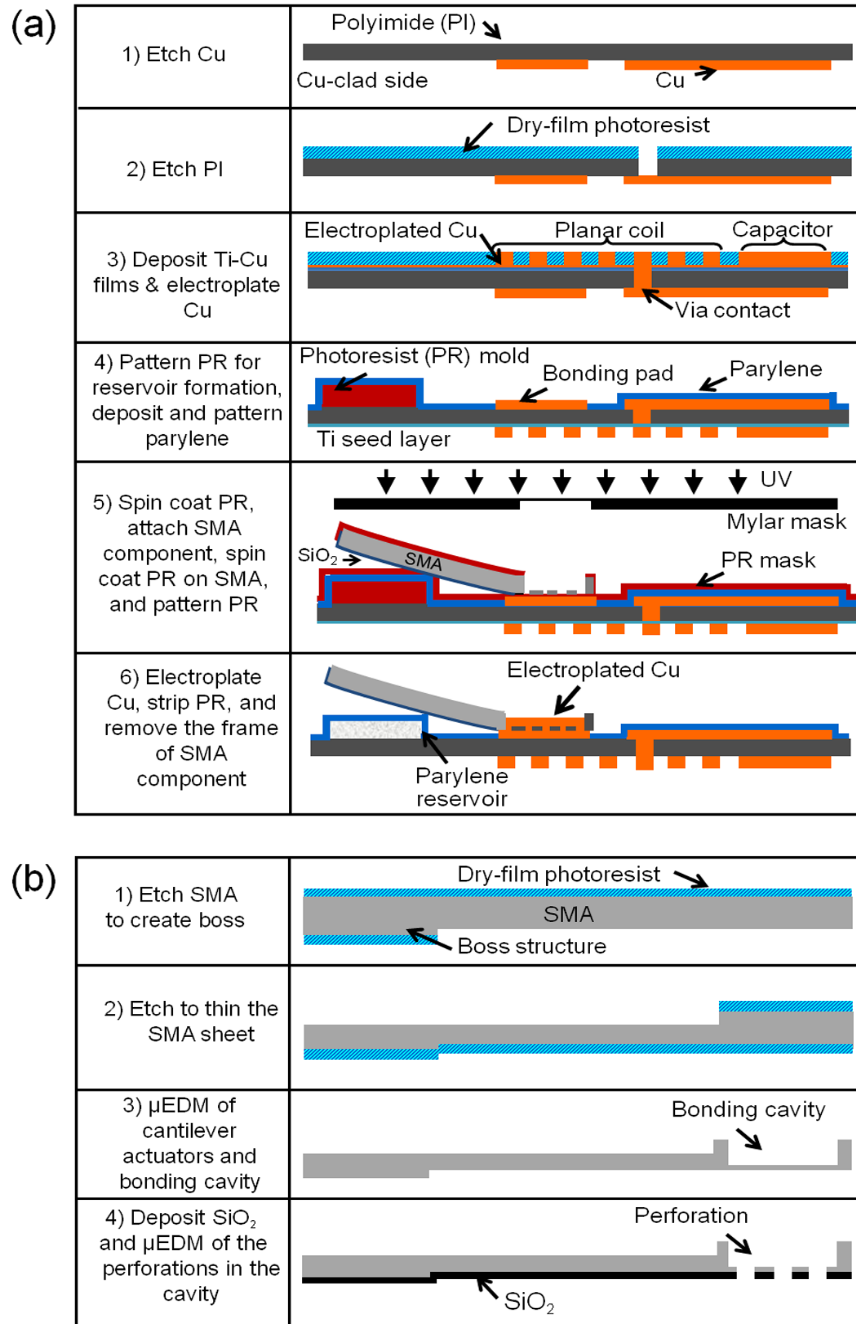


**Figure 4.3:** Cross sectional view of the fabrication process for (a) wireless resonant circuit (steps 1-3), reservoir formation (step 4), and SMA actuator assembly (steps 5-6), and (b) the SMA actuator component.

Next, the SMA plate is etched from the other side in HNA to thin the structure down to ~100 µm while protecting the opposite side of the SMA (Figure 4.3(b), step 2). The SMA plate is then patterned using µEDM to shape the cantilever structures as well as the cavity and the perforations noted earlier (Figure 4.3(b), step 3) using the same machining parameters described in Chapter 3. A sample of the patterned SMA plate is shown in Figure 4.4(b); the actuator array is still tethered to the frame structure at this stage, for not only easier handling, but also high-precision assembly and bonding of each of the actuators to the heater circuit. A 3.5-µm-thick $SiO_2$ film, the compressive reset layer, is deposited on the bottom surfaces of the SMA using PECVD at an approximate temperature of 390 °C (Figure 4.3(b), step 4).

The cavity regions of the SMA actuators fabricated above are fixed onto the bonding pads on the circuits coated with the SPR-220 photoresist that serves as a temporary adhesive for the SMA attachment (Figure 4.3(a), step 5). The photoresist is then soft baked for 10 minutes at 90 °C, followed by spin coating of another layer of the photoresist on top of the SMA and its soft baking. After the photoresist on the cavity regions is removed with a lithography step (Figure 4.3(a), step 5), Cu is electroplated in the regions to grow 120-µm-thick bonding structures through the perforations, fixing the actuator array onto the substrate (Figure 4.3 (a), step 6).

All the photoresist layers including the sacrificial mold inside the parylene reservoir are then dissolved using acetone in an ultrasonic bath. Lastly, the titanium seed layer is etched to complete the heater circuit fabrication, and the frame of the SMA actuators is removed by locally etching the tethers using µEDM (Figure 4.4(c)). Heaters-1, -2, and -3 of the fabricated device were typically measured to have a common inductance of 89 nH while having different capacitances of 3.3, 4.2, and 5.4 pF and $f_r$ of 231, 264, and 295 MHz, respectively, all of which match well with the theoretical values (Figure 4.2(a)).

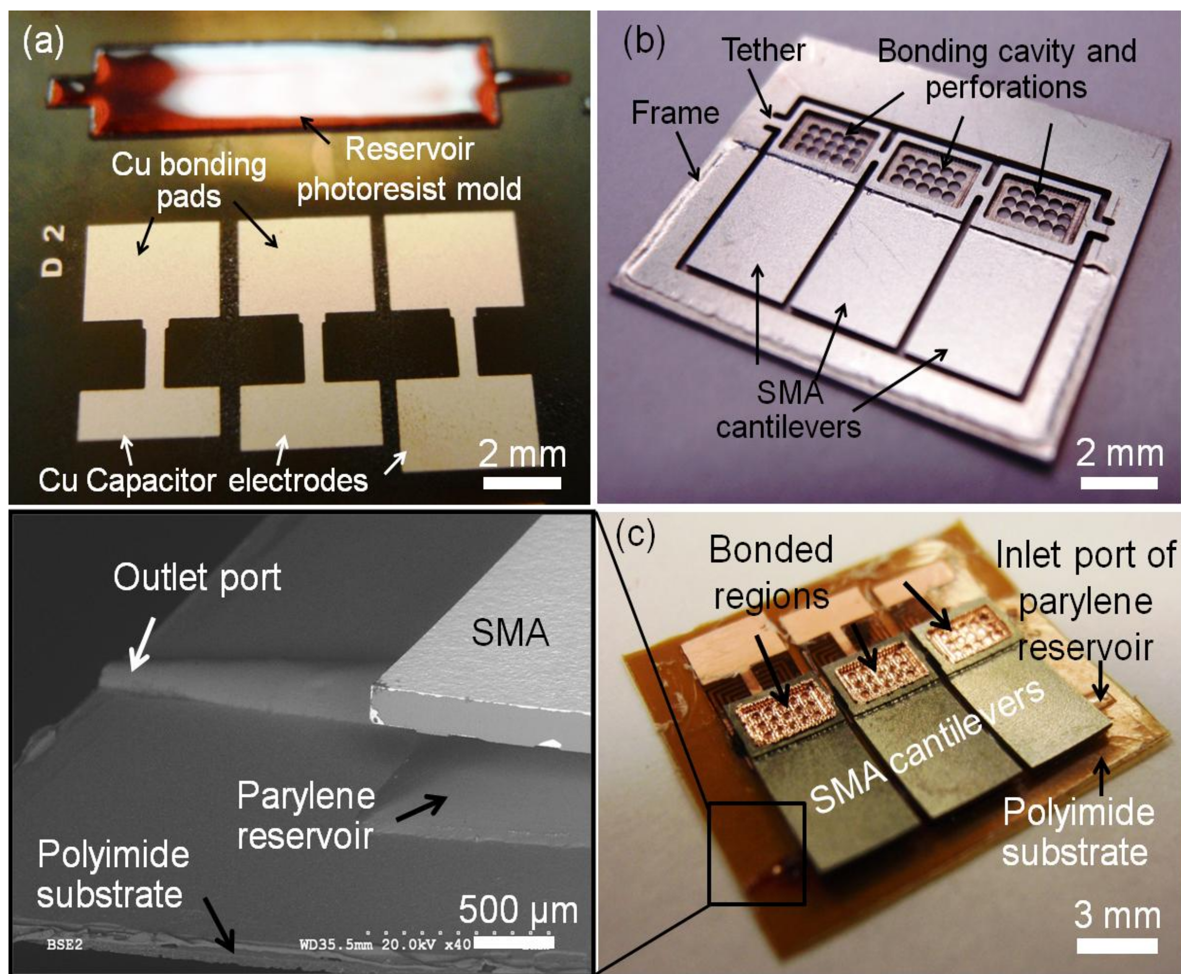


**Figure 4.4:** Fabrication results: (a) Sacrificial photoresist mold patterned for the reservoir, and Cu bonding pads for the SMA actuator assembly; (b) SMA component fabricated by wet etching and µEDM; (c) fabricated device with close-up of the parylene reservoir.

## 4.4 Experimental Results and Discussion

Characterization results for the fabricated actuators including the multiple wireless-heater operation using frequency-modulated RF magnetic fields as well as thermal behaviors of the actuators are discussed in this section. The stepwise pH-level modification through the wireless control of the fabricated microsyringe device is experimentally demonstrated.

### 4.4.1 Selectable Activation of Wireless Heater Array

The wireless activation of the LC resonant heaters fabricated in an array was first evaluated using the set-up shown in Figure 4.5 (without the beaker and the pH meter used for the experiment discussed in Section 4.4.3). An RF signal generator (HP 8657A) was interfaced with a Labview™ program to control the frequency modulation, and the amplified RF signals were fed to an external coil to generate RF magnetic fields.

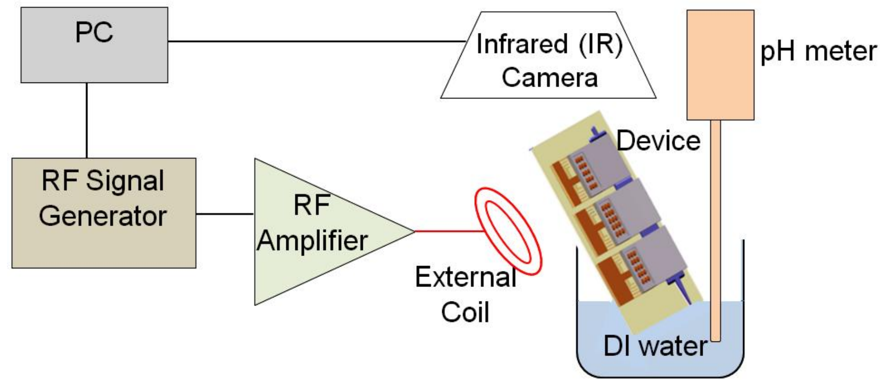


**Figure 4.5:** Experimental setup for wireless testing of the fabricated devices.

An array of four heater circuits (Figure 4.6(a)) was used for this test. These circuits have spiral coils with identical dimensions (3.8×7 mm$^2$), and the size of the capacitors were varied to differentiate their resonant frequencies with an approximate separation of 30 MHz as noted earlier. The $f_r$ of the heaters ($f_{r1\text{-}4}$) were wirelessly measured using the external coil connected to a spectrum analyzer (Agilent 4396B) by detecting the dips in the S11 parameter whose frequencies correspond to $f_r$ of the heaters (Figure 4.6(b)).

The size of the external coil (23-mm diameter, ~900 nH) was adjusted to cover the entire array of the heaters. The measurement shows that $f_{r1}$, $f_{r2}$, $f_{r3}$, and $f_{r4}$, are 136, 163, 188, and 211 MHz, respectively. In this test, the selective wireless activation of the heaters was

implemented by modulating $f_m$ to $f_{r2}$ and $f_{r4}$, i.e., activating only Heaters-2 and -4 at a 1-W RF output power. For the $f_m$ modulation, $f_m$ was switched alternately between $f_{r2}$ and $f_{r4}$ with a time period of 15 ms for each frequency.

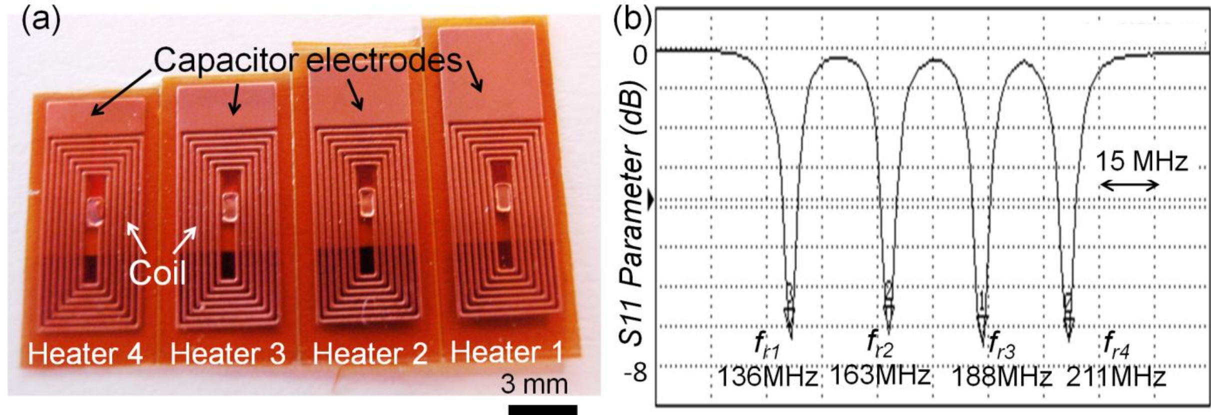


**Figure 4.6:** (a) Array of four wireless heaters; (b) Measured $f_r$ of the four heaters.

The heat distribution across the circuit array was measured using an infrared (IR) camera (Jenoptik VarioCam HiRes 1.2M, Jena, Germany) as illustrated in Figure 4.5. Figure 4.7(a) shows an IR image of the array captured at the 8th second after the heaters were activated. The temperature distribution along the line (A-A') indicated in Figure 4.7(a) is shown in Figure 4.7(b). The distribution along the same line before the activation is also plotted in Figure 4.7(b) for comparison. It can be seen that the temperatures of the coil regions in Heaters-2 and -4 were increased significantly, with a maximum temperature of ~75 °C on their coils, whereas the temperatures of the other heaters (Heaters-1 and -3) remain low. The average temperatures over the coil regions in Heaters-1, -2, -3, and -4 were measured to be 34.2, 66.3, 46.7, and 66.6 °C, respectively. This measurement clearly indicates that only the regions of the activated heaters reached the temperatures greater than the threshold temperature of the SMA (65 °C) thus the SMA coupled with them can be actuated, while the temperatures in the regions of the inactive heaters were low enough to keep the corresponding

SMA inactive. This result verifies the effectiveness of the $f_m$ modulation principle for the selective activation of the heater-SMA component. This result also shows that planar coils with unique $f_r$ act as frequency sensitive heaters and can be controlled by choosing appropriate $f_m$ as reported in Chapter 2.

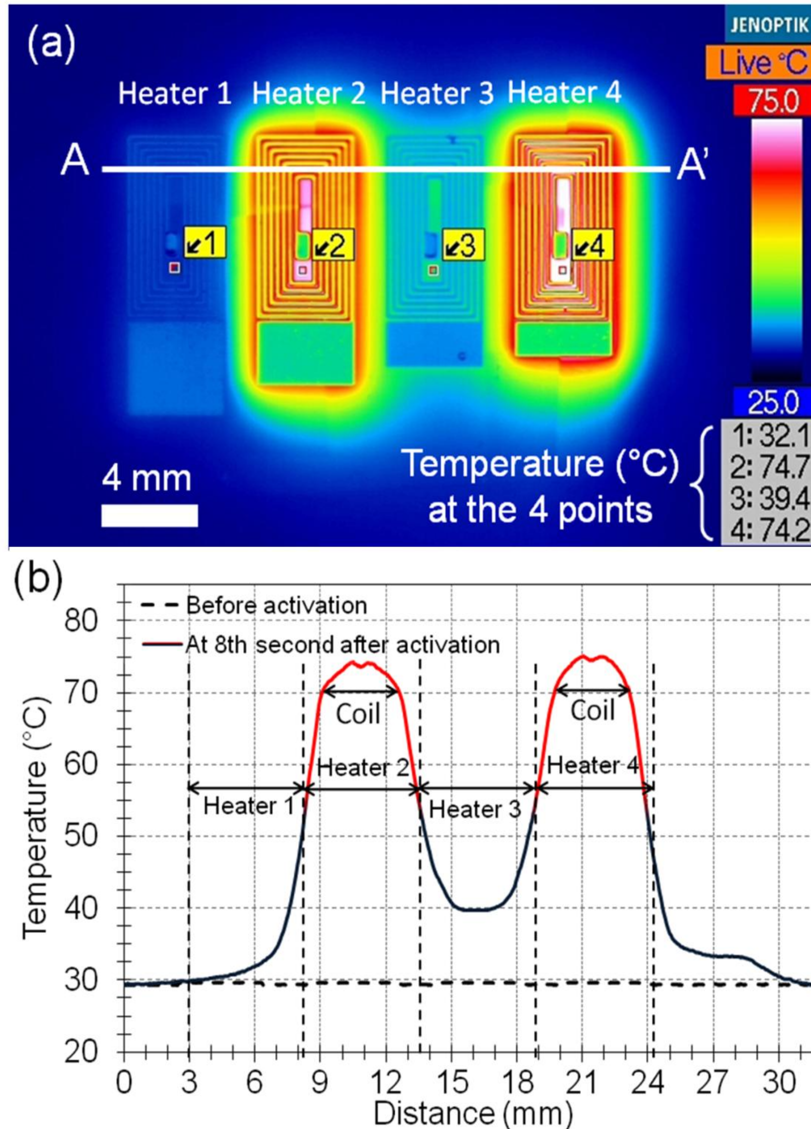


**Figure 4.7:** (a) IR image showing selective wireless activation of Heaters-2 and -4; the image was captures at the 8th second after the activation. (b) Temperature distribution accross the array of the four heaters along the line A-A' indicated in Figure 4.7(a).

### 4.4.2 Heat Distribution in the SMA Cantilever Actuator

The SMA cantilever structure is actuated by applying heat to one end of the structure. This leads to a thermal gradient across the structure due to heat loss, as well as a time delay in the heat transfer to the other end of the structure. These spatial and temporal characteristics in the heat transfer within the SMA structures are the important factors that affect their actuation behaviors. To characterize them, the temperature distribution and its change with time in an activated SMA cantilever were measured using the IR camera. The cantilever actuator bonded to Heater-2 in the device shown in Figure 4.4(c) was activated by tuning $f_m$ to the $f_{r2}$ value (264 MHz). The RF power used for this test was 0.15 W (approximately the minimum level required for the full-range actuation of the cantilever). Figure 4.8 shows an IR image of the cantilever at the 13th second after activation, the time when the temperature at the free end of the cantilever reached the SMA's threshold temperature of 65 °C and the actuator was fully activated.

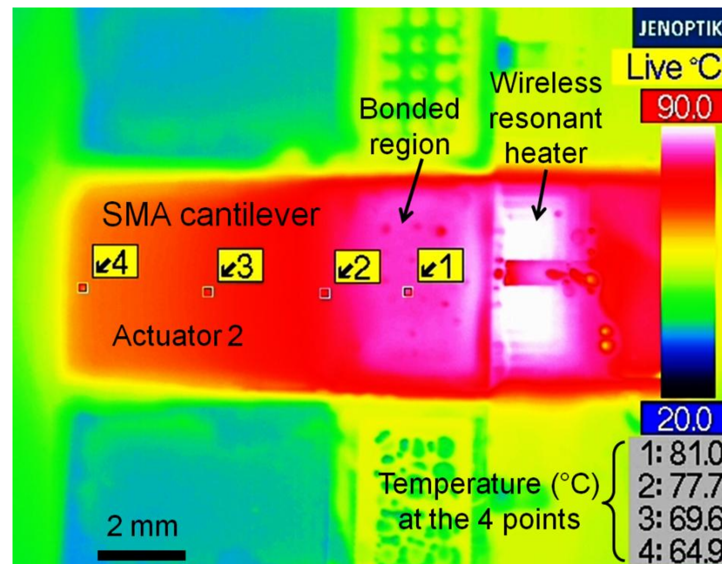


**Figure 4.8:** IR image of the SMA cantilever actuator with the wireless heater captured at the 13th second after the heater activation.

The temperatures indicated by the inset numbers 1, 2, 3 and 4 in Figure 4.8 correspond to those at the SMA bonding cavity covered by electroplated Cu, the fixed end of the cantilever, a middle location (2.5 mm away from the point 2) of the cantilever, and the free end (5 mm away from the point 2) of the cantilever, respectively. Transient temperatures measured at these four points for the time period of 13 seconds are plotted in Figure 4.9(a). The same measurement was repeated by doubling the RF power (to be 0.3 W, Figure 4.9(b)). The results in the average rate of temperature increase, full-actuation time, and temperature gradient between points 1 and 4 at the time of the full actuation for the two RF power levels are summarized in Table 4.1.

The temperature gradient across the SMA cantilever beam was continuously higher with higher power; this is clearly seen in Figure 4.9(c) that plots the temporal changes of the temperature gradient between points 1 and 4 shown in Figures 4.9(a) and 4.9(b). The temperature gradient at the full-actuation time with 0.3 W was measured to be twice the gradient for the case with 0.15 W (Table 4.1). This result indicates that, although increasing the RF output power improves the temporal response of the actuator, it leads to a higher temperature at the fixed end of the cantilever in order to achieve full actuation. Low operational temperatures are required in many cases, especially those in biomedical areas. To minimize heat produced and its dissipation to the external environment, the RF power level should be optimized in conjunction with the selection of SMA materials that have lower threshold temperatures as well as with proper device packaging.

**Table 4.1:** Measured actuator response at 0.15 and 0.3 W power levels.

| RF Power | Average rate of temperature increase (°C/s) | Time for full actuation (s) | Temperature gradient between points 1 and 4 (°C) |
|---|---|---|---|
| 0.15 W | 4.1 | 13 | 16 |
| 0.3 W | 8.6 | 8 | 32 |

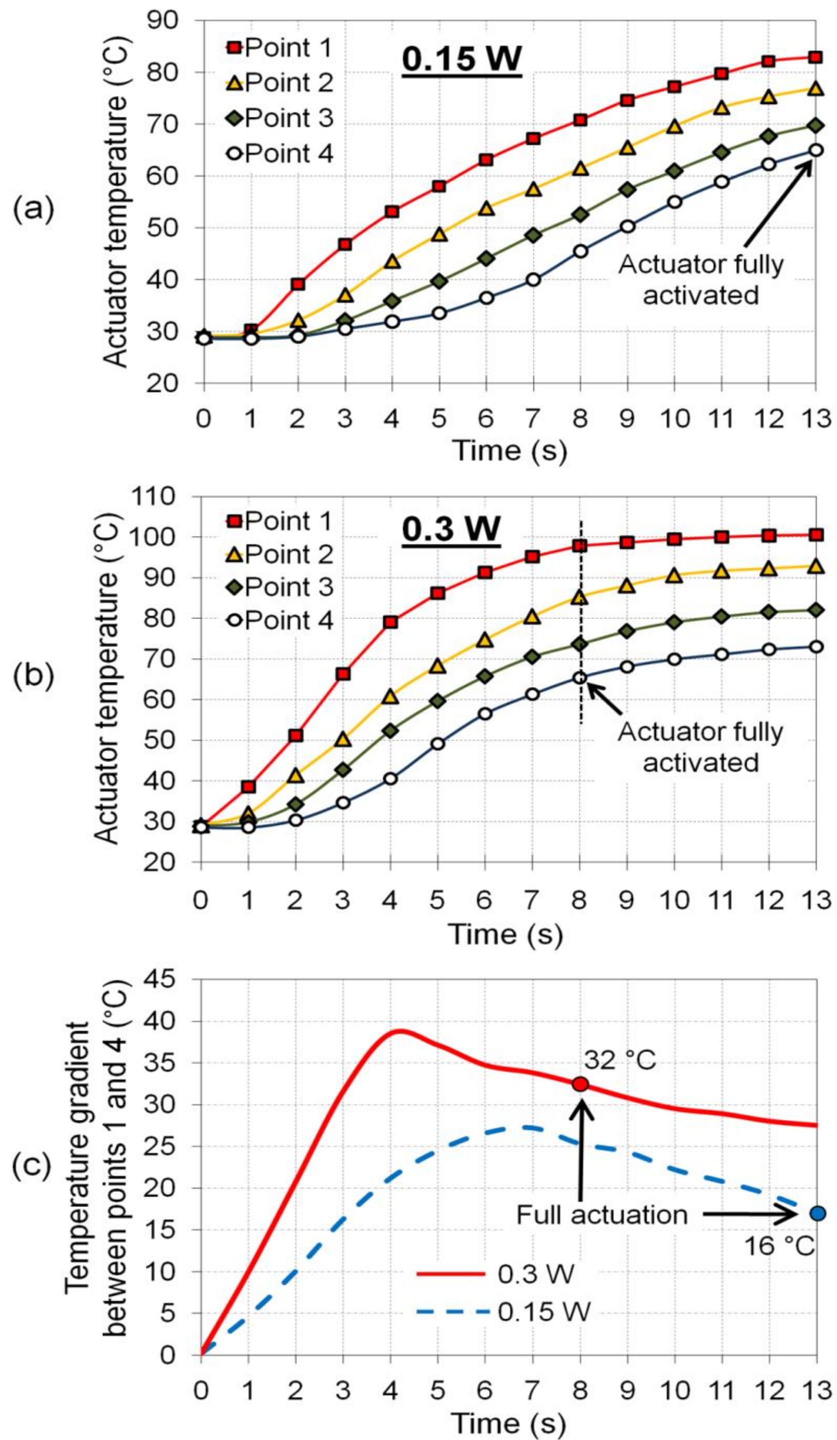


**Figure 4.9:** Measured temporal changes in the temperature of the SMA cantilever actuator at the four points (Figure 4.8) when the heater is wirelessly resonated with RF output power of (a) 0.15 W and (b) 0.3 W. (c) Temporal changes in temperature gradients between the bonding cavity (point 1) and the free end of the cantilever (point 4) for the 0.3-W and 0.15-W cases obtained from the results in Figures 4.9(a) and 4.9(b).

### 4.4.3 Wireless Test for the Microsyringe Device

Preliminary wireless tests for the fabricated microsyringe devices were experimentally performed using the set-up illustrated in Figure 4.5. The external coil was placed at a distance of ~8 mm from the device in this experiment. The wireless activation of individual actuators through $f_m$ tuning was first tested – Figures 4.10(a) and 4.10(b) show side views of Actuator-3 (Figure 4.2(a)) in the inactive state without an external field and in the fully active state established with an field at $f_m$ = $f_{r3}$, respectively, showing that the activated SMA actuator squeezes the parylene reservoir underneath in Figure 4.10(b). The maximum force at the free end of the actuator was measured to be ~840 mN using a digital force gauge (DS2-1, Imada Inc., IL, USA) with a 1-mN resolution. Device tests were further conducted to demonstrate the wireless control of the pH level of liquid. This was implemented by ejecting controlled amounts of a pH buffer from the device's reservoir to deionized (DI) water using the three actuators.

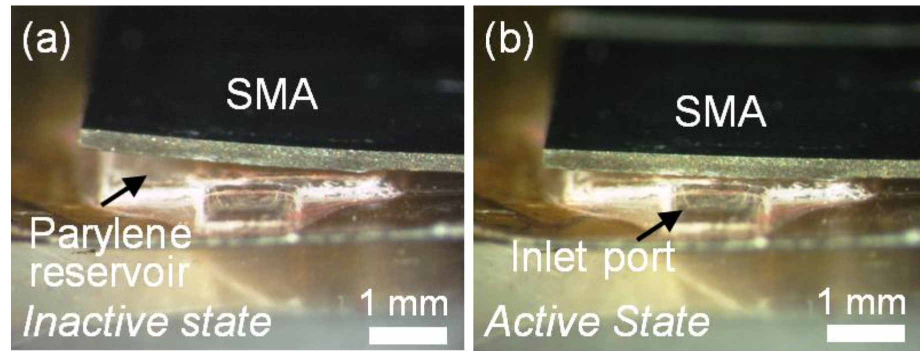


**Figure 4.10:** Side views of the SMA cantilever actuator in (a) the inactive state and (b) the active state showing the SMA squeezing the reservoir.

A device that was measured to have $f_{r1}$, $f_{r2}$, $f_{r3}$ of 231, 264, and 295 MHz, respectively, was used for this experiment. The reservoir was fully filled with ~5 μl of pH-2 buffer solution (SB96-500, Fisher Scientific, ON, Canada) through the inlet port using a syringe

needle, and then the port was sealed with silicone adhesive. The device was placed in a beaker with 10 ml of DI water so that the outlet port of the reservoir was immersed in the water, and its pH value during the test was measured using a pH meter as shown in Figure 4.5.

The stepwise ejections of the buffer solution from the reservoir were implemented through the following three steps with a 1-minute interval (each step took ~1 minute): 1) only Actutor-3 was activated by tuning $f_m$ to the $f_{r3}$ value, squeezing a 1/3 area of the reservoir; 2) Actuators-3 and -2 were simultaneously activated by modulating $f_m$ to the $f_{r3}$ and $f_{r2}$ values alternately for an equal time period of 15 ms, squeezing another 1/3 area of the reservoir; 3) Actuators-3, -2, and -1 were all activated by modulating $f_m$ to the three $f_r$ values in the same manner, squeezing the last 1/3 area of the reservoir. In Step-1, an RF output power of 0.25 W was sufficient for full squeezing with Actuator 3. When two or more actuators are involved, as in Steps-2 and -3, the duty cycle of actuator excitation drops from 100% to 50% or less, causing heat loss during each “off” time in the cycle. The actuator temperature decreases more as the number of actuators increases, i.e., the off time in each actuator becomes longer. In order to compensate for this condition, the RF power in Steps-2 and -3 was adjusted to higher levels (1.2 and 3.2 W, respectively) to ensure full squeezing. Comparing between the power levels in Step-1 and Step-2, it can be seen that a substantially larger power (4.8×) was needed in Step-2 due to the presence the off time in that case. The required power in Step-3 was 2.67× larger than that in Step-2, although the off time in Step-3 was only twice the off time in Step-2. This difference may be related to various potential causes, including non-uniform power transfer to the heaters/actuators due to their different locations with respect to the external coil, as well as a slight delay in frequency settling observed when the RF signal generator used switches the frequency (affecting the duty cycle).

An extended study will follow for further investigation of these aspects in power requirement related to actuator multiplicity. The measured pH value and the amount of released solution calculated from the measured pH after each of the three actuation steps are shown in Figure 4.11. The pH measurement indicates a consistent reduction from the initial pH value of 6.90 to the final value of 5.43 due to the release of the acidic buffer solution.

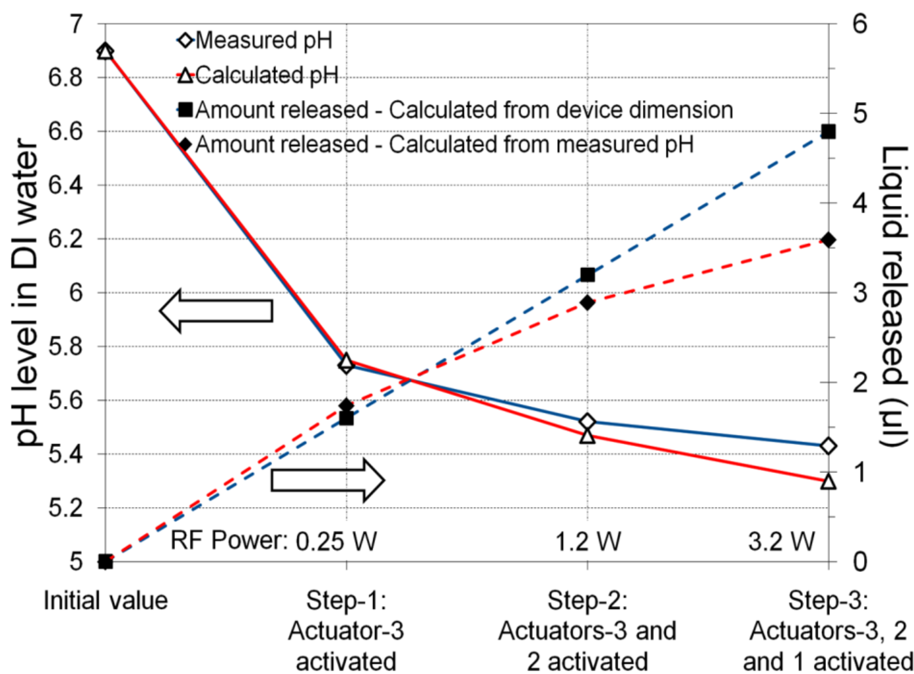


**Figure 4.11:** pH changes and released amounts of pH buffer (measured and calculated) vs. actuators activated.

A theoretical volume of the released solution (calculated with the reservoir and actuator sizes, i.e., release volume of $4.1 \times 3 \times 0.13$ mm$^3$ per step) and a pH value calculated from the theoretical released volume after each step are also plotted in Figure 4.11. The dissolution of atmospheric $CO_2$ in DI water is known to affect its pH value [175] – it was verified that this effect was negligible for the time period involved in the experiment. As can be seen, both measured pH values and the released amounts calculated using the pH values show good

agreement with the corresponding theoretical values defined above. Small deviations seen in Steps-2 and -3 may be related to the incompleteness in the reservoir squeezing, which can be caused by various non-ideal factors such as variations in the height of the bonded actuators and slight bending of the PI substrate.

## 4.5 Conclusion

The fully passive, selectable wireless actuation of multiple bulk-micromachined SMA actuators using frequency-modulated RF magnetic fields has been demonstrated. The SMA actuators were coupled with planar wireless resonant heaters that have unique resonant frequencies, and thus they could be activated selectively using the external field whose frequency was modulated to the heaters' resonant frequencies. The electroplating-based planar bonding technique developed in this research was used to integrate an array of the SMA actuators with the planar heaters, achieving mechanical and thermal coupling between the actuators and the heater circuits. A microsyringe device was designed and fabricated as a proof-of-concept demonstration of the wireless multiple-actuator control toward a variety of microfluidic and biomedical applications. The thermal behavior and its temporal response of the SMA actuators were experimentally characterized at different RF-power levels. The wireless operation of the fabricated devices was successfully implemented to show controlled releases of liquid from the device's reservoir through selective activations of three SMA actuators integrated in the device. Stepwise ejections of acidic solution from the reservoir were wirelessly performed to demonstrate sequential pH modification, showing results that matched well with theoretical values. Future work will involve the optimization of the device design and fabrication as well as further integration and miniaturization of the actuator module.

# Chapter 5

# Radio-Controlled Out-of-Plane Microactuators using Shape-Memory Alloy Spiral-Coil Inductor

## 5.1 Introduction

Passive wireless control of SMA wireless actuators using RF magnetic field were reported Chapter 3 and Chapter 4 [166, 167, 173, 174]. In these cases, the receiver coils, which act as a frequency sensitive wireless heater, and the bulk-micromachined SMA component, are formed as two separate parts. Then, one end of the SMA part is coupled with the coil through the developed electroplated bonding method. The heat will be generated at the coil when it is exposed to the RF magnetic field that matches with the coil's $f_r$ and then transferred to the SMA part through the bonded structure for the actuation. This causes a high thermal gradient between the heater and the SMA part. In addition, the response of the actuator is rather slow due to the time delay for the heat to be transferred to the SMA. The low thermal conductivity of the Nitinol type SMA that used for fabricating the actuator further deteriorates the actuator's temporal response during the heating process.

This chapter[3] reports an innovative method to fabricate an out-of-plane actuator using bulk-micromachined SMA coils, and the passive wireless actuation of the microcoils using RF magnetic field. The out-of-plane coil is formed using a planar fabrication method with a patterned stressed film. The SMA coil acts as both the resonant circuit, which receives power

[3] A version of this chapter is submitted to *Journal of Microelectromechanical System* as "M.S. Mohamed Ali, B. Bycraft, A. Bsoul and K. Takahata, 'Radio-Controlled Out-of-Plane Microactuators using Shape-Memory Alloy Spiral-Coil Inductor'".

wirelessly, and the actuator. This approach reduces the fabrication complexity and the overall size of the actuator. Another important feature is that the SMA is used as the substrate/base material, eliminating the need for the special processes needed to integrate bulk SMA. The direct wireless heating of the SMA coil improves temporal response and reduces the temperature gradient of the actuator which broadens its potential applications. Based on the changes in the inductance value which modifies $f_r$ of the actuator during actuation, a wireless displacement monitoring method is presented by tracking the changes in $f_r$ that corresponds to a specific degree of displacement. The temporal and thermal responses, as well as the force generated by the actuators are experimentally characterized and reported.

## 5.2 Working Principle of the Device

The formation of an out-of-plane SMA actuator is achieved by creating selected patterns of a reset layer directly on a planar spiral-coil structure of SMA. This configuration, with proper patterns, leads to locally controlled bimorph deformations in the coil, resulting in a vertical displacement of the planar coil. This technique was also applied to the development of out-of-plane spiral-coil copper inductor, which is discusses in Appendix A [176]. As the SMA coil is used as an inductor to form an LC tank circuit with a fixed capacitor, an AC electromotive force is generated in the circuit when it is exposed to a RF magnetic field. When $f_m$ matches $f_r$ of the LC tank an AC current flows through the SMA coil and itself produces Joule heat. The SMA coil returns to its flat remembered shape when the coil's temperature reaches the austenitic phase temperature of the SMA (Figure 5.1(a)).

In this approach, the LC resonant tank is used as a heat source that can be activated by $f_m$ tuning to enable wireless control of thermal actuators (SMA in this case); details of the working principle of this type of wireless resonant heater is described in Chapter 2. In the

present device, the SMA is designed to serve as the actuator as well as the heat source, thus RF power transfer to the actuation is expected to be much more effective than the cases in Chapter 3 and Chapter 4 that use separate heat sources.

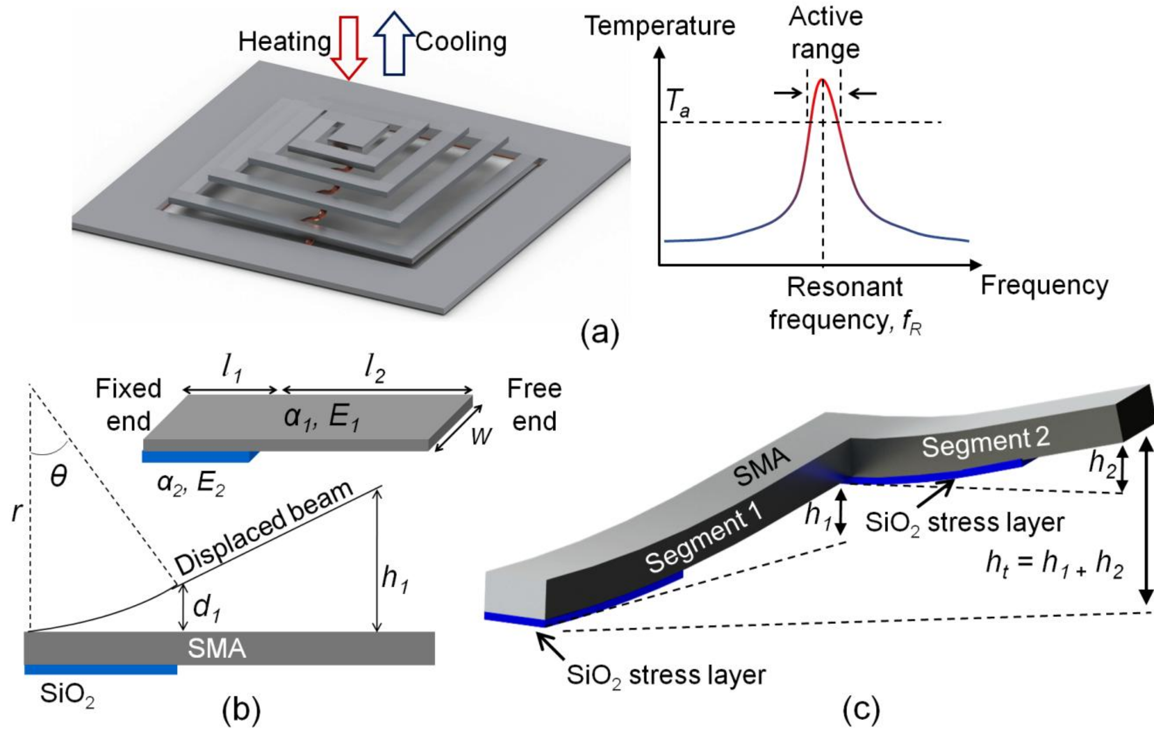


**Figure 5.1:** (a) Conceptual diagram and working principle of the 3D SMA spiral-coil actuator; (b) bimorph actuation of a single segment of the coil; and (c) additive height gain from two consecutive segments of the coil.

In order to form an out-of-plane displacement, the spiral coil is designed to have patterned reset layer on each coil segment (Figure 5.1(a) and (c)). At the cold state, the difference of the CTE between the reset layer (2-μm·m$^{-1}$·°C$^{-1}$ for $SiO_2$ used in this study) and the SMA (6 to 11-μm·m$^{-1}$·°C$^{-1}$ depending on the temperature) that forms the coil causes a compressive stress in the reset layer defined on the coil, causing a height change in each of the segments of the SMA coil due to bending in the bimorph regions (Figure 5.1(b)). The vertical

displacement is also defined by the length of the reset-layer patterns since the displacement forms the arc whose radius of curvature, $r$, illustrated in Figure 5.1(b), can be expressed as:

$$\frac{1}{r} = \frac{6w_1w_2E_1E_2t_1t_2(t_1+t_2)(\alpha_1-\alpha_2)\Delta T}{(w_1E_1t_1^2)^2+(w_2E_2t_2^2)^2+2w_1w_2E_1E_2t_1t_2(2t_1^2+3t_1t_2+2t_2^2)} \tag{5.1}$$

where $E$ is the Young's modulus of the materials, $w$ is the width of the beam, $t$ is the thickness of the layer, $\alpha$ is CTE, $\Delta T$ is the temperature difference between initial flat condition and deformed state, and subscript *1* and *2* represents the SMA and the reset layer, respectively. The bent bi-layer section creates an angle between the displaced beam (end of the reset layer) and the fixed end represented by $\theta = l_1/r$, where $l_1$ is the length of the reset layer. The vertical displacements at the end of the reset layer, $d_1$, and at the free end of the beam, $h_1$, are then expressed as $r(1 - \cos\theta)$ and $d_1 + l_2\sin\theta$, respectively, where $l_2$ is the length of the SMA beam portion without the reset layer.

Figure 5.1(c) displays two consecutive segments with different lengths as part of the SMA coil, showing the total vertical displacement, $h_t$, representing the sum of the individual displacements for the two segment, $h_1 + h_2$. In order to achieve a uniform rise of the coil, the length of the reset layer was varied to provide different levels of bending in each segment of the coil as shown in Figure 5.2(a). These lengths of the reset layer of $SiO_2$ were determined through FEA performed using COMSOL Multiphysics 3.5a. The FEA result shown in Figure 5.2(c) indicates that 3.5-μm-thick $SiO_2$ layer with the layout shown in Figure 5.2(a) deposited at 420 °C on a 35-μm thick SMA coil provides a total out-of-plane displacement of 492 μm at the cold state. Raising SMA's temperature to austenite phase, by resonating the coil using an RF excitation as noted earlier, triggers the actuation of the 3D coil, which returns to the

memorized planar geometry and remains flat as long as the temperature is kept in austenite region. The removal of the resonance (by either shifting $f_m$ off from $f_r$ or turning off the field) cools the device down to the martensite phase, and the flat SMA coil restores the original 3D shape because of the force provided by the $SiO_2$ reset layer.

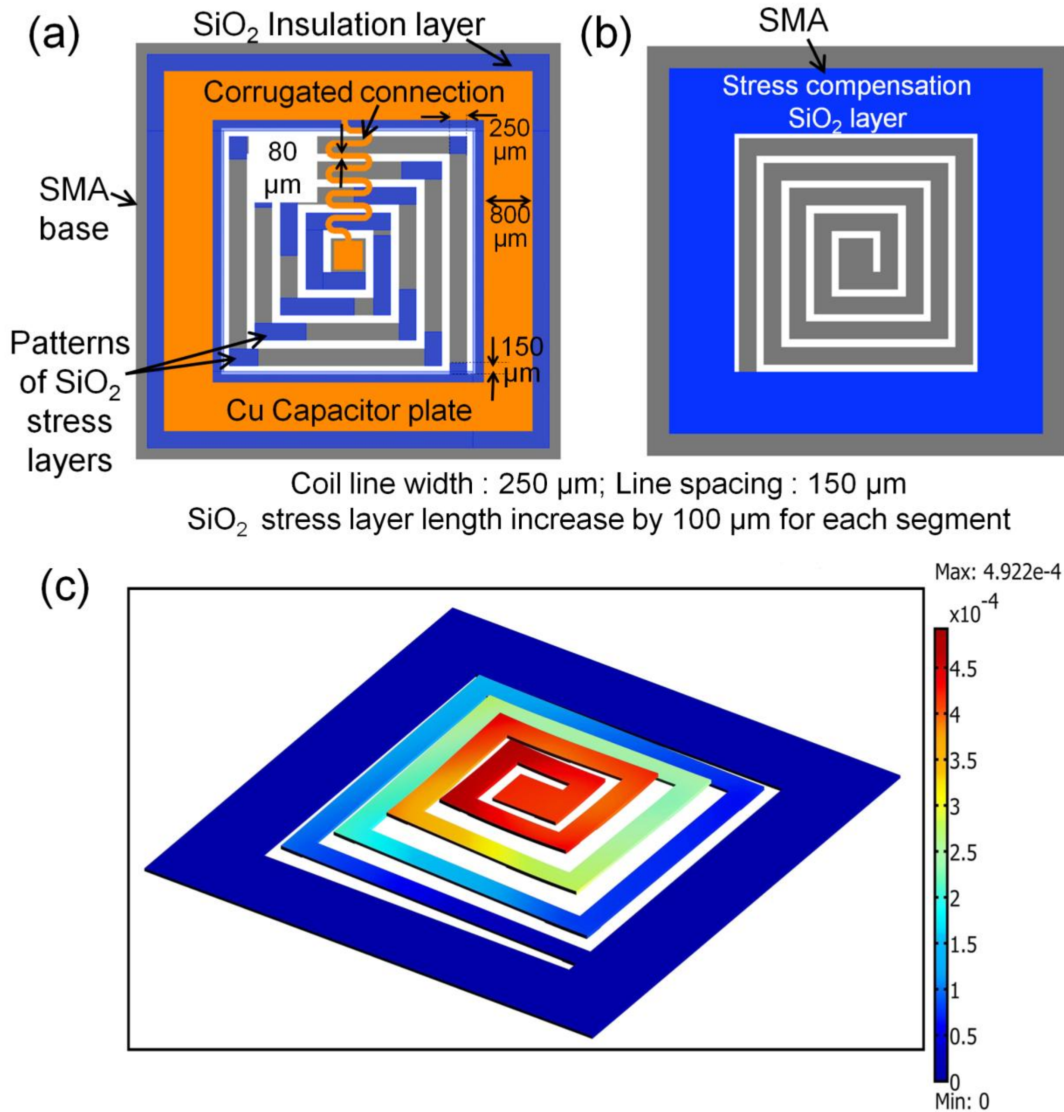


**Figure 5.2:** (a) Design of the SMA actuator showing the backside; (b) design of the SMA actuator showing the front side; (c) a FEA result showing an out-of-plane displacement of 492 µm at room temperature, obtained with a model that defines a 3.5-µm-thick $SiO_2$ layer deposited at 420 °C and patterned.

As shown in Figure 5.2(a), the outer region of the SMA coil is used as the substrate to form a built-in fixed capacitor on the backside, in which the SMA substrate itself serves as one of the parallel-plate electrodes, i.e., electrical coupling between the outer end of the SMA coil and the capacitor is directly made through the substrate. The other capacitive electrode is created by depositing a Cu layer on an intermediate dielectric layer both of which are patterned on the SMA substrate to complete the capacitor element. The other electrical connection between the inner end of the coil and the capacitor is made by the Cu lead that is patterned together with the Cu electrode. This Cu lead is corrugated as shown in Figure 5.2(a) to minimize the stress applied to the lead during the out-of-plane actuation of the device. Figure 5.2(b) illustrates the top view of the device, where the SMA's outer substrate region is covered with a $SiO_2$ layer to compensate the stress induced by the dielectric layer of the capacitor on the opposite side of the region.

## 5.3 Device Fabrication

The fabrication process of the 3D SMA coil actuator is illustrated in Figure 5.3. A 200-μm thick SMA plate is first etched down to a thickness of 35 μm using HNA solution as described earlier in Chapter 4. The SMA plate is then patterned using *μ*EDM to form the coil with the dimensions shown in Figure 5.2(a) (Figure 5.3(a)). The machining was performed at voltage level, capacitance, and tool rotation speed of 80 V, 3.3 nF, and 3000 rpm, respectively. The EDMed SMA piece is shown in Figure 5.4(a). The SMA sample is cleaned/degreased, and then 3.5-μm-thick $SiO_2$ is deposited on both sides of the SMA using PECVD at 420 °C (Figure 5.3(b)).

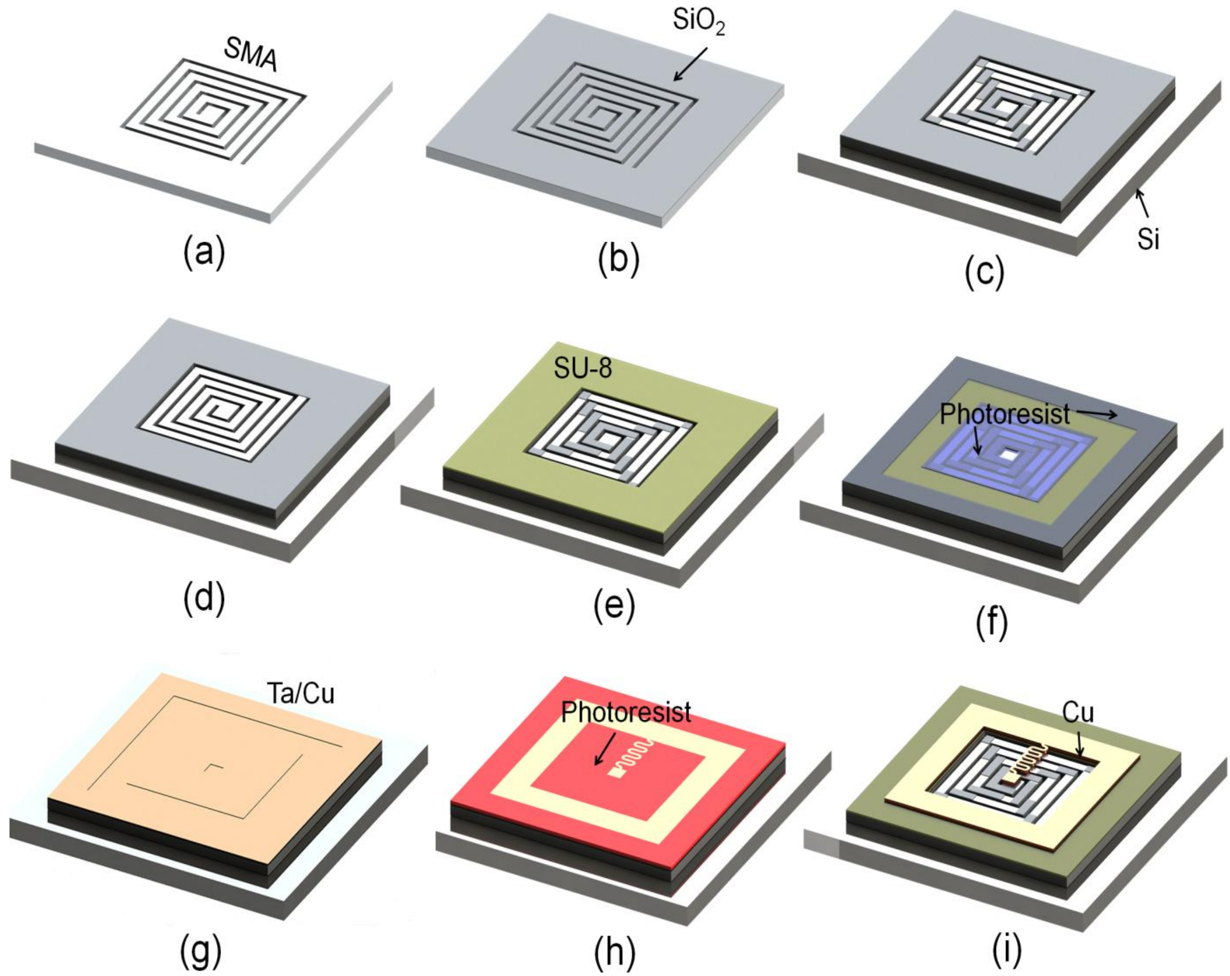


**Figure 5.3:** Fabrication process; (a) coil formation in SMA sheet using $\mu$EDM; (b) $SiO_2$ layer deposition on both sides; (c) bottom $SiO_2$ layer patterning; (d) top $SiO_2$ layer patterning; (e) SU-8 coating and patterning; (f) sacrificial photoresist patterning; (g) Ta/Cu seed layer deposition; (h) photoresist mold patterning; and (i) Cu electroplating and seed layer and photoresist removal.

For ease of handling and processing, the SMA sample is attached to a piece of a Si wafer using a polymer adhesive (Cristalbond 509, Electron Microscopy Science, PA, USA) at 100 °C. This fixation is conducted so that the backside of the SMA (Figure 5.2(a)) faces upward. Subsequently, a photoresist layer (SPR 220-7, Rohm and Hass Co., PA, USA) is spin coated on the sample and patterned for the $SiO_2$ reset layer formation. The sample is

then hard baked at 70 °C for 2 hours; this is necessary to minimize the diffusion of the $SiO_2$ etchant (buffered HF) into the photoresist during the etching process (Figure 5.3(c)). The SMA sample is then is removed from the Si piece using acetone. At this stage, the coil is bent and vertically displaced as shown in Figure 5.4(b).

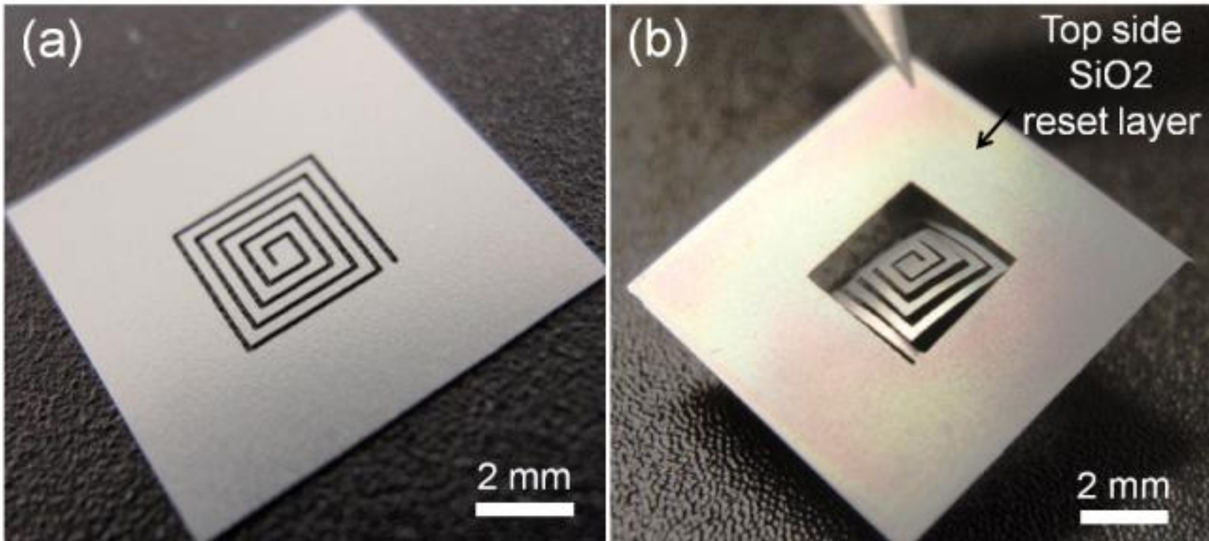


**Figure 5.4:** (a) EDMed SMA spiral coil and (b) SMA coil after backside $SiO_2$ reset layer have been patterned (before top side $SiO_2$ layer patterned).

The coil is then re-fixed on the piece so that the front side of the sample faces up. During the polymer bonding process which requires baking at 100 °C, the coil returns to austenite flat condition and sticks to the Si substrate. Next, another photoresist layer is spin coated on the sample, patterned and hard baked to form the stress compensation layer on the SMA base by wet etching of the $SiO_2$ layer (Figure 5.3(d)). The sample is then removed from the Si piece, which leads to a vertical displacement (measured to be 470 μm) in the SMA coil (Figures 5.5(a) and (b)). Next, the 3D SMA is deposited with a 400-nm-thick $SiO_2$ layer using PECVD on both sides of the sample for insulation purposes.

This $SiO_2$ layer also will serve as the dielectric layer of the fixed capacitor. The $SiO_2$ layer on the backside of the center of the coil is then removed using $\mu$EDM (this step is necessary to achieve the electrical connection to the corrugated lead to be formed later). The SMA piece is again fixed onto a Si piece using the adhesive so that the backside faces up (SMA returns to flat condition during baking process as mentioned earlier).

A SU-8 layer (2007, MicroChem, MA, USA) is spin coated on the sample and patterned to cover the outer substrate/base of the SMA, which is effective to fill any potential pinhole present in PECVD $SiO_2$ layer and avoid a short circuit between the capacitor electrodes. To ensure a good adhesion of SU-8 onto the $SiO_2$ surfaces, an adhesion promoter (AP 3000, Advance Electronic Material, CA, USA) is coated prior to the SU-8 coating (Figure 5.3(e)). Then, a thick sacrificial layer of SPR 220-7 is coated (to create a gap between the coil and the corrugated lead) and patterned to expose the SU-8 layer (for capacitor plate formation) and the center of the SMA coil.

After hard baking the sample at 70 °C for 8 hours, a Ta/Cu seed layer is sputtered on the sample (Figure 5.3(g)). Prior to this Ta/Cu deposition, an $O_2$ plasma treatment is performed to enhance the adhesion on the SU-8 surfaces. Next, a thin layer of the photoresist is patterned (Figure 5.3(h)) to be used as the mold for Cu electroplating of the capacitor electrode and the corrugated lead for a thickness of ~7 μm. Lastly, the layers of the photoresist and the Cu/Cr seed are all removed to complete the device fabrication (Figure 5.3(i)). Figures 5.5(c) and 5(d) show the device before and after being released from the Si base, respectively. The out-of-plane displacement of this particular device was measured to be 466 μm. The small decrease in the displacement from 470 μm noted above could be related to the force from the thin Cu corrugated connection to the capacitor plate.

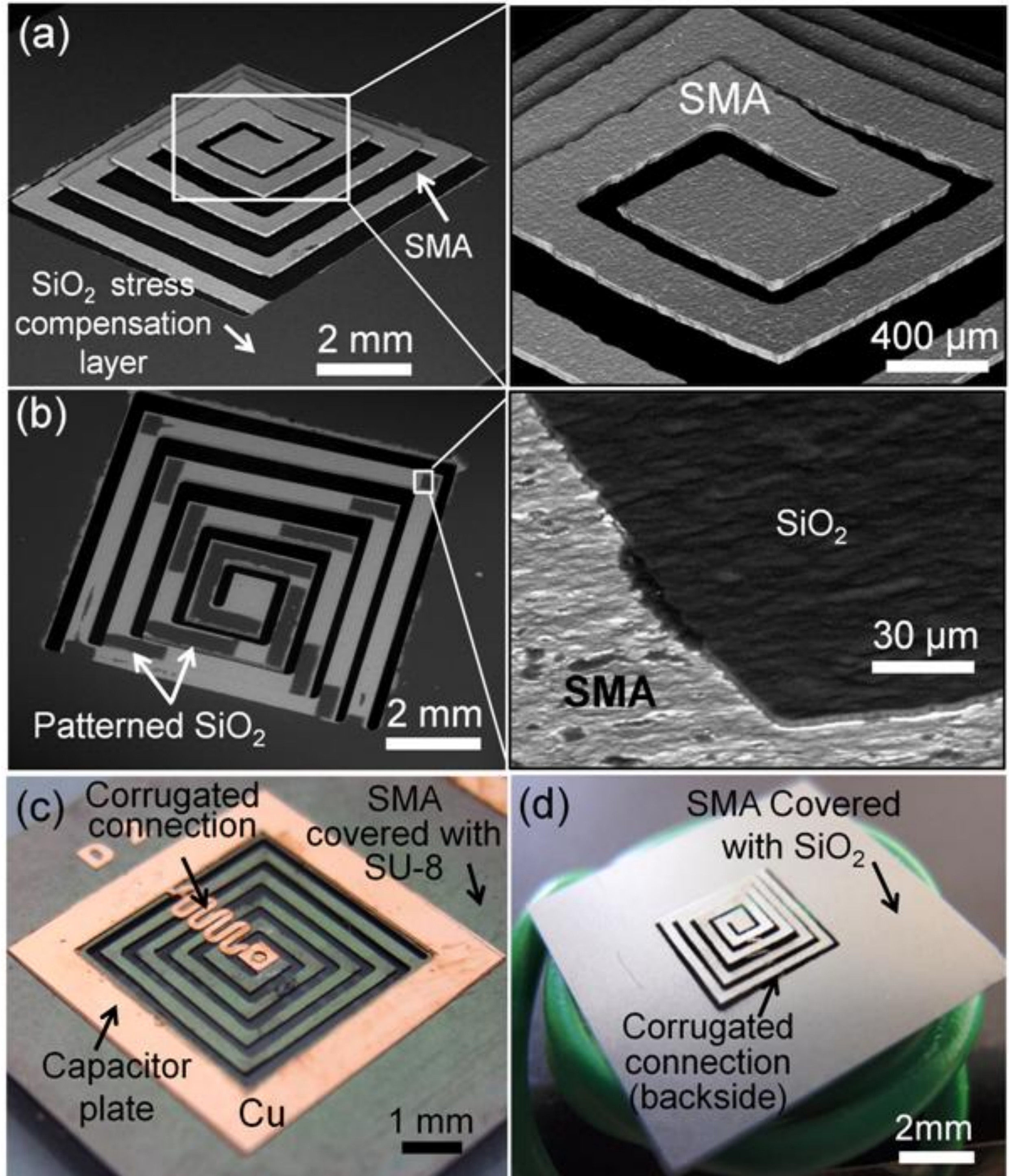


**Figure 5.5:** Fabrication results; (a) SEM image of the 3D SMA coil and a close-up view of the center of the coil; (b) SEM image of the $SiO_2$ reset layer patterned on the backside of the coil with a close-up view; (c) optical image of the backside of the device in its planar state prior to releasing from the base; (d) optical image of the front side of the released SMA actuator showing its 3D shape.

## 5.4 Experimental Results and Discussion

Characterization results for the fabricated SMA actuator are presented in this section. The performance of the device in terms of the thermal and temporal responses and their dependences on $f_m$ are experimentally evaluated through wireless actuation tests. In addition, the forces generated by the actuators and the wireless displacement monitoring are also assessed and discussed.

### 5.4.1 Characteristics of SMA Spiral-Coil Inductor

The frequency characteristics of the SMA inductor were first evaluated using a spectrum-impedance analyzer to which the inductor was connected through a wire interface. The inductance and the Q-factor of the SMA coil were measured in both the planar state (Figure 5.4(a)) and the 3D state (with an out-of-plane displacement of 470 μm, Figure 5.5(a)) (Figure 5.6).

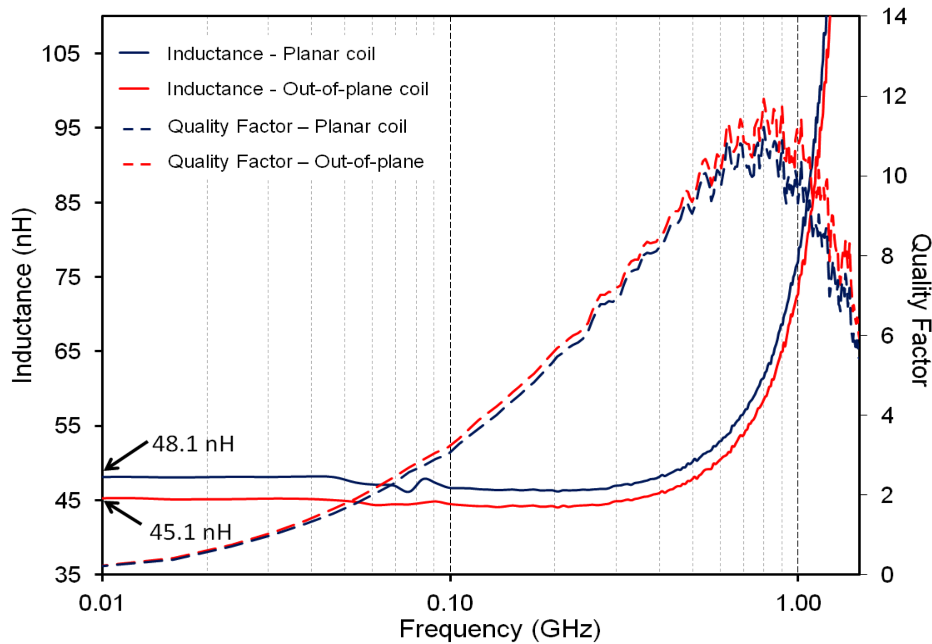


**Figure 5.6:** Inductance and Q-factor of the fabricated SMA spiral coil measured for its planar and 3D states as a function of frequency.

The inductances at a low frequency (10 MHz) for the planar and 3D SMA coils were measured to be ~48 nH and ~45 nH, respectively. This suggests an approximately 6.3 % reduction in the inductance induced by the out-of-plane displacement in the coil. This reduction is caused by the increase in the distance between turns which reduces the mutual inductance of the coil. The self resonances of the inductor in both the planar and 3D states were observed at ~1.5 GHz. The Q-factor was measured to be ~11 (peaked at ~0.8 GHz) with no significant difference between the planar and 3D states.

### 5.4.2 Wireless Tests of the SMA Actuator

**A. Measurement set-up**

Wireless measurements and operations of the fabricated devices were performed using the experimental set-up illustrated in Figure 5.7. In this set-up, an amplified RF signal with an output power of up to 0.7 W was fed to an external excitation coil (diameter ~6 mm, 497-nH, positioned ~1 mm below the actuator) to generate RF magnetic fields that were used for the wireless control of the actuator. As shown in Figure 5.7, Thermal responses of the actuator were characterized using IR camera, and the out-of-plane displacement of the actuator was measured at the center of the SMA coil using a CCD laser displacement sensor (LK-G32, Keyence, ON, Canada) whose laser spot size was 30 μm. The resonance of the SMA actuator was wirelessly observed using another external coil (7-mm diameter, ~380 nH, positioned ~2 mm above the actuator) connected to the Agilent network analyzer by detecting the dip in the S11 parameter whose frequency corresponds to $f_r$ of the actuator (this external coil for resonance detection is not shown in Figure 5.7).

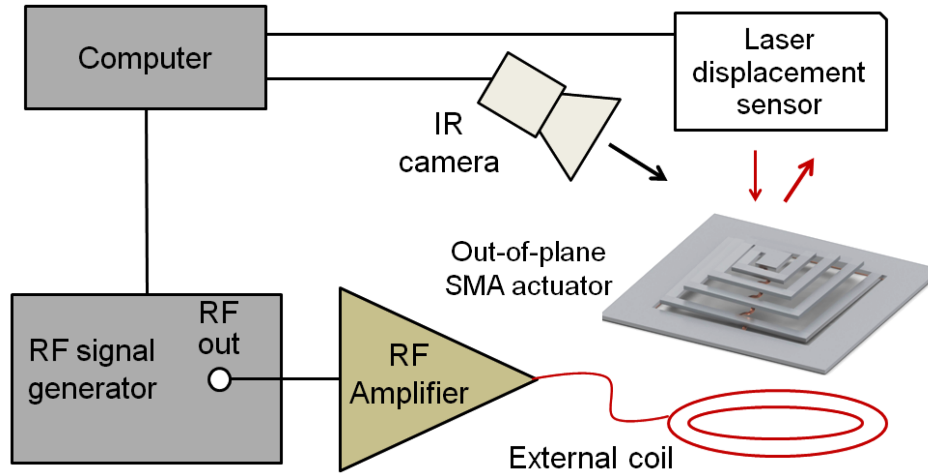


**Figure 5.7:** Experimental set-up used for wireless actuation tests**.**

**B. Frequency response: Temperature and displacement**

The device at its cold (3D) state was measured to have a typical $f_r$ of 238 MHz using the set-up described above. This measured $f_r$ matches well with a theoretical value calculated using measured inductance and capacitor of the device (45 nH and 10 pF, respectively, providing $f_r$ = 237 MHz). With this cold-state $f_r$ value, the wireless actuation tests were performed by scanning $f_m$ from 150 MHz to 320 MHz at a constant output power of 0.7 W while measuring the temperature and out-of-plane displacement of the device simultaneously. Figure 5.8 shows a typical measured response. The results indicate a temperature peak of 71 °C when $f_M$ = ~230 MHz, which matches $f_R$ of the device at its flat condition (that has 48 nH and 10 pF). The results also indicate that the actuator was activated and deactivated at about 51 °C (in heating, $f_M$ = 210 MHz) and 39 °C (in cooling, $f_M$ = 270 MHz), respectively. The full displacement to the flat condition was reached when $f_M$ = 226 MHz (at 70 °C), and the actuator started to make a returning displacement when $f_M$ was increased beyond 244 MHz (at 59 °C); this suggests a full-actuation frequency range (the difference between these two $f_M$ values) of 18 MHz. These measured threshold temperatures are slightly higher than the

actual austenite finish temperature (corresponding to the point of the full actuation measured at 70 °C) and the martensite start temperature (corresponding to the point of initiating the returning displacement measured at 59 °C) that were measured to be 65 °C and 55 °C, respectively, for the SMA material used. The small discrepancy in these temperature values is presumably related to the location on the actuator that these temperatures were captured, which was one of the inner turns of the coil near its center. It was found that temperatures on the inner turns, including the location of the measurement point, were higher than those on the outer turns (this tendency can be seen in the IR images to be shown in Figure 5.12 later) – this condition likely led to the above discrepancy although the average actuator temperature is expected to be closer to the rated threshold temperatures.

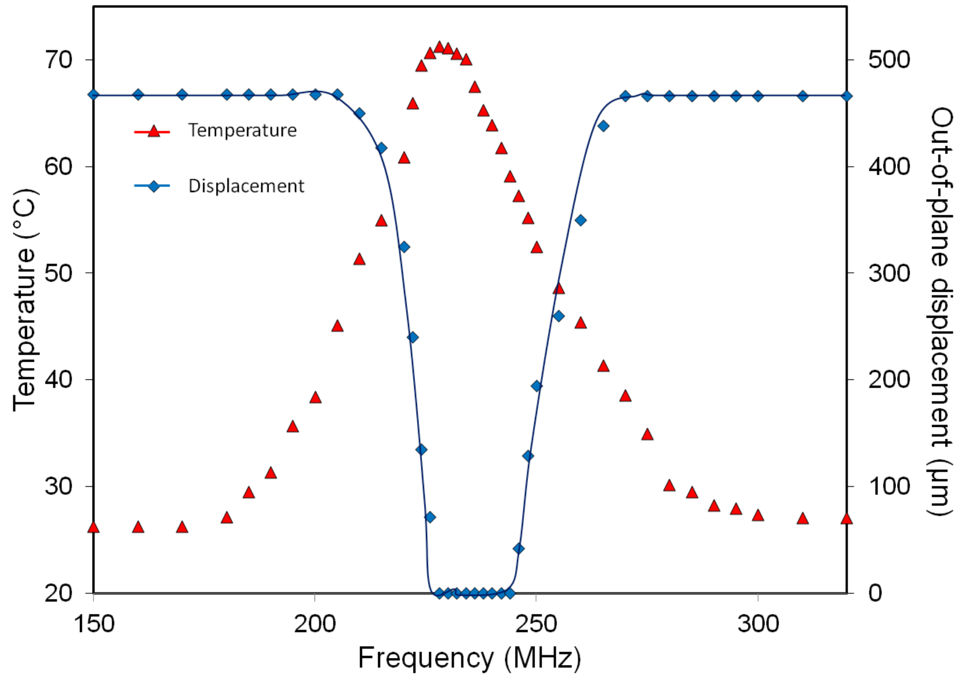


**Figure 5.8:** Measured actuator's temperature and displacement vs. $f_m$.

It was observed from the wireless resonance measurement that $f_r$ shifted to ~231 MHz at the fully actuated flat state (from ~238 MHz at the cold state), resulting in $\Delta f_r$ of ~7 MHz

(Figure 5.9) (this result agrees with the result reported in Figure 5.8 where the maximum temperature measured when $f_m$ was tuned to ~230 MHz which matches with $f_r$ of the device at austenite phase). The $\Delta f_r$ is led by a change in the inductance of the SMA coil, from 45 nH to 48 nH, upon the full displacement as discussed in Section 5.4.1. Another fact observed in Figure 5.9 is that the bandwidth of the actuator's resonance widened (from 45 MHz to 53 MHz at half of the S11 dips), i.e., the Q-factor dropped as the coil actuated to the flat state. Although the actuation causes a 6.7% increase in the coil inductance (which increases the Q-factor and narrows the resonant width) with the actuation, the observed result is likely dominated by the change in the SMA resistivity. When the coil is actuated from its cold 3D state to the excited flat state, the resistivity ($\rho$) of the SMA used in this study increases 7.9%, from 76 μΩ·cm (at the martensite phase) to 82 μΩ·cm (at the austenite phase), respectively, thus the parasitic resistance of the coil, $R_p$, increases as well. Since the Q-factor of an LC tank depends more on $R_p$ (or $\rho$) than $L$ as it is proportional to $L^{1/2}/R_p$, the above changes in $L$ and $\rho$ suggest a decrease in the Q-factor of the coil when actuated to the flat shape.

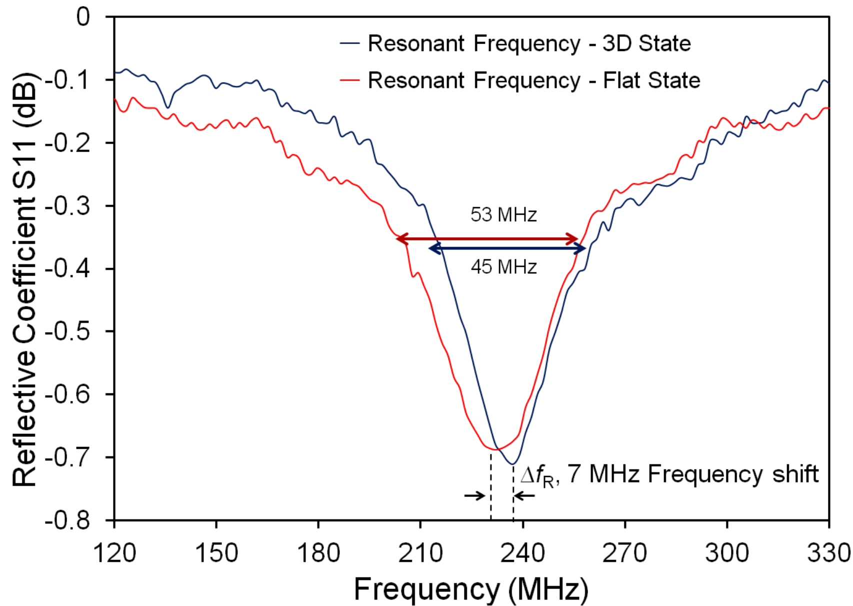


**Figure 5.9:** Measured $f_r$ of the SMA LC tank at the planar and 3D states.

**C: Frequency response: Force**

There are two types of the force generated by the actuator when it is operated. One of them involves the force produced when the actuator is excited and displaced from its 3D state to flat state. This force is generated by the SMA itself, through its phase transformation from the martensite to the austenite phase. The other force is involved in the returning deformation from flat to 3D; this restoring force is induced only by the reset compressive layer of $SiO_2$ (i.e., the SMA does not contribute to this returning motion). The force measurements were performed in both paths to evaluate these two forces. As illustrated in Figure 5.10, for the measurement of the SMA force, a force gauge was located underneath the actuator that pushed the gauge's probe downward when activated, and for the restoring force measurement, the gauge was located on top of the actuator that pushed the probe upward when deactivated. In both cases, the probe was pointed to the center of the coil.

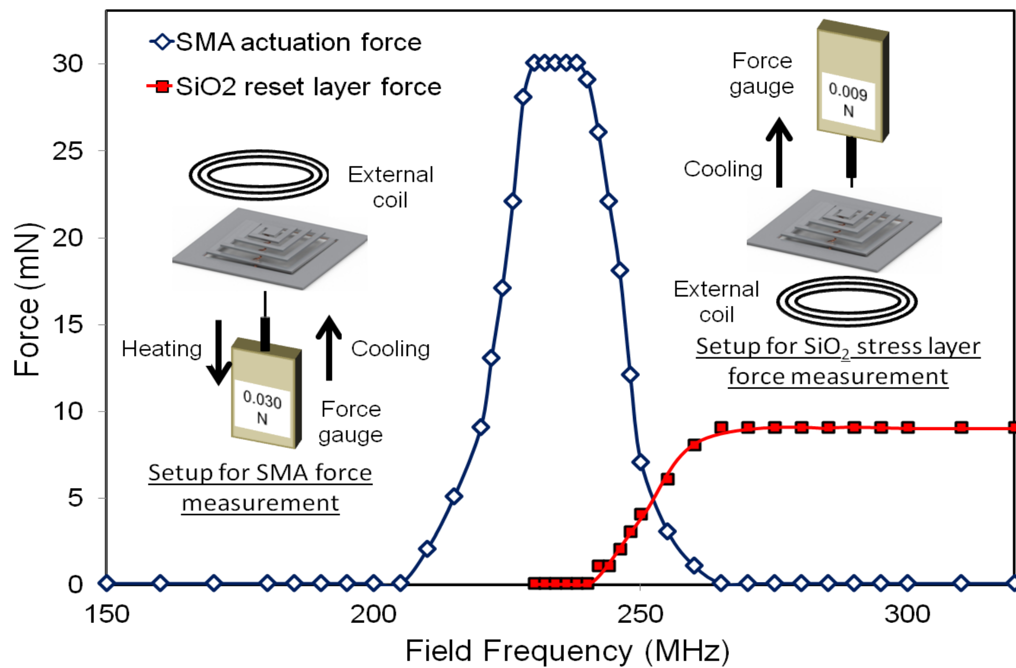


**Figure 5.10:** Measured force generated by each of the SMA and $SiO_2$ layers vs. $f_m$ (inset images show the set-ups used for both measurements).

The SMA force measurement was performed while scanning $f_M$ from 150 MHz to 320 MHz, and the restoring force was measured with $f_M$ scanned from 230 MHz (at the full actuation/flat state) to 320 MHz. As shown in Figure 5.10, the maximum SMA force of 30 mN was recorded when $f_M$ was within the range between 230 MHz and 238 MHz. This range is located approximately in the middle of the frequency range for the full actuation shown in Figure 5.8. The force rapidly decreased and diminished as $f_M$ was raised beyond 238 MHz. For the restoring force, the maximum value of 9 mN was recorded when $f_M$ reached 265 MHz. This experiment verifies that, as expected, the SMA provides a larger force than the $SiO_2$ reset layer, and that the former force is more than 3× greater than the latter one.

**D. Temporal response**

Figure 5.11 shows measured variations in the temperature and displacement of the actuator when repeated excitations were performed using an external RF field with 1-W output power at $f_m = f_r$ (231 MHz). As can be seen, the time for the actuator to achieve the full displacement of 466 µm from the 3D state (at ~40 °C) to the flat state (at ~73 °C) was ~3 s, whereas the time to return to the original 3D state after turning off the field was ~4 s. These suggest that this actuator may be operated for the full-range actuation in a 7-s cycle (0.14 Hz) with the setup used in this experiment. The time response of the actuator also depends on the RF output power as well as on the device design/size, including the property of the SMA material (i.e. the hysteresis between the martensite-phase and austenite-phase temperatures). However, it is evident from comparison with the case that used separate heaters as reported in Chapters 3 and 4 that the developed device provides 2-3× faster responses than the previous results while requiring lower temperatures for full actuations. This large improvement is mainly attributed to the actuator's design, in which the actuator

itself generates heat (as the wireless resonant heater) and thus causes less thermal energy loss, leading to faster responses. In addition, the lower thermal capacity of the SMA compared to PI which was used to fabricate the heater for the devices in previous chapters improves the response of the actuator during cooling cycle.

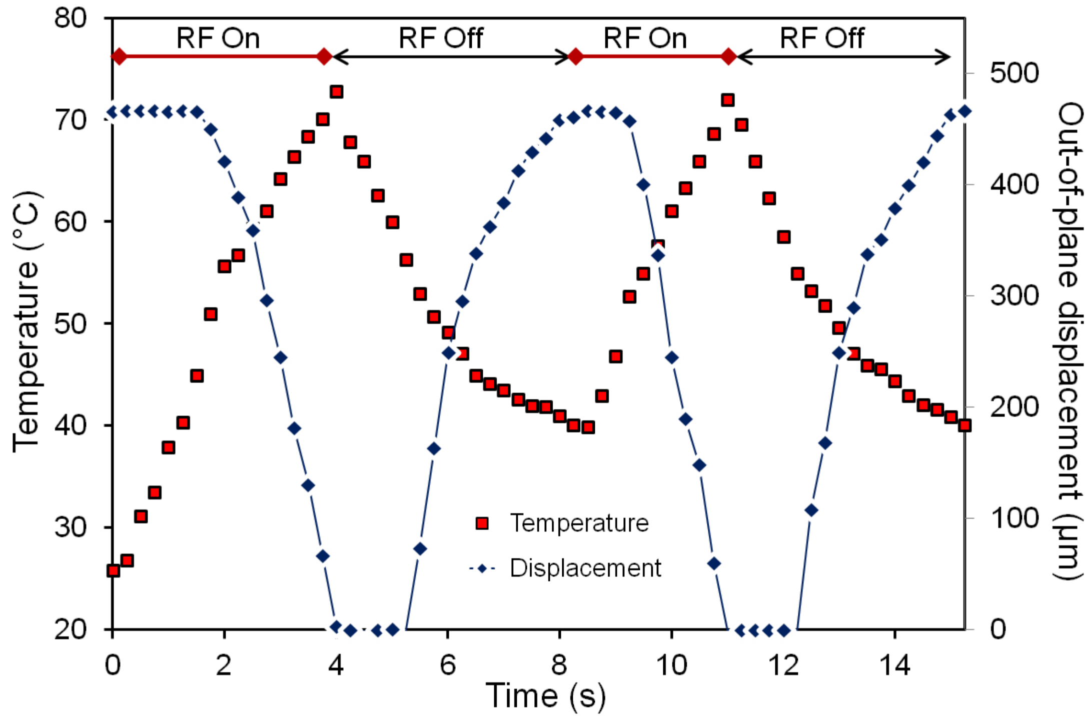


**Figure 5.11:** Measured actuator's temperature and displacement caused by repeated excitations of the actuator implemented using an RF field at $f_m = f_r$.

The IR images of the SMA actuator captured during a heating and cooling cycle are shown in Figure 5.12. It can be seen that when the SMA coil was excited, the inner turns of the coil tend to have higher temperature compared to the outer turns, resulting in a temperature gradient with higher temperatures in the inner turns as discussed in Section 5.4.2 B. This might be caused by the denser magnetic flux towards the center of the coil that led to maximum heating in this area [177].

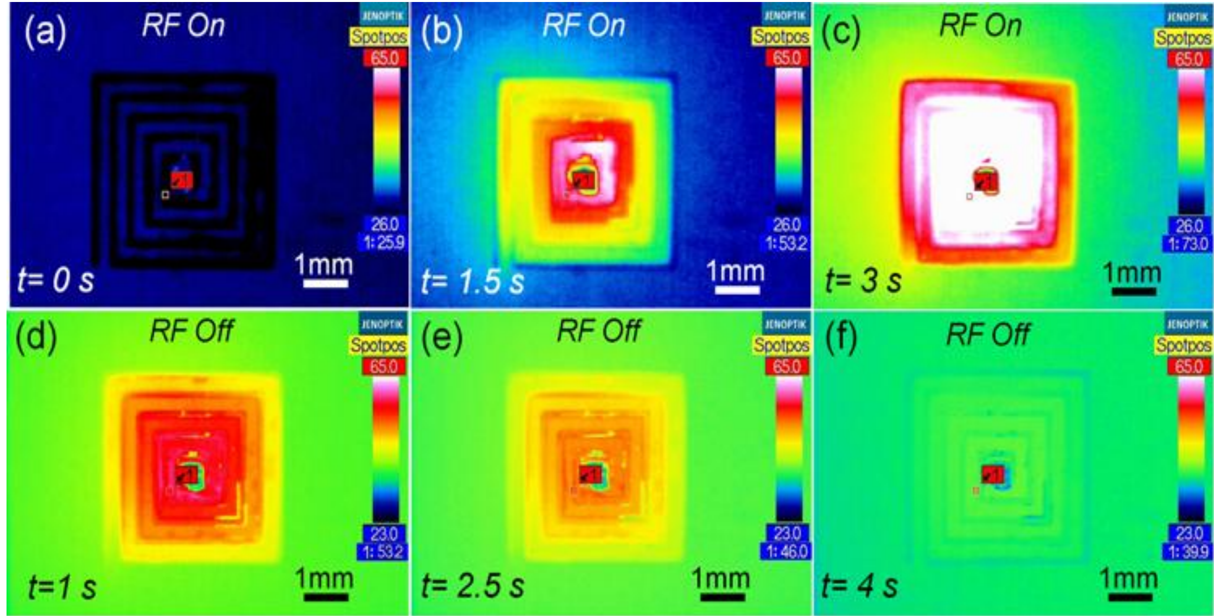


**Figure 5.12:** IR images of the actuator; (*a*-*c*) during heating cycle when an RF field with $f_m$ = 231 MHz and 1-W power is applied; (*d*-*f*) during cooling cycle after the full actuation.

### 5.4.3 Wireless Displacement Monitoring

A wireless resonant sensing mechanism using LC circuits has been utilized in many applications [178-185]. Various physical parameters such as temperature, pressure, pH and force have been wirelessly measured. LC circuits are arranged so that an environmental parameter causes a change in its inductance or capacitance that contributes to a shift in its $f_r$. In this section, we demonstrate a wireless displacement tracking method for an out-of-plane spiral coil SMA that forms an LC circuit.

The change in $f_r$ of the actuator was monitored using the setup illustrated in Figure 5.7 with an additional monitoring coil placed 2 mm above the actuator. A monitoring coil (7 mm in diameter, ~380 nH) was connected to an Agilent network analyzer that was interfaced with a computer through a Labview software program. $f_r$ was sampled at a 20 Hz frequency (every 50 ms) with a frequency tracking resolution of 50 kHz. The sampling frequency and resolution are related to the computational limitation and the response time of the analyzer.

The actuator was excited by the excitation coil placed beneath the actuator as implemented before, while the displacement was measured by a laser displacement sensor. Figure 5.13 plots the relationship between $f_r$ and the out-of-plane displacement when the actuator was excited using 1 W of power at $f_m$ = 231 MHz.

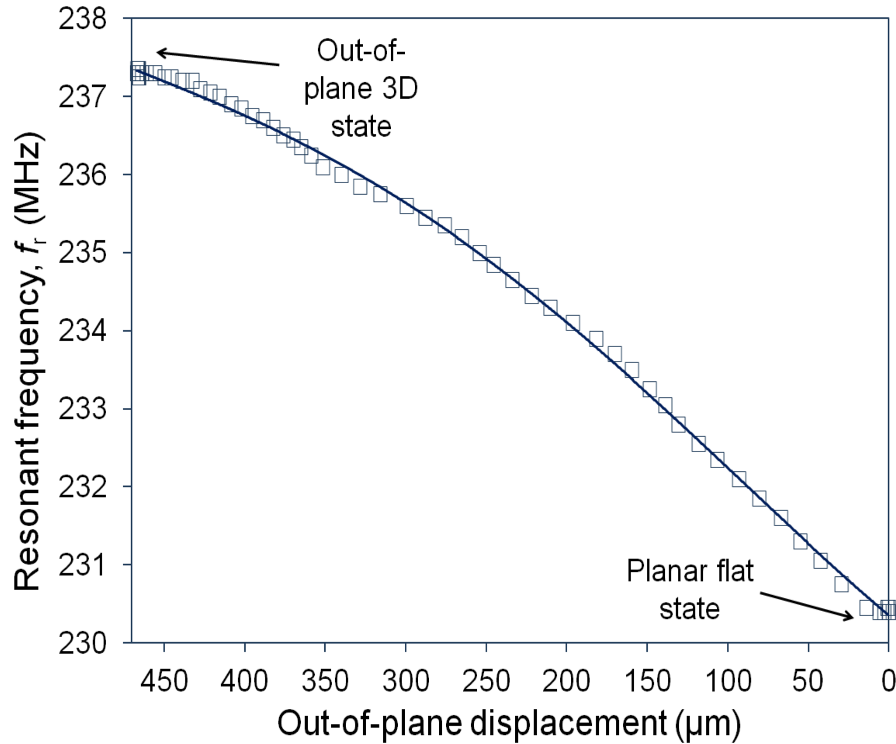


**Figure 5.13:** Measured $f_r$ vs. out-of-plane displacement when $f_m$=231 MHz.

Similar to the $f_r$ measurement reported in Section 5.4.2 B (Figure 5.9), the result plotted in Figure 5.13 shows that the actuator has $f_r$ of ~237.5 MHz in the 3D state and reduces to ~230.5 MHz when it was actuated to a flat condition. The $f_r$ shows higher changes at larger displacements towards flat condition. This might be related to the influence of the outer turns of the coil to the change in the inductance value, where at a larger displacement, the outer turn of the coil which has a large influence on inductance value was displaced. On average, the sensitivity of $f_r$ is calculated at ~14 kHz/μm. The displacement and $f_r$ tracking were repeated

at the same power but at different $f_m$ and plotted in Figure 5.14 to show the ability to control the out-of-plane displacement at the desired level while wirelessly monitoring the $f_r$.

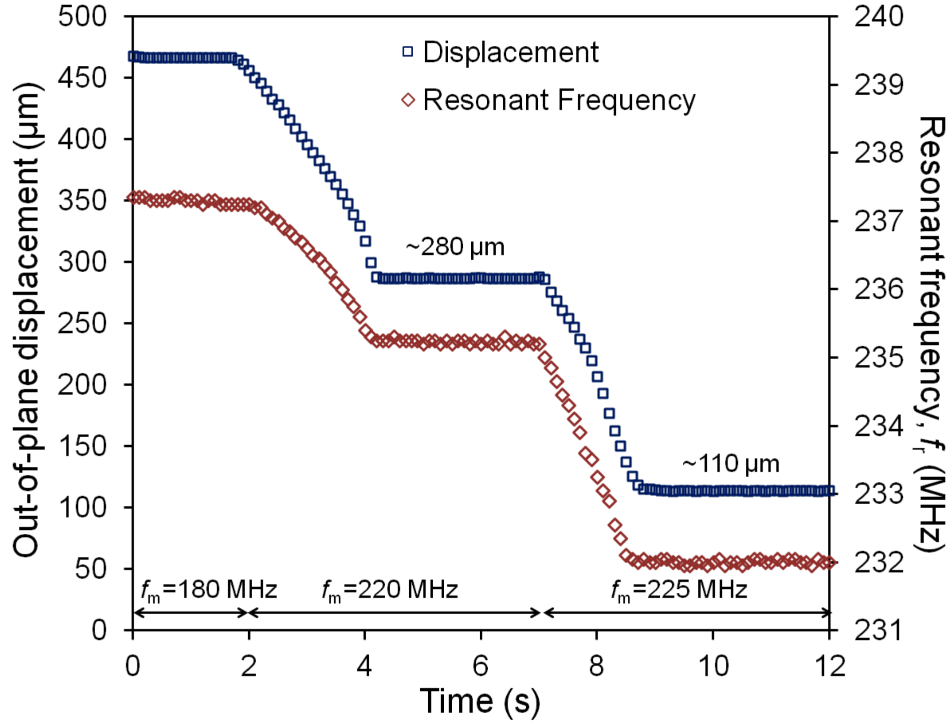


**Figure 5.14**: Wireless resonant tracking when $f_m$= 180 MHz, 200 MHz and 225MHz.

During the first 2 seconds of the measurement results plotted in Figure 5.14, the $f_m$ is set at 180 MHz. In this period, not much change was observed in $f_r$ as there has not been any displacement in the actuator. When the $f_m$ was changed from 180 MHz to 220 MHz at the 2$^{nd}$ second, the actuator is displaced from ~466 µm to ~280 µm. Due to this displacement, $f_r$ shifts from 237 MHz to ~235 MHz. The calculated sensitivity is given at 10.8 kHz/µm. The actuator settles at ~280 µm after 2 s, and the $f_m$ is tuned to 220 MHz. Until the 7$^{th}$ second, there is no significant change in $f_r$ recorded. The $f_m$ is then further tuned to 225 MHz at the 7$^{th}$ second. At this stage, the actuator is displaced in less than 2 seconds to ~110 µm and a shift in $f_r$ to ~232 MHz was observed. This shift corresponds to a sensitivity of 17.6 kHz/µm. The trend of the change in $f_r$ and displacement basically reveal a similar response as in Figure 5.13.

As described earlier, the higher change in $f_r$ is contributed to the displacement of the outer turn of the coil and the delay to achieve more uniform heating throughout the coil.

This measurement proves that wireless displacement monitoring of the fabricated device is possible. In addition, the displacement of the actuator can also be precisely controlled by applying a specific $f_m$. However, in order to attain more accurate displacement tracking, the quality factor of the actuator must be improved. It can be observed that $f_r$ reading plotted in Figure 5.14 reveals some fluctuation when the actuator is in the steady state, particularly when the actuator is approaching the austenite phase of the SMA.

### 5.4.4 Coil Optimization

One of the important factors in wireless RF resonant sensing is to achieve a high Q-factor. In this chapter, SMA which has a high resistivity is used to form the coil inductor. Although the actuator demonstrated better temporal response compared to the result reported in Chapter 3 and Chapter 4, high power is used to excite the actuator. This is mainly due to the low Q-factor of the SMA coil. Since the low Q-factor is due to the low conductivity of the SMA, this issue may be resolved by coating the SMA coil with a highly conductive material such as Cu.

In this section, the effect of Cu-layer coating is investigated to evaluate the impact on the Q-factor of the coil. For this analysis, a 35-μm-thick SMA coil is prepared with the same dimensions as those described in Section 5.2 but without the $SiO_2$ stress layer on the SMA (Figure 5.4(a)). The measurement is performed using an Agilent impedance analyzer. Silver paste is employed to create a connection with the centre of the coil. After the electrical characterization of the original SMA coil, the coil is coated with a of Ta/Cu seed layer through sputter deposition. Then, a 5-μm-thick Cu was electroplated onto the coil. Figure

5.15 shows the SMA coil with its Cu layer prepared for characterization. Figures 5.16(a) and (b) show the resistance, inductance and Q-factor measurement results of the SMA coil before and after employment of the Cu-layer coating.

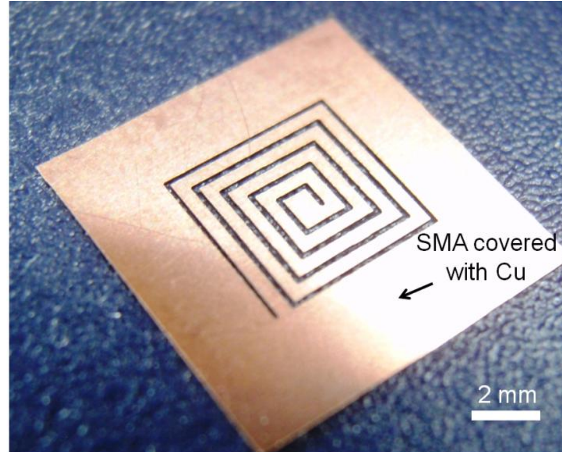


**Figure 5.15:** A SMA coil coated with Cu.

A significant improvement in the resistance of the SMA coil was observed after coating Cu layer (Figure 5.16(a)). Without the Cu layer, the SMA coil has a resistance of 5.5 Ω; this is reduced to 2.7 Ω after the Cu coating. This reduction corresponds to a ~50 % improvement in the coil's conductivity. In terms of the coil's inductance, no noteworthy change is observed (Figure 5.16(b)). The Q-factor of the coil reveals a significant increase when the Cu-layer is deposited, with an increase of 85 % from the original value of 10.5 to 19 recorded.

This result proves that with a good conductive material coating, the quality factor of the SMA coil can be improved. In this experiment, a Cu-layer thickness of 5 µm is selected in consideration of skin effect, which is estimated to be 4.3 µm when the coil is operated at 231 MHz. Further increased of the Cu thickness may not contribute to a significant increase in the Q-factor due to the skin effect and also may cause deleterious impact on the displacement as the coating can stiffen the SMA beams.

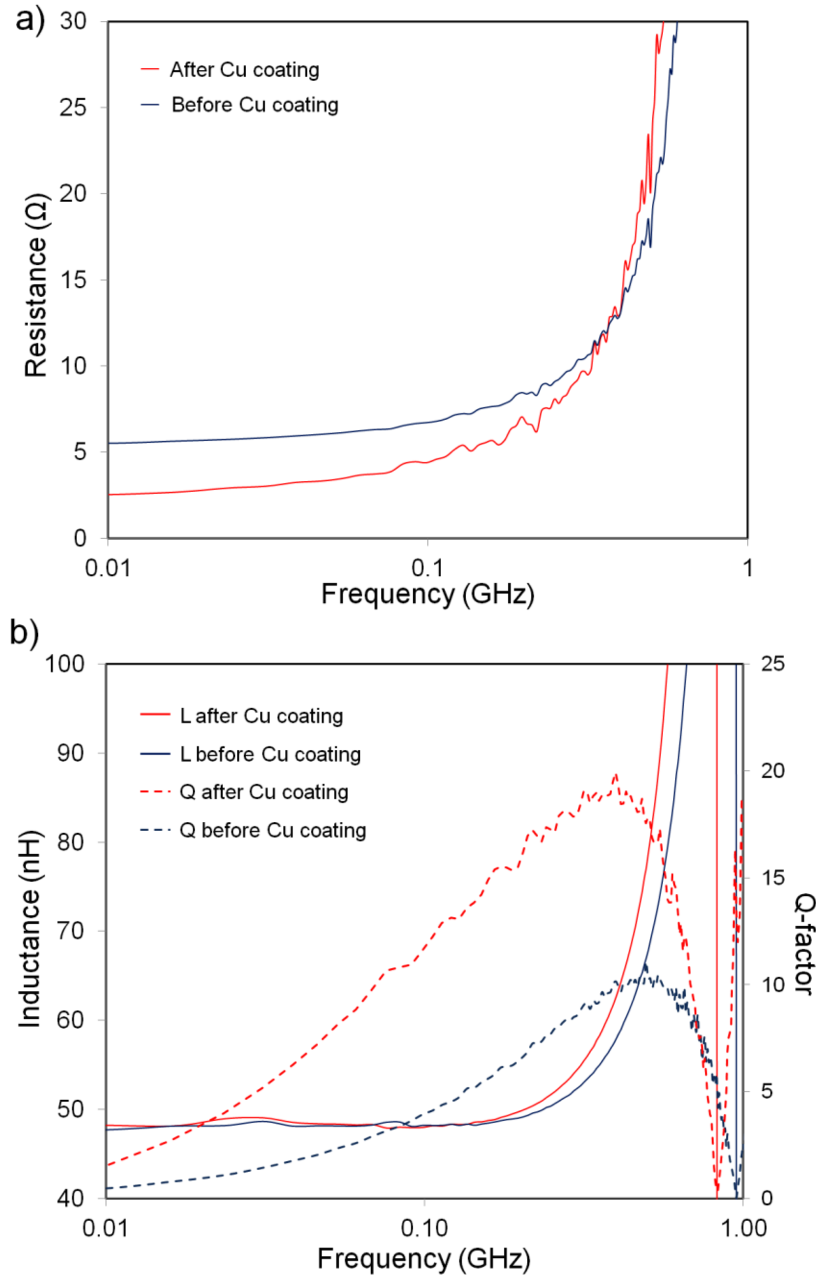


**Figure 5.16:** Electrical characterization of an SMA coil before and after Cu-layer coating; (a) resistivity measurement; and (b) L and Q-factor measurements.

## 5.5 Conclusion

A novel SMA actuator that is directly powered and controlled with RF fields has been designed, fabricated, and demonstrated. The SMA was bulk micromachined to form a planar

spiral-coil inductor that constituted an LC resonant circuit, which was used as a radio-controlled built-in heat source to produce vertical displacements in the SMA coil. The fabricated SMA LC tank was observed to provide an inductance of 48 nH and a Q-factor of 11 with a self resonance at 1.5 GHz. The self-assembly of SMA 3D spiral coils was achieved using patterned bimorph structures with the $SiO_2$ reset layer locally defined on the planar SMA coils, yielding an out-of-plane displacement of 466 μm in the fabricated SMA coils. The actuation of the devices was implemented through direct heating of the SMA coil through the wireless excitation of the SMA LC tank using external RF fields by tuning $f_m$ to $f_r$ of the tank. The actuation of the SMA, which had an austenitic phase temperature of 65 °C, was successfully controlled only within 5 °C above the threshold temperature based on the RF excitation technique. The ranges of the RF output power and operation frequency used were 0.7-1 W and 230-240 MHz, respectively. The fabricated devices were characterized to produce vertical actuation forces of up to 30 mN in their 3D-to-planar actuation path. The observation for dynamic behaviors of the SMA actuator revealed a markedly improved temporal response compared to the previously developed SMA actuators that were coupled with separate wireless heat sources, suggesting the effectiveness in the use of the built-in wireless heat source adopted in the present device. In addition, the shift in $f_r$ that the actuator exhibited during the actuation was shown to represent actual displacements of the actuator by monitoring the frequency wirelessly, potentially enabling high-precision radio control of the actuation through real-time tracking of the resonant frequency. The improvement in the Q-factor of the SMA actuator demonstrated by coating a Cu layer may further improve the performance of the actuator.

# Chapter 6

# Conclusion

In this dissertation, we have reported a wireless control method for the bulk-micromachined SMA actuator. A complete form of the research which includes the modeling, simulation, fabrication and experimental verification of the wireless SMA actuator is reported. A summary of the contributions from the research conducted and the future direction of this research is presented in this chapter.

## 6.1 Contributions

The research contributions are presented in the following chapter sequence:

### I. Chapter 2

In this chapter, the LC resonant circuits which were used as frequency sensitive wireless heaters were characterized in detail. The scaling effect on the wireless power transfer efficiency and other key parameters as functions of the inductor's number of turns and line widths were evaluated. Each coil that used in the experiment was well analyzed in terms of its resistivity, inductance, capacitance, resonant frequency and Q factor. The coupling coefficients between the transmitter and the receiver coils (wireless heater) were also examined. The effect of the increase in the separation distance between the coils was also experimentally verified. In addition, the measurement results were compared with the theoretical model. A simplified model to estimate the steady state temperature at the coil was

developed based on the model reported in [111] and the results were compared with the actual measurements.

## II. Chapter 3

The feasibility of the wireless actuation of the bulk-micromachined SMA actuator that is controlled using the novel RF magnetic field control method has been verified, and its application as a micro gripper has also been demonstrated in this chapter. The developed method has advantages in terms of the device's longevity, size and applicability in the application where the space and access are limited, as compared with any other reported wireless SMA actuation technique including the laser and electron beam method [34, 35]. A new integration technique using the photo-defined electroplating bonding method was developed to bond the bulk-micromachined SMA to the planar LC circuit. The bonding strength between the SMA and LC circuit was experimentally studied and revealed that the reported technique has a higher bonding strength than most of the polymer based bonding. This batch compatible integration scheme could also enable the use of any bulk micromachined material into the MEMS fabrication. The SMA based wireless gripper that was fabricated through the electroplating bonding method was demonstrated to manipulate the vertically aligned CNT forest using the developed RF control method.

## III. Chapter 4

In this chapter, we have reported a wireless control method for the selective and simultaneous control of multiple SMA actuators using the frequency modulation technique. The wireless control of the multiple actuators method developed in this work is a key to achieving novel functionalities while enhancing the devices' performance. For implantable drug-delivery devices, for example, this ability may be utilized to enable the controlled and

selective delivery of different types of drugs at specific mixtures. We have demonstrated the viability of the frequency modulation technique to control multiple SMA actuators that were integrated to the LC resonance circuits. This was demonstrated in a microfluidic device designed as a microinjector, which integrated three actuators with the LC heaters, demonstrating controlled release of liquid for pH level adjustment by selective control of the three actuators. The thermal response of the fabricated device was also characterized using different power levels.

### IV. Chapter 5

An out-of-plane SMA actuator in the form of a spiral coil has been designed, fabricated and reported in this chapter. We have demonstrated that an out-of-plane displacement in a planar spiral coil can be achieved using a localized stress layer. The developed technique using a simple lithography and bimorph process could also be used to build various 3-D structures by using patterned stress layers which previously required complex processes and tools. The vertically displaced SMA spiral coil with a planar parallel plate capacitor that was fabricated on the SMA formed an LC resonant circuit. The displacement of the SMA spiral-coil actuator in its out-of-plane direction was wirelessly controlled using external RF magnetic fields. We also reported a wireless position monitoring method by tracking the change in the resonant frequency of the out-of-plane spiral LC circuit. By controlling the external field frequency, precise displacement control and monitoring were demonstrated where discrete frequencies correspond to a specific degree of displacement. The force induced by the SMA and the stress layer were also measured and reported.

## V. Appendix

The out-of-plane spiral coil formation technique that used a localized stress layer, reported in Chapter 5, was applied to study a novel microfabrication/assembly method for an out-of-plane copper planar inductor that was permanently displaced to achieve controlled height and final inductance. The permanent out-of-plane displacement was achieved by controlling the plastic deformation on the copper coil using specific annealing temperature. This method allows the inductance of the planar coils to be determined by adjusting the annealing temperature without the need for changing the base dimensions of the coil.

Based on the specific contributions as described by chapter, the contribution of this research can be summarized as a development of the fully passive wireless SMA actuator. To the best of our knowledge, this research was the first to report the wireless actuation of thermal actuators using an RF magnetic field without the use of batteries and/or active circuitries. Although there was a report on the passive SMA actuation using the RF magnetic field [110, 111], it needed to use rectification and conditioning circuits. In our case, the electromotive force induced at the coil is effectively converted to Joule heat to drive the SMA and this eliminates the need for additional conditioning circuits. This eventually reduces the size of the devices which is an important parameter in designing implantable devices. In terms of the fabrication method, in this research, the devices were fabricated by combining non-traditional micromachining methods such as μEDM with standard MEMS fabrication methods such as lithography, E-beam deposition, sputter disposition, RIE, PECVD, and electro-chemical deposition. We also integrated bulk materials such as the SMA sheet, and non-traditional materials such as parylene into the standard MEMS fabrication process. The developed fabrication processes to realize the devices prove that unique and high performance

MEMS devices can be built by combining non-traditional micro-machining process and materials with standard MEMS fabrication approach. The techniques and results demonstrated in this research suggest many opportunities of the developed wireless SMA actuators especially in biomedical areas.

## 6.2 Future Work

With suitable optimization and packaging, the developed wireless actuators may be used for a variety of applications in biomedical areas, e.g., wireless control of micropumps and valves in implantable microfluidic devices. In this work, the wireless actuation was focused onto the actuation of SMA actuators. However, the developed wireless actuation principle can be extended to the control of other thermal actuators such as bimorphs and thermoresponsive hydrogels [154, 186]. Future work will involve the optimization of the device design and fabrication as well as further integration and miniaturization of the actuator module.

# Bibliography

[1] D. Peroulis, S. P. Pacheco, K. Sarabandi, and L. P. B. Katehi, "Electromechanical Considerations in Developing Low-Voltage RF MEMS Switches," *Transaction IEEE Microwave Theory Techniques,* vol. 51(1), pp. 259- 270, 2003.

[2] H. Wijshoff, "Structure and Fluid-Dynamics in Piezo Inkjet Printheads," *PhD Thesis*, University of Twenty, Enschede, Netherland, 2008.

[3] C. D. Meinhart and H. Zhang, "The Flow Structure Inside a Microfabricated Inkjet Printhead," *Journal of Microelectromechanical System*, vol. 9, pp. 67-75, 2000.

[4] S. A. Khan and N. A. Riza, "Demonstration of the MEMS Digital Micromirror Device-Based Broadband Reconfigurable Optical Add–Drop Filter for Dense Wavelength-Division-Multiplexing Systems", *Journal of Lightwave Technology*, vol. 25(2), pp. 520-526, 2007.

[5] A. Menciassi, G. Scalari, A. Eisinberg, C. Anticoli, P. Francabandiera, M. C. Carrozza, and P. Dario, "An Instrumented Probe for Mechanical Characterization of Soft Tissues," *Biomedical Microdevices*, vol. 3(2), pp. 149–156, 2001.

[6] M. O. Schurr, S. P. Heyn, W. Ment, G. Buess, "Endosystems - Future Perspectives for Endoluminal Therapy," *Minimally Invasive Therapy Allied Technology*, 7(1), 37–42. 1998.

[7] N. M. Elman, Y. Patta, A. W. Scott, B. Masi, H. L. Ho Duc, and M. J. Cima, "The Next Generation of Drug-Delivery Microdevices," *Clinical pharmacology & Therapeutics*, vol. 85(5), pp. 544-547, 2009.

[8] H. Abdi, M. Asgari, and S. Nahavandi, "Active Surface Shaping for Artificial Skins," *IEEE Conference on Systems Man, and Cybernetics*, Anchorage, AK, 9-12 Oct. 2011, pp.2910-2915.

[9] N. Maluf and K. William, *An Introduction to Microelectromechanical Systems Engineering*, 2nd Ed. Artech House, Boston, USA, 2004.

[10] Y. Zhang, G. Ding, S. Fu, and B. Cai, "A Fast Switching Bistable Electromagnetic Microactuator Fabricated by UV-LIGA Technology," *Mechatronics*, vol. 17, pp. 165-171, 2007.

[11] H. Fujita, "Studies of Micro Actuators in Japan," *Proceeding IEEE Robotics and Automation*, Scottsdale, AZ USA, May 14-19, 1989, pp.1559–64.

[12] E. Thielicke and E. Obermeier, "Microactuators and Their Technologies," *Mechatronics*, vol. 10, 431–455, 2000.

[13] A. K. Poddar and K. N. Pandey, "Microwave Switch using MEMS-Technology," *Proceeding IEEE High Performance Electron Devices, Microwave, Optoelectronics, and Application*, Glasgow, UK, November 13-14, 2000, pp. 134–139.

[14] P. Sumant, A. Cangellaris, and N. Aluru, "Modeling of Dielectric Charging in RF-MEMS Capacitive Switches," *Microwave Optical Technology Letter*, vol. 49(12), pp. 3188–3192, 2007.

[15] C. Goldsmith, J. Ehmke, A. Malczewski, B. Pillans, S. Eshelman, Z. Yao, J. Brank, and M. Eberly, "Lifetime Characterization of Capacitive RF MEMS Switch," *Proceeding IEEE Microwave*, Phoenix, AZ, USA, May 20-25, 2001, pp. 227–230.

[16] J. E. Huber, N. A. Fleck, and M. F. Ashby, "The Selection of Mechanical Actuators Based on Performance Indices," *Proceeding of Royal Society A*, vol. 453, pp.2185–2205, 1997.

[17] N. J. Conway, Z. J. Traina, and S. G. Kim, "A Strain Amplifying Piezoelectric MEMS Actuator, *Journal of Micromechanics and Microengineering*, vol. 17, pp. 781–787, 2007.

[18] C. H. Ko, J. J. Yang, and J. C. Chiou, "Efficient Magnetic Microactuator with an Enclosed Magnetic Core," *Journal of Microlithography, Microfabrication and Microsystem*, vol. 1(2), pp. 144–149, 2002.

[19] S. Braun, "Wafer-Level Heterogeneous Integration of MEMS Actuators," *PhD thesis*, Royal Institut of Technology, Stocholm, Sweden, 2010.

[20] J. Mattey, "Using Shape Memory Alloy," *Johnson Mattey Engineering Reference* © 2004.

[21] F. J. Gil, J. A. Planell, "Shape Memory Alloys for Medical Applications," *Proceedings of the Institution of Mechanical Engineers, Part H: Journal of Engineering in Medicine*, vol. 212, pp. 473-488, 1998.

[22] Y. Bellouard, R. Clavel, R. Gotthardt, J. E. Bidaux, T. Sidler, "A New Concept of Monolithic Shape Memory Alloys Micro-devices used in Micro-Robotics," *International Conference on New Actuators*, Bremen, Germany, June 17-19, 1998, pp.

88-91.

[23] J. Madden, N. Vandesteeg, P. A. Anquetil, P. G. Madden, A. Takshi, R. Z. Pytel, S. R. Lafontaine, P. A. Wieringa, I. W. Hunter, "Artificial Muscle Technology: Physical Principles and Naval Prospects," *IEEE Journal of Oceanic Engineering*, vol. 29, pp. 706-725, 2004.

[24] K. Shimizu, T. Tadaki, *Shape Memory Alloys*, Ed. H. Funakubo, , Gordon and Breach Science Publishers 1987.

[25] N. B. Morgan, "Medical Shape Memory Alloy Applications – The Market and Its Products," *Material Science Engineering A*, vol. 378, pp. 16-23, 2004.

[26] P. Krulevitch, A. Lee, P. Ramsey, J. Trevino, J. Hamilton, and M. Northrup, "Thin Film Shape Memory Alloy Microactuators," *Journal of Microelectromechanical System*, vol. 5 (4), pp. 270–282, 1996.

[27] R. X. Wang, Y. Zohar, and M. Wong, "Residual Stress-Loaded Titanium–Nickel Shape-Memory Alloy Thin-Film Microactuators," *Journal of Micromechanics and Microengineering*, vol. 12, pp. 323–327, 2002.

[28] J. J. Gill, K. Ho, and G. P. Carman, "Three-Dimensional Thin-Film Shape Memory Alloy Microactuator With Two-Way Effect," *Journal of Microelectromechanical System*, vol. 11 (1), pp. 68-77, 2002.

[29] M. Tomozawa, H. Y. Kim, S. Miyazaki, "Films Microactuators Using R-phase Transformation of Sputter-deposited Ti-47.3Ni Shape Memory Alloy Thin," *Journal of Intelligent Material, Systems and Structures*, vol. 17, 1049-1058, 2006.

[30] J. L. Seguin, M. Bendahan, A. Isalgue, V. E. Cano, H. Carchano, and V. Torra, "Low Temperature Crystallised Ti-Rich NiTi Shape Memory Alloy Films for Microactuators," *Sensors and Actuators A Physical*, vol. 74, pp. 65–69, 1999.

[31] N. Frantz, E. Dufour-Gergam, J. P. Grandchamp, A. Bosseboeuf, W. Seiler, G. Nouet, and G. Catillon, "Shape Memory Thin Films with Transition Above Room Temperature from Ni-Rich NiTi Films," *Sensors and Actuators A: Physical*, vol. 99, pp. 59-63, 2002.

[32] E. Makino, T. Mitsuya, and T. Shibata, "Fabrication of TiNi Shape Memory Micropump," *Sensors and Actuators A: Physical*, vol. 88, pp. 256-262, 2001.

[33] Q. Pan and C. Cho, "The Investigation of a Shape Memory Alloy Micro-Damper for MEMS Applications," *Sensors*, vol. 7, pp. 1887-1900, 2007.

[34] J. K Paik, E. Hawkes, and R. J. Wood, "A Novel Low-Profile Shape Memory Alloy Torsional Actuator," *Smart Material and Structures*, vol. 19, 125014 (9pp), 2010.

[35] S. Braun, N. Sandström, and G. Stemme, "Wafer-Scale Manufacturing of Bulk Shape-Memory-Alloy Microactuators Based on Adhesive Bonding of Titanium-Nickel Sheets to Structured Silicon Wafers," *Journal of Microelectromechanical System*, vol.18, pp. 1309-1317, 2009.

[36] N. Sandström, S. Braun, G. Stemme, and W. van der Wijngaart, "Waferscale Manufacturing of Robust Trimorph Bulk SMA Microactuators," *Proceeding New Actuators*, Bremen, Germany, 2008, pp. 382–385.

[37] Y. Nakamura, S. Nakamura, L. Buchaillot, and H. Fujita, "A Three-Dimensional Shape Memory Alloy Loop Actuator," *Proceeding IEEE MEMS*, Nagoya, Japan, 26 - 30 Jan 1997, pp 262-266.

[38] H. Kahn, M.A. Huff, and A.H. Heuer, "The Tini Shape-Memory Alloy and Its Applications for MEMS," *Journal of Micromechanics and Microengineering*, vol. 8 pp. 213-221, 1998.

[39] C. M. Pemble and B. C. Towe, A Miniature Shape Memory Alloy Pinch Valve, *Sensors and Actuators A physical*, vol. 77, pp. 145–148, 1999.

[40] D. Reynaerts, J. Peirs, and H. Van Brussel, "Shape Memory Microactuation for a Gastro-Intestinal Intervention System," *Sensors and Actuators A physical*, vol. 77, pp. 157–166, 1999.

[41] G. Rondelli, "Corrosion Resistance Tests on NiTi Shape Memory Alloy," *Biomaterials*, vol. 17, pp. 2003-2008, 1996.

[42] J. Van Humbeeck, M. Chandrasekaran, and L. Delaey, "Shape Memory Alloys: Materials in Action," *Endeavour*, vol. 15, pp. 148-54, 1991.

[43] M. Kohl, "*Shape Memory Microactuators*," Springer, Berlin, 2004.

[44] M. Bergamascol, P. Dario, and F. Salsedo, "Shape Memory Alloy Microactuators," *Sensors and Actuators A: Physical*, vol.21 -23, pp.253-251, 1990.

[45] K. Yang and C. L. Gu, "Design, Drive and Control of a Novel SMA-Actuated Humanoid Flexible Gripper," *Proceedings of the Institution of Mechanical Engineers, Part C: Journal of Mechanical Engineering Science*, vol. 222(7), pp. 1329-1337, 2008.

[46] A. Menciassi, G. Pernorio, and P. Dario, “A SMA Actuated Artificial Earthworm,” *Proceeding IEEE Robotics and Automation*, vol. 4, 2004, pp. 3282–3287.

[47] S. Vyawahare, S. Sitaula, S. Martin, D. Adalian, and A. Scherer, “Electronic Control of Elastomeric Microfluidic Circuits with Shape Memory Actuators,” *Lab on Chip*, vol. 8, pp. 1530–1535, 2008.

[48] W. L. Benard, H. Kahn, A. H. Heuer, and M. A. Huff, “Thin-Film Shape-Memory Alloy Actuated Micropumps,” *Journal of Microelectromechanical System*, vol. 7, pp.245-251, 1998.

[49] Y. Fu, W. Huang, H. Du, X. Huang, J. Tan, and X. Gao, “Characterization Of Tini Shape-Memory Alloy Thin Films For MEMS Applications,” *Surface Coating Technology*, vol. 145, pp. 107-112, 2001.

[50] Z. Wang, J. Hewit, E. Abel, A. Slade, and B. Steele, “Development of a Shape Memory Alloy Actuator for Transanal Endoscopic Microsurgery,” *Proceeding IEEE Engineering, Medicine, and Biology*, Shanghai, China, September 1-4, 2005, pp. 4341-4344.

[51] D. Reynaerts, J. Peirs, and H. Brussel, “An Implantable Drug-Delivery System Based on Shape Memory Alloy Micro-Actuation,” *Sensors and Actuators A physical*, vol. 61, pp. 455-462, 1997.

[52] Y. Fu, H. Du, W. Huang, S. Zhang, and M. Hu, “TiNi-Based Thin Films in MEMS Applications: A Review,” *Sensors and Actuators A physical*, vol.112, pp. 395-408, 2004.

[53] T. Duerig, A. Pelton, and D. Stöckel, “An Overview of Nitinol Medical Applications,” *Materials Science and Engineering: A*, vol. 273–275, pp. 149–160, 1999.

[54] L. Petrini and F. Migliavacca, “Biomedical Applications of Shape Memory Alloys,” *Journal of Metallurgy*, vol. 2011, 501483 (15 pages), 2011.

[55] C. D. J. Barras and K. A.Myers, “Nitinol—Its Use in Vascular Surgery and Other Applications,” *European Journal of Vascular and Endovascular Surgery*, vol. 19(6), pp. 564–569, 2000.

[56] P. Parashos and H. H. Messer, “The Diffusion of Innovation in Dentistry: A Review Using Rotary Nickel-Titanium Technology as an Example,” *Oral Surgery, Oral Medicine, Oral Pathology, Oral Radiology and Endodontology*, vol. 101(3), pp. 395–401, 2006.

[57] J. Szewczyk, E. Marchandise, P. Flaud, L. Royon, and R. Blanc, "Active Catheters for Neuroradiology," *Journal of Robotics and Mechatronics*, vol.23, pp. 105-115, 2011.

[58] A. Tung, B. Park, D. Liang, and G. Niemeyer, "Laser-Machined Shape Memory Alloy Sensors for Position Feedback in Active Catheters," *Sensors and Actuators A: Physical*, vol. 147, pp. 83-92, 2008.

[59] F. J. Gil, J. M. Manero, and J. A. Planell, "Relevant Aspects in the Clinical Applications of NiTi Shape Memory Alloys," *Journal of Materials Science: Materials in Medicine*, vol. 7, pp. 403-406, 1996.

[60] J. Y. Xiong, Y. C. Li, X. J. Wang, P. D. Hodgson, and C. E. Wen, "Titanium-Nickel Shape Memory Alloy Foams for Bone Tissue Engineering" *Journal of the Mechanical Behavior of Biomedical Materials*, vol. 1, pp. 269-273, 2008.

[61] K. Kuribayashi, K. Tsuchiya, Z. You, D. Tomus, M. Umemoto, T. Ito, and M. Sasaki, "Self-Deployable Origami Stent Grafts as a Biomedical Application of Ni-Rich TiNi Shape Memory Alloy Foil," *Materials Science and Engineering A*, vol. 419, pp. 131-137, 2006.

[62] D. Stoeckel, "Nitinol Medical Devices and Implants," *Minimally Invasive Therapy*, vol. 9(2), pp. 81-88, 2000.

[63] H. Scherngell and A.C. Kneissl, "Training and Stability of the Intrinsic Two-Way Shape Memory Effect in Ni-Ti Alloys," *Scripta Materialia*, vol. 39, pp. 205-212, 1998.

[64] T. Suguwara, K. Hirota, M. Watanabe, T. Mineta, E. Makino, S. Toh, and T. Shibata, "Shape Memory Thin Film Actuator for Holding a Fine Blood Vessel," *Sensors and Actuators A: Physical*, vol.130-131, pp. 471-467, 2006.

[65] T. Mineta, T. Mitsui, Y. Watanabe, S. Kobayashi, Y. Haga, and M. Esashi, "Batch Fabricated Flat Meandering Shape Memory Alloy Actuator for Active Catheter," *Sensors and Actuators A physical*, vol. 88, pp. 112-120, 2001.

[66] W. M. Huang, J. P. Tan, X. Y. Gao, and J. H. Yeo, "Design, Testing, and Simulation of NiTi Shape-Memory-Alloy Thin-Film-Based Microgrippers," *Journal of Microlithography, Microfabrication and Microsystem*, vol. 2, pp. 185-190, 2003.

[67] J. H. Prescott, S. Lipka, S. Baldwin, N. F. Sheppard, J. M. Maloney, J. Copetta, B. Yomotov, M.A. Staples, and J.T. Santini, "Chronic, Programmed Polypeptide Delivery From an Implanted Multireservoir Multi-Chip Device," *Nature*

*Biotechnology*, vol. 24, pp. 437-438, 2006.

[68] S. Smith, T. B. Tang, J. G. Terry, J. T. M. Stevenson, B. W. Flynn, H. M. Reekie, A. F. Myrray, A. M. Gundlach, D. Renshaw, B. Dhillon, Y. Inouse, and A.J. Walton, "Development of a Miniaturized Drug Delivery System with Wireless Power Transfer and Communication," *IET Nanobiotechnology*, vol. 1, pp. 80-86, 2007.

[69] T. B Tang, S. Smith, B. W. Flynn, J. T. M. Stevenson, A. M. Gundlach, H. M. Reekie, A. F. Murray, D. Renshaw, B. Dhillon, A. Ohtori, Y. Inoue, J.G. Terry, and A.J. Walton, "Implementation of Wireless Power Transfer and Communications for an Implantable Ocular Drug Delivery System," *IET Nanobiotechnology*, vol. 2, pp. 72-79, 2008.

[70] Y. Yang, Y. Huang, H. Liao, T. Wang, P. Huang, C. Lin, Y. Wang, and S. Lu, "A Release-On-Demand Wireless CMOS Drug Delivery SoC Based on Electrothermal Activation Technique," *Proceeding IEEE Solid-State Circuit*, San Francisco, CA, USA, Feb. 8-12, 2009, pp. 288-290.

[71] P. Gao, K. Yao, X. Tang, X. He, S. Shannigrahi, Y. Lou, J. Zhang, and K. Okada, "A Piezoelectric Micro-Actuator with a Three-Dimensional Structure and Its Micro-fabrication," *Sensors and Actuators A: Physical*, vol. 130-131, pp. 491–496, 2006.

[72] Z. H. Wang, W. G. Zhu, and X. Yao, "$d_{31}$ Type Inplane Bending Multilayer Piezoelectric Microactuators - a Design Concept and Its Applications," *Sensors and Actuators A: Physical*, vol.101, pp. 262-268, 2002.

[73] R. Maeda, J. Tsaur, S. Lee, and M. Ichiki, "Piezoelectric Microactuator Devices," *Journal of Electroceramics*, vol. 12, pp. 89-100, 2004.

[74] D. C. Roberts, H. Li, J. L. Steyn, O. Yaglioglu, S. M. Spearing, M. A. Schmidt, and N. W. Hagood, "A Piezoelectric Microvalve for Compact High-Frequency, High-Differential Pressure Hydraulic Micropumping Systems," *Journal of Microelectromechanical System*, vol.12(1), pp. 91-92, 2003.

[75] D. Piyabongkarn, Y. Sun, R. Rajamani, A. Sezen, and B. J. Nelson, "Travel Range Extension of a MEMS Electrostatic Microactuator," *IEEE Transaction on Control System Technology*, vol. 13 (1), pp.138-146, 2005.

[76] C. Huang, C. Christophorou, K. Najafi, A. Naguib, and H. M. Nagib, "An Electrostatic Microactuator System for Application in High-Speed Jets," *Journal of Microelectromechanical System*, vol. 11(3), 222 -235, 2002.

[77] J. Muthuswamy, M. Okandan, T. Jain, and A. Gilletti, "Electrostatic Microactuators for Precise Positioning of Neural Microelectrodes," *IEEE Transaction on Biomedical Engineering*, vol. 52(10), 1748–1755, 2005.

[78] G. K. Lau, J. F. Goosen, F. van Keulen, T. Chu Duc, and P. M. Sarro, "Powerful Polymeric Thermal Microactuator with Embedded Silicon, Microstructure," *Applied Physics Letters*, vol. 90, pp. 214103-1–214103-3, 2007.

[79] Y. Zhang and D. W. J. Lee, "Design and Modeling of an Efficiency Horizontal Thermal Microactuator with Integrated Piezoresistors for Precise Control," *Journal of Nanoscience and Nanotechnology*, vol. 10 (5), pp. 3311-3315, 2010.

[80] C. H. Ahn and M. G. Allen, "A Fully Integrated Surface Micromachined Magnetic Microactuator with a Multilevel Meander Magnetic Core," *Journal of Microelectromechanical System*, vol. 2 (1), pp. 15- 22, 1993.

[81] L. K. Lagorce, O. Brand, and M. G. Allen, Magnetic Microactuators Based on Polymer Magnets," *Journal of Microelectromechanical System*, vol. 8 (1), pp. 2-9, 1999.

[82] S. Park, K. Koo, S. M. Bang, J. Y. Park, S. Y. Song, and D. Cho, "A Novel Microactuator for Microbiopsy in Capsular Endoscopes," *Journal of Micromechanics and Microengineering*, vol. 18, pp. 025032-1– 025032-9, 2008.

[83] S. C. Shen, A New Cymbal-Shaped High Power Microactuator for Nebulizer Application, *Microelectronic Engineering*, vol. 87(2), pp. 89-97, 2010.

[84] H. Yaguchi and K. Tsurumoto, "Wireless-Type Magnetic Micro-Actuator Capable of Movement in a Pipe," *Proceeding IEEE on. Magnetics*, Nagoya, Japan, Apr. 4-8, 2005, pp. 1443-1444.

[85] H. Yaguchi and S. Sasaki, "Cable-Free Magnetic Micro-Actuator Capable of Movement in a Thin Pipe," *Transaction of Magnetics Society Japan*, vol.5 (1), pp. 43-48, 2005.

[86] B. Kim, M.G. Lee, Y.P. Lee, Y. Kim, and G. Lee, "An Earthworm-Like Micro Robot using Shape Memory Alloy Actuator," *Sensors and Actuators A physical*, vol. 125 pp. 429-437, 2006.

[87] E. T. Jara, T. J. Eduardo, and D. Rus, Flexible Actuator Based on Shape Memory Alloy Sheet, *US Patent* Application No. 20110173970, 2011.

[88] E. Torres-Jara, K. Gilpin, J. Karges, R. J. Wood, and D. Rus, "Compliant Modular Shape Memory Alloy Actuators," *IEEE Robotics Automation Magazine,* vol. 17, pp.78-87, 2010.

[89] Z. Wang, G. Hang, J. Li, Y. Wang, and K. Xiao, "A Micro-Robot Fish with Embedded SMA Wire Actuated Flexible Biomimetic Fin," *Sensors and Actuators A physical*, vol. 144, pp. 354–360, 2008.

[90] D. W. Dissanayake, S.F. Al-Sarawi, and D. Abbott, "Electrostatic Microactuator Design using Surface Acoustic Wave Devices," *Smart Sensor Technology*, vol. 20, pp. 139-151, 2008.

[91] P. Basset, A. Kaiser, P. Bigotte, D. Collard, and L. Buchaillot, "A Large Stepwise Motion Electrostatic Actuator for A Wireless Microrobot," *Proceeding IEEE MEMS*, Las Vegas, NV, USA, Jan. 20-24, 2002, pp. 606-609.

[92] M. Hafez, Y. Bellouard, T. Sidler, R. Clavel, and R. Salathe, "Local Annealing of Shape Memory Alloys using Laser Scanning and Computer Vision," *Proceeding* SPIE *International Symposium on Laser Precision Microfabrication*, Saitama, Japan, June 14-16, 2000**,** pp. 160-163.

[93] G. K. Knopf, "Optically Driven Shape Memory Alloy Microactuators," *Proceeding SPIE International Society Optical Engineering, Intelligent Manufacturing*, Providence, RI, USA, Oct. 29-30, 2003, pp. 22–29.

[94] S. S. Zaidi, F. Lamarque, J. Favergeon, O. Carton, C. Prelle, M. Lejeune, and A. Zeinert, "Wavelength Dependent Remote Power Supply for Shape Memory Alloy," *Journal of Intelligent Material, System and Structure*, vol. 21, pp. 175-184, 2010.

[95] K. Clements, "Wireless Technique for Microactivation," *US Patent* No. 6, 588, 208, 2003.

[96] C. Liu, D. Zhang, and H. Zhang, "Experimental Study of Novel Microactuator Based on Photothermal Expansion," *Optoelectronics Letters*, vol. 4, pp. 89-91, 2008.

[97] L. H. Han and S. Chen, "Wireless Bimorph Micro-Actuators by Pulsed Laser Heating," *Sensors and Actuators A physical*, vol. 121 (1), pp. 35-43, 2005.

[98] O. J. Sul, M. R. Falvo, R. M. Taylor II, S. Washburn, and R. Superfine, "Thermally Actuated Untethered Impact-Driven Locomotive Microdevices," *Applied Physics Letters*, vol. 89, pp. 203512-1–203512-3, 2006.

[99] K. Vollmers, D. R. Frutiger, B. E. Kratochvil, and B. J. Nelson, “Wireless Resonant Magnetic Microactuator for Untethered Mobile Microrobots,” *Applied Physics Letters*, vol. 92, pp. 144103-1–144103-3, 2008.

[100] T. Bourouina, A. Garnier, and H. Fujita, “Magnetostrictive Microactuators and Application to Two-Dimensional Optical Scanners,” *Japan Journal of Applied Physics*, vol. 41, pp. 1608-1613, 2002.

[101] C. S. Troisi, M. Knaflitz, E. S. Olivetti, L. Martino, and G. Durin, “Fabrication of New Magnetic Micro-Machines for Minimally Invasive Surgery,” *IEEE Transaction on Magnetics*, vol. 44 (11), pp. 4499-4491, 2008.

[102] N. Miki and I. Shimoyama, “Soft-Magnetic Rotational Microwings in an Alternating Magnetic Field Applicable to Microflight Mechanisms,” *Journal of Microelectromechanical System*, vol. 12 (2), pp. 221-227, 2003.

[103] M. P. Kummer, J. J. Abbott, B. E. Kratochvil, R. Borer, A. Sengul, and B. J. Nelson, “OctoMag: An Electromagnetic System for 5-DOF Wireless Micromanipulation,” *IEEE Transaction on Robotics*, vol. 26 (6), pp. 1006-1617, 2010.

[104] K. B. Yesin, K. Vollmers, and B. J. Nelson, “Modeling and Control of Untethered Biomicrorobots in a Fluidic Environment using Electromagnetic Fields,” *International Journal on Robotics Research*, vol. 25, pp. 527-536, 2006.

[105] J. B. Mathieu, G. Beaudoin, and S. Martel, “Method of Propulsion of a Ferromagnetic Core in the Cardiovascular System through Magnetic Gradients Generated by an MRI System,” *IEEE Transaction on Biomedical Engineering*, vol. 53 (2), pp.292-299, 2006.

[106] S. Hollar, A. Flynn, S. Bergbreiter, and K. S. J. Pister, “Robot Leg Motion in a Planarized-SOI, Two-Layer Poly-Si Process,” *Journal of Microelectromechanical System*, vol.14 (4), pp. 725-740, 2005.

[107] S. Takeuchi and I. Shimoyama, “Selective Drive of electrostatic Actuators using Remote Inductive Powering,” *Sensors and Actuators A: Physical*, vol.95, pp. 269-273, 2002.

[108] B. R. Donald, C. G. Levey, C. D. McGray, I. Paprotny, and D. Russ, “An Untethered, Electrostatic, Globally Controllable MEMS Micro-Robot,” *Journal of Microelectromechanical System*, vol.15 (1), pp. 1–15, 2006.

[109] R. S. Fearing, “Powering 3 Dimensional Microrobots: Power Density Limitations,” *in Tutorial on Micro Mechatronics and Micro Robotics ICRA*, 1998.

[110] M. Tanaka, F. Wang, K. Abe, Y. Arai, H. Nakagawa, and S. Chonan, “A Closed-Loop Transcutaneous Power Transmission System with Thermal Control for Artificial Urethral Valve Driven by SMA Actuator,” Journal *of Intelligent Material, System, and Structure*, vol. 17, pp. 779-786, 2006.

[111] M. Tanaka, T. Sakamoto, F. Wang, T. Namima, Y. Tanahashi, and S. Chonan, “Development of Mechanical SMA Urethral Valve with Transcutaneous Energy Transmission System,” *International Journal of Applied Electromagnetics and Mechanics*, vol. 14, pp. 381-390, 2001.

[112] D. Clausi, H. Gradin, S. Braun, J. PeirsI, G. Stemme, D. Reynaerts, and W. van der Wifngaart, “Microactuation Utilizing Wafer-Level Integrated SMA Wires,” *Proceeding IEEE MEMS*, Sorrento, Italy, 25-29 Jan, 2009, pp.1068-1070.

[113] S. Braun, N. Sandström, and G. Stemme, “Wafer-Scale Manufacturing of Bulk Shape-Memory-Alloy Microactuators Based on Adhesive Bonding of Titanium-Nickel Sheets to Structured Silicon Wafers,” *Journal of Micromechanical System*, vol. 18, pp. 1309-1317, 2009.

[114] F. Niklaus, P. Enoksson, E. Kalvesten, and G. Stemme, “Low-Temperature Full Wafer Adhesive Bonding,” *Journal of Micromechanics and Microengineering*, vol. 11, pp. 100-107, 2001.

[115] H. S. Noh, K. S. Moon, C. Cannon, P. J. Hesketh, and C. P. Wong, “Wafer Bonding using Microwave Heating of Parylene Intermediate Layers,” *Journal of Micromechanics and Microengineering*, vol. 14, pp. 625-631, 2004.

[116] Y. K. Kim, E. Y. Kim, S. W. Kim, and B. K. Ju, “Low Temperature Epoxy Bonding for Wafer Level MEMS packaging,” *Sensors and Actuators A physical*, vol. 143, pp. 323-328, 2008.

[117] T. Pan, H. Yang, S.C. Shen, M. C. Chou1 and H. P. Chou, “A Low-Temperature Wafer Bonding Technique using Patternable Materials,” *Journal of Micromechanics and Microengineering*, vol. 12, pp. 611–615, 2002.

[118] A. Jourdain, P. D. Moor, K. Baert, I. D. Wolf, and H. A. C. Tilmans, “Mechanical and Electrical Characterization of BCB as a Bond and Seal Material for Cavities Housing

(RF) MEMS Devices," *Journal of Micromechanics and Microengineering*, vol. 15, pp. 89-96, 2005.

[119] Y. H. Joung and M. G. Allen, "Inter-Substrate Microstructure Formation by Electroplating Bonding Technology," *Journal of Micromechanics and Microengineering*, vol. 18**,** pp. 1-12, 2008.

[120] N. Tesla, "The Transmission of Electrical Energy Without Wires as a Means for Furthering Peace," *Electrical World and Engineer*, p. 21, 1905.

[121] A. Kurs et al., "Wireless Power Transfer via Strongly Coupled Magnetic Resonances," *Science*, vol. 317 (5834), pp. 83-88, 2007.

[122] T. Deyle and M. Reynolds, "Surface Based Wireless Power Transmission and Bidirectional Communication for Autonomous Robot Swarms," *Proceeding IEEE Robotics and Automations*, pp. 1036-1041. 2008.

[123] J. Taylor, Z.N. Low; J. Casanova, and J. Lin, "A Wireless Power Station For Laptop Computers," *IEEE Radio and Wireless Symposium* (RWS), LA, USA, 10-14 Jan. 2010, pp. 625-628.

[124] P. Sample, T. Meyer, and J. Smith, "Analysis, Experimental Results, and Range Adaptation of Magnetically Coupled Resonators for Wireless Power Transfer," *IEEE Transaction on Industrial Electronics*, vol. 58(2), pp. 544-554, 2011.

[125] C. E. Weitzel, "RF Power Devices for Wireless Communications," *IEEE Microwave Symposium*, WA, USA, 2-7 Jun, 2002, pp. 285-288.

[126] R. Puers, "Linking Sensors with Telemetry: Impact on The System Design," *Proceeding IEEE Transducers '95/Eurosensors IX*, Stockholm, Sweden, 25-29 June, 1995, pp. 47-50.

[127] M. Nardin and K. Najafi, "A Multichannel Neuromuscular Microstimulator with Hi-Directional Telemetry," *Proceeding IEEE Transducers '95/Eurosensors IX*, Stockhohn, Sweden, 25-29 June, 1995, pp. 59-62.

[128] R. Kadefors, E. Kaiser, and I. Petersen, "Energizing Implantable Transmitters by Means of Coupled Inductance Coils," *IEEE Transaction on Biomedical Engineering*, vol. 16, pp. 177-183, 1969.

[129] G. Wang, W. Liu, M. Sivaprakasam, M. Humayun, and J. Weiland, "Power Supply Topologies for Biphasic Stimulation in Inductively Powered Implants," *Proceeding*

*IEEE International Symposium on Circuits and Systems*, vol. 3(12), pp. 2743–2746, 2005.

[130] P. Li, J. Principe, and R. Bashirullah, “A Wireless Power Interface For Rechargeable Battery Operated Neural Recording Implants,” *Proceeding IEEE Engineering Medicine Biology Society*, New York City, USA, Aug 30-Sept 3, 2006, pp. 6253–6256.

[131] K. Finkenzeller, *RFID Handbook: Fundamentals and Applications in Contactless Smart Cards and Identification*, Wiley, Sussex, UK, 2003.

[132] B. Jiang, J. R. Smith, M. Philipose, S. Roy, K. Sundara-Rajan, and A. V. Mamishev, “Energy Scavenging for Inductively Coupled Passive RFid Systems,” *IEEE Transaction on Instrumentation and Measurements*, vol. 56 (1), pp. 118–125, 2007.

[133] C. R. Neagu, H. V. Jansen, A. Smith, J. G. E. Gardeniers, and M. C. Elwenspoek, “Characterization of a Planar Microcoil for Implantable Microsystems,” *Sensors and Actuators A: Physical*, vol. 62, pp. 599-611, 1997.

[134] F. Hendriks, “Design of Planar coils of Minimum Resistance for Magnetic Recording Devices,” *15th Annual Workshop on Mathematical Problems in Industry*, University of Delaware, DE, USA, June 7-11, 1999.

[135] T. Munsat, W. M. Hooke, S. P. Bozeman, and S. Washburn, “Two New Planar Coil Designs for a High Pressure Radio Frequency Plasma Source,” *Applied Physics Letters*, vol. 66, pp. 2180-1–2180-3, 1995.

[136] K. Yanagisawa, A. Tago, T. Ohkubo, and H. Kuwano, “Magnetic Micro-Actuator,” *Proceeding IEEE MEMS*, Nara, Japan, 1991, pp. 120-124.

[137] H. Guckel, K. J. Skrobis, T. R. Christenson, J. Klein, S. Han, B. Choi, E. G. Novell, and T. W. Chapman, “On the Application of Deep X-Ray Lithography with Sacrificial Layers to Sensor and Actuator Construction,” *Journal of Micromechanics and Microengineering*, vol. 1(4), pp. 135-138, 1991.

[138] B. Wagner, M. Kreutzer, and W. Benecke, “Linear and Rotational Magnetic Micromotors Fabricated using Silicon Technology,” *Proceeding IEEE MEMS*, 1992, pp. 183-189.

[139] C. P. Yue, C. Ryu, J. Lau, T. H. Lee, and S. S. Wong, “A Physical Model for Planar Spiral Inductors on Silicon,” *Proceeding IEEE International Electron Devices Meeting*, San Francisco, CA, 1996, pp. 155-158.

[140] R. B. Merrill, T. W. Lee, H. You, R. Rasmussen, and L. A. Moberly, “Optimization of High Q Integrated Inductors for Multilevel Metal CMOS,” *Proceeding IEEE International Electron Devices Meeting*, Washington, USA, 1995, pp. 3871-3874.

[141] S. S. Mohan, M. M. Hershenson, S. P. Boyd, and T. H. Lee, “Simple Accurate Expressions for Planar Spiral Inductances,” *IEEE Journal of Solid-State Circuits*, 34(10), pp. 1419-1424, 1999.

[142] H. M. Greenhouse, “Design of Planar Rectangular Microelectronic Inductors,” *IEEE Transaction on Parts, Hybrids and Packaging*, vol. PHP-10, pp.101-109, 1974.

[143] H. A. Wheeler, “Simple Inductance Formulas for Radio Coils,” *Proceeding IRE*, Oct. 1928, vol. 16(10), pp. 1398-1400.

[144] V. Sridhar, “A micromachined Inductive Sensor using Folded Flex-Circuit Structures and its Wireless Telemetry Applications,” *Master’s thesis*, University of British Columbia, Vancouver, Canada, 2008.

[145] H. Sun, Z. Liu, J. Zhao, L. Wang, and J. Zhu, “The Enhancement of Q-Factor of Planar Spiral Inductor with Low-Temperature Annealing,” *IEEE Transaction on Electron Devices*, vol. 55, pp. 931-936, 2008.

[146] S. Brugger and O. Paul, “Field-Concentrator-Based Resonant Magnetic Sensor With Integrated Planar Coils,” *Journal of Microelectromechanical System*, vol. 18(6), pp. 1432-1441, 2009.

[147] A. Eroglu, “Planar Inductor Design for High Power Applications,” *Progress In Electromagnetics Research B*, vol. 35, pp. 53-67, 2011.

[148] A. Kids, V. Fernandex, and M. A. M Gijj, “Planar Coi1-Based Microsystem for the Long-Range Transport of Magnetic Beads,” *Proceeding IEEE Transducers*, Boston, June 8-12, 2003, pp. 292-295.

[149] Z. N. Low, R. Chinga, R. Tseng, and J. Lin, “Design and Test of a High Power High-Efficiency Loosely Coupled Planar Wireless Power Transfer System,” *IEEE Transactions on Industrial Electronics*, vol. 56(5), pp. 1801-1812, 2009.

[150] J. Casanova, Z. N. Low, and J. Lin, “A Loosely Coupled Planar Wireless Power System for Multiple Receivers,” *IEEE Transactions on Industrial Electronics*, vol. 56(8), pp. 3060-3068, 2009.

[151] P. W. Harrison and G. H. Rayner, “A Primary Standard of Mutual Inductance,” *Metrologia*, vol. 3(1), pp.1-12, 1967.

[152] Z. Li, Z. Zhang, Q. He, Y. Fu, J. Zhao, B. Han, S. Li, J. Lan, and C. Li, "A Compensation Method to Measure the Mutual Inductance at Low Frequency," *IEEE Transaction of Instruments and Measurement*, vol. 60(7), pp. 2292-2297, 2011.

[153] D. R. Patrick and S. W. Fardo, *Electricity and Electronics Fundamentals*, 2nd Edn. Fairmount Press, GA, USA, 2008.

[154] E. H. Sarraf, G.K. Wong, and K. Takahata, "Frequency-Selectable Wireless Actuation of Hydrogel using Micromachined Resonant Heaters Toward Implantable Drug Delivery Application", *Proceeding IEEE Transducers*, Denver, CO, USA, June 21-25, 2009, pp. 1525-1528.

[155] S. D. Senturia, *Microsystem Design*, Kluwer Academic Publishers, New York, 2001.

[156] A. D. Kraus, A. Bar-Cohen, *Thermal Analysis and Control of Electronic Equipment*, Hemisphere, New York, 1983.

[157] J. Welty, C. E. Wicks, R. E. Wilson, and G. L. Rorrer, *Fundamentals of Momentum*, *Heat*, *and Mass Transfer*, 5th Ed. Wiley, New Jersey, USA, 2008.

[158] R. W. Lewis, P. Nithiarasu and K. N. Seetharamu, *Fundamentals of the Finite Element Method for Heat and Fluid Flow*, Wiley, Sussex, UK, 2004.

[159] McAdams, H.William, *Heat Transmission*, 3rd Ed., McGraw-Hill, New York, USA, 1954.

[160] F. Kreith, *The CRC Handbook of Thermal Engineering*, CRC Press, Florida, USA, 2000.

[161] K. J. Puttlitz and P. Totta, *Area Array Interconnection Handbook*, Kluwer Academic publisher, Massachusetts, USA, 2001.

[162] M. F. Modest, *Radiative Heat Transfer*, 2nd Ed. Academic Press, Massachusetts, USA, 2003.

[163] M. Fadlisyah, E. Ábrahám, D. Lepri, and P. C. Ölveczky, "A Rewriting-Logic-Based Technique for Modeling Thermal Systems," *Proceeding of RTRTS'10, EPTCS*, vol. 36, 2010, pp. 82-100.

[164] Dupond, "Mechanical and Thermal Property of Polyimide Sheet", http://www2.dupont.com/Kapton/en_US/assets/downloads/pdf/summaryofprop.pdf.

[165] J. Bird, *Electrical and Electronic Principles and Technology*, 4th Ed., Newnes, Hong Kong, China, 2010.

[166] M. S. Mohamed Ali and K. Takahata, "Frequency-Controlled Wireless Shape-Memory-Alloy Microactuators Integrated using an Electroplating Bonding Process," *Sensors and Actuators A: Physical*, 163(1), pp 363-372, 2010.

[167] M. S. Mohamed Ali and K. Takahata, "A Wirelessly Controlled Shape-Memory-Alloy MEMS Gripper Microfabricated using an Electroplating-Based Bonding Process," *Solid-State Sensors, Actuators and Microsystems Workshop*, Hilton Head, SC, USA, June 6-10, 2010, pp. 396-399.

[168] T. Masaki, K. Kawata, and T. Masuzawa, Micro Electro-Discharge Machining and Its Applications, *Proceeding IEEE MEMS*, Napa Valley, CA, USA, February 11-14, 1990, pp. 21-26.

[169] K. Takahata, *Micro-Electro-Discharge Machining Technologies for MEMS in Micro Electronic and Mechanical Systems*, Ed. K. Takahata, IN-TECH, 2009, ISBN 978-953-307-027-8.

[170] B. A. Davis, *Investigation of the Thermomechanical Response of Shape Memory Alloy Hybrid Composite Beams*, NASA/CR-2005-213929.

[171] C. H. Seah, S. Mridha, L. H. Chan, "Adhesive Strength of Electroplated Copper Films," *Journal of Material Processing Technology*, vol. 114, pp. 252-256, 2001.

[172] T. Hara, M. Uchida, and M. Fujimoto, Measurement of Adhesion Strength in Copper Interconnection Layers, *Electrochemical Solid State Letter*, vol. 7, pp. 28-30, 2004.

[173] M.S. Mohamed Ali and K. Takahata, "Wireless Microfluidic Control with Integrated Shape-Memory-Alloy Actuators Operated by Field Frequency Modulation," *Journal of Micromechanics and Microengineering*, vol. 21, pp. 075005-1– 075005-10, 2011.

[174] M. S. Mohamed Ali and K. Takahata, "Selective RF Wireless Control of Integrated Bulk-Micromachined Shape-Memory-Alloy Actuators and Its Microfluidic Application," *Proceeding IEEE MEMS*, Cancun, Mexico, Jan 23-27, 2011, pp 1269-1272.

[175] A. Persat, R. D. Chambers, and J. G. Santiago, "Basic Principles of Electrolyte Chemistry for Microfluidic Electrokinetics: part I. Acid-Base Equilibria and pH Buffers," *Lab on Chip*, vol. 9, pp. 2437-2453, 2009.

[176] M. S. Mohamed Ali, B. Bycraft, C. Schlosser, B. Assadsangabi, and K. Takahata, "Out-of-Plane Spiral- Coil Inductor Self-Assembled by Locally Controlled Bimorph Actuation," *Micro and Nano Letters*, vol. 6, pp. 1016-1018, 2011.

[177] S. Zinn and S.L. Semiatin, "Coil Design and Fabrication: Basic Design and Modifications," *Heat Treating Magazine*, pp. 32–36, 1998.

[178] A. D. Hennis and K. D. Wise, "A Double-Sided Single-Chip Wireless Pressure Sensor," in *Proceeding IEEE MEMS*, Las Vegas, NV, Jan. 2002, pp. 252–255.

[179] J. C. Butler, A. J. Vigliotti, F. W. Verdi, and S. M. Walsh, "Wireless, Passive, Resonant-Circuit, Inductively Coupled, Inductive Strain Sensor," *Sensors and Actuators A: Physical*, vol. 102, pp. 61-66, 2002.

[180] Y. Wen, P. Li, J. Yang, and M. Zheng, "Detecting and Evaluating the Signals of Wirelessly Interrogational Passive SAWResonantor Sensors," *IEEE Sensors Journal*, vol. 4(6), pp. 828-836, 2004.

[181] M. Hamsch, R. Hoffmann, W. Buff, M. Binhack, and S. Klett, "An Interrogation Unit for Passive Wireless SAW Sensors Based on Fourier Transform," *IEEE Transaction on Ultrasonic, Ferroelectric and Frequency Control*, vol. 51(11), pp. 1449-1456, 2004.

[182] Sajeeda and T. J. Kaiser, "Passive Telemetric Readout System," *IEEE Sensors Journal*, vol. 6(5), pp. 1340-1345, 2006.

[183] E. L. Tan, W. N. Ng, R. Shao, B. D. Pereles, and K. G. Ong, "A Wireless, Passive Sensor for Quantifying Packaged Food Quality," *Sensors Journal*, vol. 7, pp. 1747-1756, 2007.

[184] V. Sridhar and K. Takahata, "A hydrogel-based passive wireless sensor using a flex-circuit inductive transducer," *Sensors and. Actuators: A Physical*, vol. 155(1), pp. 58-65, 2009.

[185] B. J. Peterson, A. V. Olson, T. J. Kaiser, "A Wireless Sensor Interrogator Design for Passive Resonant Frequency Sensors Using Frequency Modulation Spectroscopy," *IEEE Sensors Journal*, vol.10(12), pp. 1884-1890, 2010.

[186] S. Rahimi, E. H. Sarraf, G. K. Wong, K. Takahata, "Implantable Drug Delivery Device Using Frequency-Controlled Wireless Hydrogel Microvalves," *Biomedical Microdevices*, vol. 13(2), 267-277, 2011.

# Appendix A

# Out-of-Plane Spiral-Coil Inductor Self-Assembled By Locally Controlled Bimorph Actuation

In this section[4], a fabrication method of 3- dimensional (3D) microcoil is presented based on the localized bimorph actuation method that reported in Chapter 5. The design, fabrication and the results are reported.

## Introduction

The fabrication of 3D microcoil inductors has attracted considerable interest in recent years for a variety of applications including radio communication [1], magnetic field sensor [2], and magnetic resonant imaging [3]. Although 2D planar coils are still being widely applied in these areas due to the simple methods needed to fabricate them, the resulting devices often suffer from inhomogeneous magnetic fields and small Q-factors which limit the performance of the systems in which they are used [4]. Furthermore, planar coils have a fixed inductance value which is dependent on how the coils are designed in these two dimensions. Any desired change in inductance requires a new coil with new dimensions. In integrated circuits (ICs) and Microsystems, stringent size and dimension constraints make this situation unfavourable. 3D spiral coils offer a potential solution to this problem. They can be selected

[4] A version of this chapter has been published in a peer-reviewed journal (Reused with permission from "M.S. Mohamed Ali, B. Bycraft, C. Schlosser, B. Assadsangabi, and K. Takahata, 'Out-of-plane spiral-coil inductor self-assembled by locally controlled bimorph actuation,' *Micro Nano Letter* vol. 6, pp. 1016-1018, 2011", Copyright 2011, IET) [178].

for a system which requires different levels of inductance without varying the base dimension of the device. Fabrication methods for 3D inductors have been extensively investigated through the use of MEMS technologies. They include folding/deforming planar structures [5, 6], LIGA [7], electrodeposition overflow [8], multilayer stacking [9], wire bonding [4], bimorph [10], and direct writing approaches [11-13]. Some of them were utilized to fabricate variable micro inductors [9, 10]. However, most of these techniques require special apparatus and complex set-ups, manual steps, and/or many photolithographic steps that are time consuming and expensive. Microfabrication of 3D coil inductors has continued to be a challenging task.

In this section, we report a method to manufacture out-of-plane, 3D spiral-coil inductors with controlled heights and inductances in a self-assembling manner based on local thermal actuation of patterned bimorph microstructures. The fabrication approach provides more freedom in defining the inductance of the coils, without affecting the on-chip space occupied by them, for various applications including those noted earlier. The fabrication is based on standard IC/MEMS processes, enabling wafer-level production and circuit integration of the inductors at low costs.

## Principle and Design

In the developed method, 3D inductors are created by permanently displacing planar spiral-coil structures using locally defined bimorph actuation (Figure A1(a)). The planar coils are deformed out-of-plane, producing a change in their total inductance by varying their mutual inductance, which is dependent on the distance between the turns of the coil. The deformation is achieved as a result of the difference between the CTE of Cu and Cr (16.5 and

4.9 μm·m$^{-1}$·°C$^{-1}$, respectively) that form the bimorph. This difference causes bending in the regions where the Cr is patterned on each segment of the spiral coil (Figure A1(b)) when the structure is annealed.

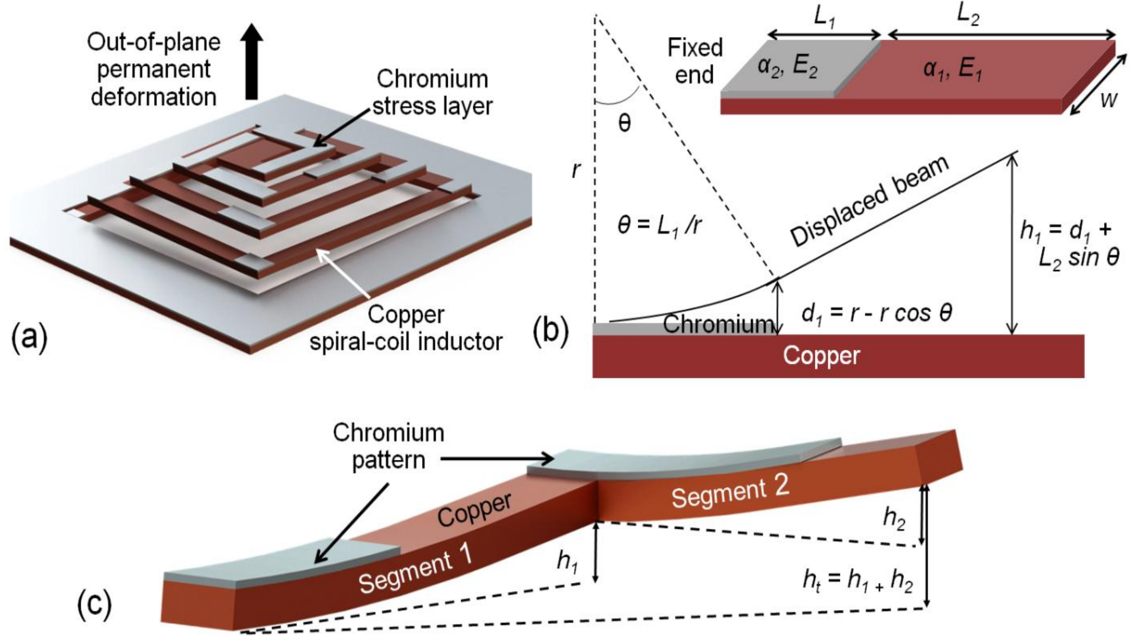


**Figure A1:** Formation of 3D spiral-coil inductor; (a) Overall structure and displacement; (b) Bimorph actuation of single segment; (c) Additive height gain from consecutive segments of the microcoil.

The bent bi-layer section creates an angle between the beam and the base which results in a vertical displacement at the free end of the beam that is proportional to this angle and the beam length. The length of the Cr pattern determines the above angle by forming an arc with the radius *r* (Figure A1(b)), which can be expressed as;

$$\frac{1}{r} = \frac{6w_1 w_2 E_1 E_2 t_1 t_2 (t_1 + t_2)(\alpha_1 - \alpha_2)\Delta T}{\left(w_1 E_1 t_1^2\right)^2 + \left(w_2 E_2 t_2^2\right)^2 + 2w_1 w_2 E_1 E_2 t_1 t_2 \left(2t_1^2 + 3t_1 t_2 + 2t_2^2\right)} \tag{1}$$

where *E* is the Young's modulus of the material, *w* is the width, *t* is the thickness, *α* is CTE, *T*

is the temperature, and the subscripts *1* and *2* denote Cu and Cr respectively. Figure A1(c) displays two consecutive segments, wherein the height gained from the whole section is the sum of both individual segments' displacements ($h_t = h_1 + h_2$). The length of the Cr pattern is increased as the length of the segment decreases to ensure that the coil's turns are uniformly raised upwards when annealed. The Cr layer is positioned over the Cu coil in specific areas to create the desired displacement (Figure A2(a)). The lengths of the Cr patterns were determined with FEA tool COMSOL Multiphysics 3.5 while evaluating the resultant overall displacements (Figure A2(b)).

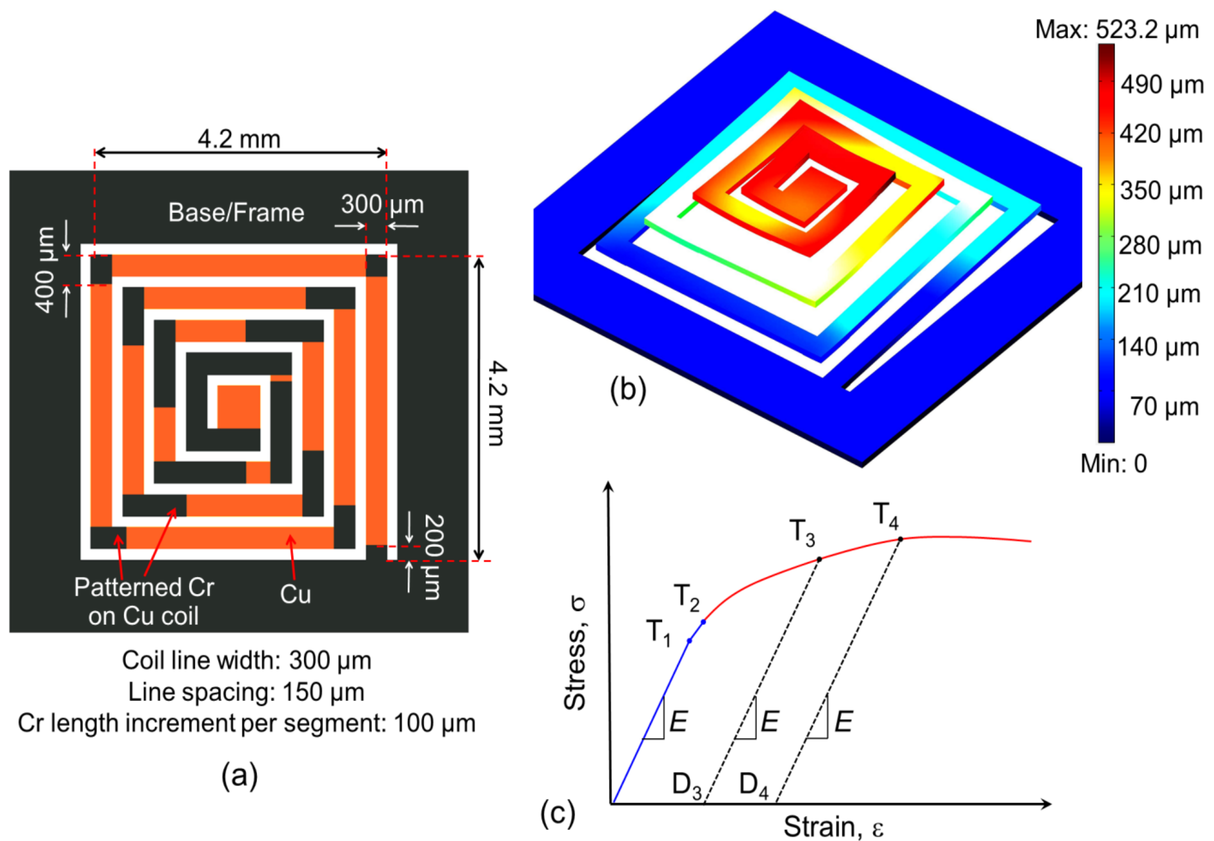


**Figure A2:** Device layout and actuation behavior; (a) Design of the 3D bimorph coil; (b) FEA result showing a ~520-µm out-of-plane displacement at 600 °C provided by Cr stress layer patterned on Cu coil; (c) Stress-strain relationship of the coil material at different $T_H$ values.

The Cr layer is deposited at room temperature, and the coil remains flat in ambient conditions after the deposition. When the coil undergoes annealing, the Cu-Cr bimorph sections bend the coil wires up. The final coil shape is determined by selecting annealing temperature, $T_a$, to control the amount of plastic deformation in the coil. This process is depicted in Figure A2(c), where $T_1$ is the temperature at the proportionality limit, and $T_2$ is the temperature needed to reach the yield strength of the material. When $T_H < T_2$, the coil structure remains in the elastic region and will return to its initial position when the device is brought back to room temperature. $T_3$ and $T_4$ are two examples of temperatures that lead to plastic deformations in the coil structures as the corresponding stresses exceed the yield strength of the material. If these temperatures are defined as $T_H$, permanent displacements of $D_3$ and $D_4$ will occur, providing two different final 3D shapes in the coil.

## Fabrication

Figure A3 illustrates the fabrication process for the 3D spiral-coil inductor (except the final annealing step). The process begins with the deposition of a 500-nm-thick $SiO_2$ sacrificial layer on a Si wafer via plasma enhanced chemical vapor deposition. A 15-nm-thick Cr adhesive layer and a 100-nm-thick Cu seed layer are then evaporated on the Si substrate. Next, the Cu coil layer with thickness of 25 μm is formed using electroplating on the seed layer. This study utilized μEDM to pattern planar spiral coils in the electroplated layer (Figure A4(a)) – this planar coil formation can also be implemented by Cu electroplating in a photoresist mold that is patterned to have the coil layout [14]. The sacrificial $SiO_2$ and adhesive Cr layers are then wet etched in HF and HCl solutions, respectively, suspending the coil while keeping the base/frame attached to the Si substrate. Next, a 500-nm-thick Cr layer is evaporated on the Cu layer (the coil remains flat at this stage) and then patterned using

photolithography and wet etching (Figure A4(b)). After Cr patterning, the coil is annealed in a furnace for 15 minutes at a pressure of 400 mTorr in nitrogen to transform the coil from planar to 3D. The level of $T_H$ determines the final height, i.e., the inductance of the coil. Wire bonding is used to establish an electrical connection to the center of the coil. Figure A4(c) shows a fabricated sample device.

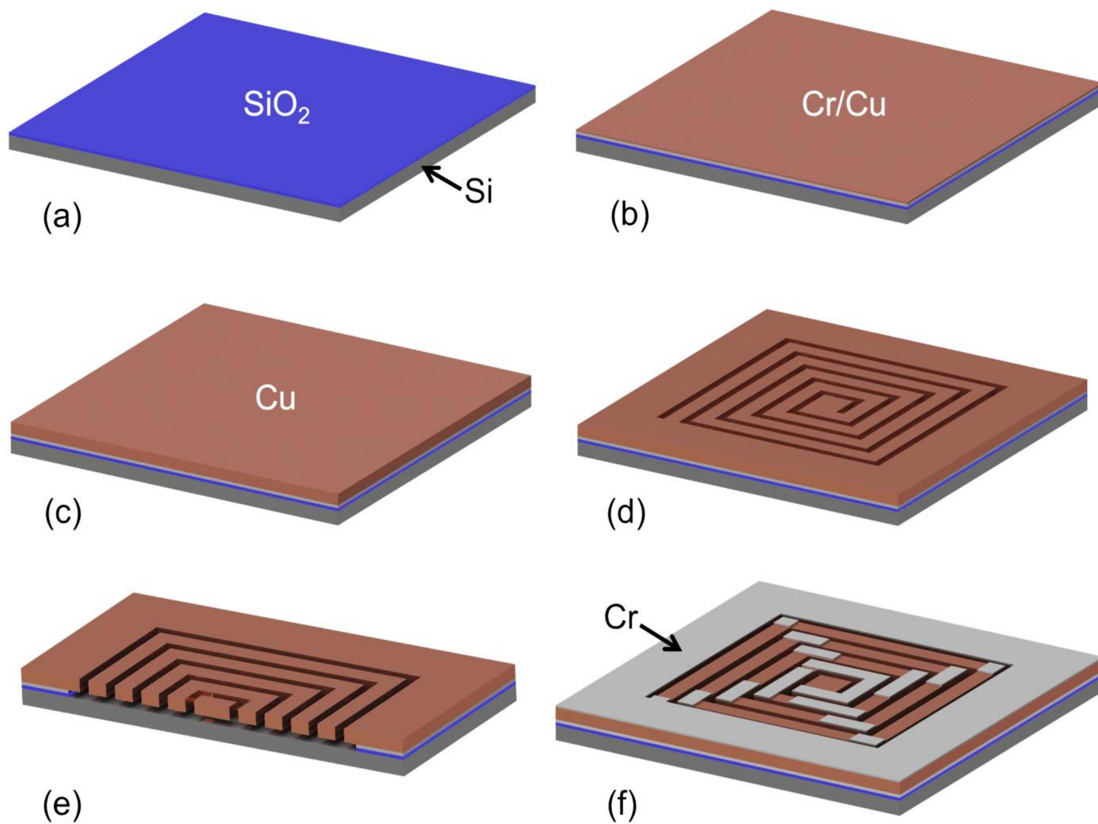


**Figure A3:** Fabrication process; (a) $SiO_2$ deposition; (b) Cr/Cu seed layer deposition; (c) Electroplating of thick Cu layer; (d) Coil formation; (e) Sacrificial etching of $SiO_2$ and Cr layers (cross sectional view); (f) Cr deposition and patterning.

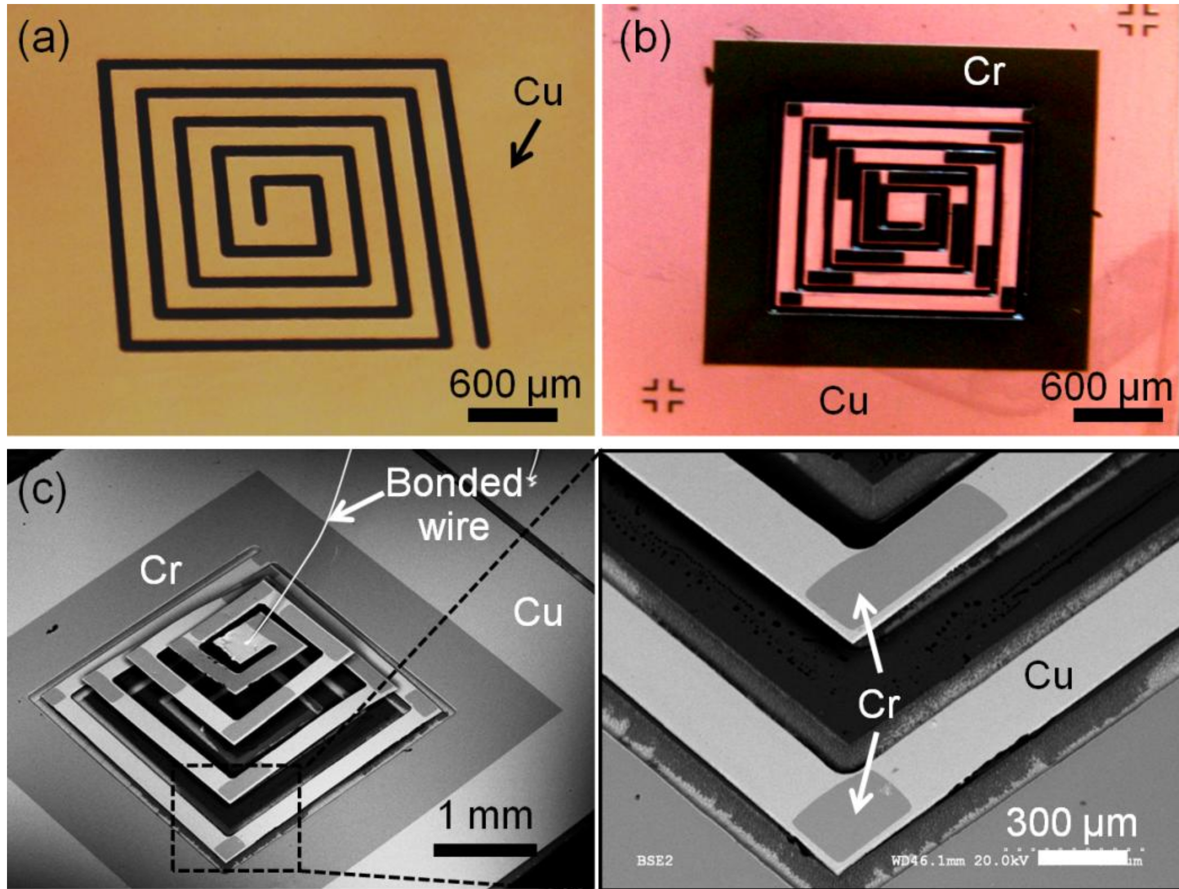


**Figure A4:** Fabricated sample device; (a) Cu coil formed by μEDM; (b) Cr stress layer patterned on the Cu coil prior to annealing process; (c) SEM image of the Cu-Cr bimetallic coil showing its 3D shape resulted by annealing at 800 °C with a close-up image.

## Experimental Results

To evaluate the effect of the annealing on the out-of-plane deformation, the fabricated planar coils were processed at different $T_H$ values. When $T_H \leq 180$ °C, they were observed to deform during the annealing process; however no noticeable deformation in the final structure after cooling was observed, indicating that the deformation was within the elastic region as noted earlier. By contrast, when $T_H = 200$ °C and greater, the coils were plastically deformed and extended vertically to form 3D coil structures (Figure A5(a)). Figure A5(b) shows the

displacements of the coils measured from the base of the coils to their center using a measuring microscope (Nikon MM400), clearly indicating that the plastic deformation of the coils increased with $T_H$ as the thermal stresses increased. It can be seen from Figures A5(b) and A2(b) for the case of $T_H$ = 600 °C that there is a good agreement between the measured displacement (480 μm) and the simulation result (523 μm). Figures A5(b) also plots the change in the inductance of the coils as a function of $T_H$ recorded using an *LCR* meter (HP 4257A) at 10 MHz; a change in inductance of up to 12.2% over the base inductance of 42.8 nH was observed for the temperature range (200-800 °C) used in this test.

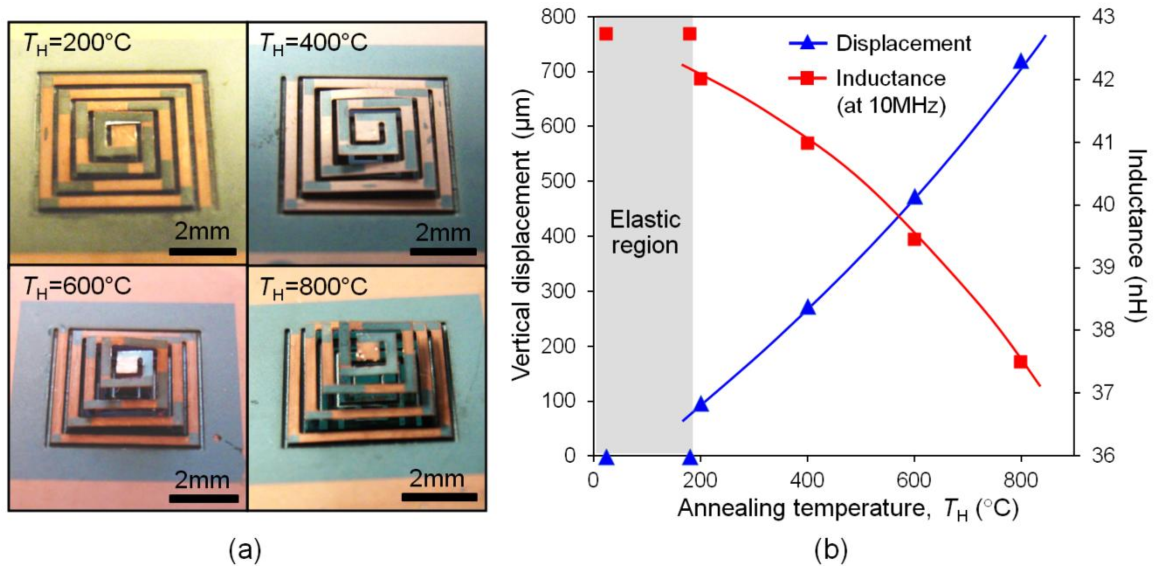


**Figure A5:** Thermal dependence of 3D coil formation; (a) Fabricated coils processed at four different $T_H$ levels showing varying heights; (b) Measured out-of-plane displacement and inductance of the coils as a function of $T_H$.

The frequency characteristics of the fabricated coils were evaluated using a spectrum-impedance analyzer (Agilent 4396B). The measured inductance and Q-factor of the coils completed with four different $T_H$ values as a function of frequency are plotted along with the non-annealed (planar coil) case in Figures A6(a) and A6(b), respectively. The self resonance

of the coils was observed at ~1.2 GHz. Figure A6(b) indicates that the peak of the Q-factor of the planar coil was at ~0.6 GHz and exhibited a shift to ~0.7 GHz with $T_H$ = 800 °C. The Q-factor was measured to increase from 14 to 17 as the coil deformed from planar to 3D (Figure A6(b)). The increase in the Q-factor may be associated with the reduction of eddy currents and parasitic capacitance [15] led by the resultant out-of-plane geometry of the coils.

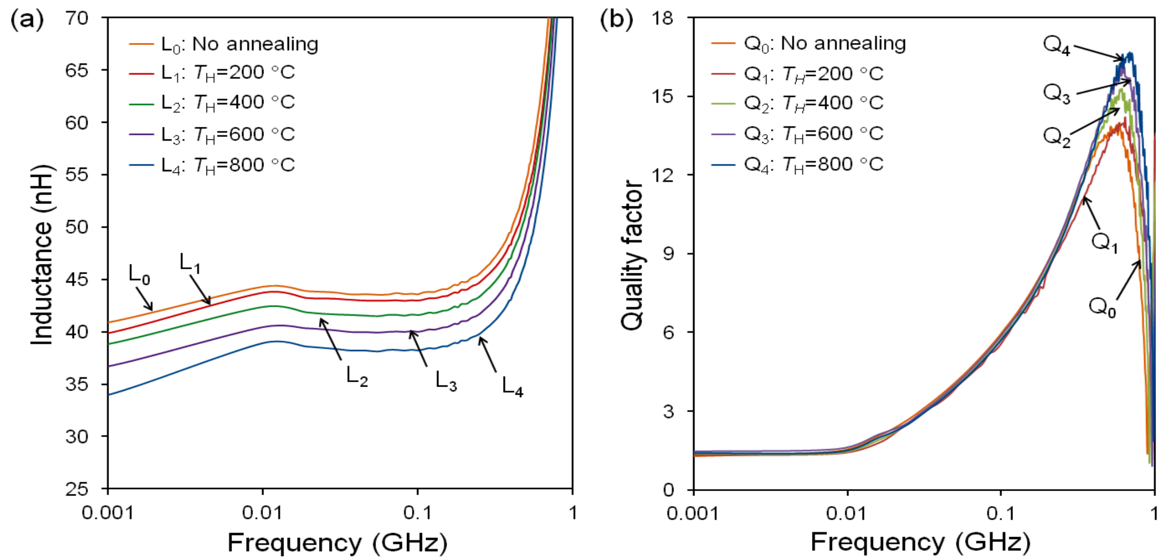


**Figure A6:** Measured frequency dependence; (a) Inductance and (b) Q-factor.

## Conclusion

A novel method to microfabricate 3D inductive coils based on local thermal stressing has been developed and demonstrated with the proof-of-concept devices. The fabrication approach is compatible with typical IC/MEMS manufacturing processes while using $T_H$ levels allowable in the particular processes, and is easily scalable to a wafer-level production. The length of the Cr pattern can be varied to achieve batch formation of the 3D coils with different inductances on a wafer using a single annealing step for their potential monolithic integration with IC/MEMS at low cost. Further miniaturization and optimization of the device will follow.

## References


[1] N. B. Rao and A. N. Chandorkar, “3D Inductor for RF Applications,” *Journal of Microwave and Optical Technology*, vol. 3, pp. 445–449, 2008.

[2] N. Fry, D. P. Makhnovskiy, L. V. Panina, S. I. Sandacci, D. J. Mapps, and M. Akhter, “Off -Diagonal Magnetoimpedance in NiFe-Au-NiFe Layered Film and Its Application to Linear Magnetic Sensors,” *IEEE Transaction on Magnetics*, vol. 40, 3358–3367, 2004.

[3] M. J. K. Klein, T. Ono, M. Esashi, and J. G. Korvink, “RIE of Solenoidal Microcoil Glass Mould with Integrated Sample Container for Micro-MRI,” *Proceeding IEEE MEMS*, 2007, Hyogo, Japan, pp. 345–348.

[4] K. Kratt, V. Badilita, T. Burger, J. G. Korvink, and U. Wallrabe, “A Fully MEMS-Compatible Process for 3D High Aspect Ratio Micro Coils Obtained With an Automatic Wire Bonder,” *Journal of Micromechanics and Microengineering*, vol. 20, 015021, 2009.

[5] M. Gel, S. Takeuchi, and I. Shimoyama, “Fabrication Method for Out-Of-Plane, Micro-coil by Surface Micromachining,” *Sensors and Actuators A: Physical*, vol. 97-98, pp. 702–708, 2002.

[6] T. Fukushige, S. Hata, and A. Shimokohbe, “A MEMS Conical Spring Actuator Array,” *Journal of Microelectromechanical System*, vol. 14, pp. 243–253, 2005.

[7] H. Mekaru, S. Kusumi, N. Sato, M. Shimizu, M. Yamashita, O. Shimada, and T. Hattori, “Fabrication of a Spiral Microcoil using a 3D-LIGA Process,” *Microsystem Technology*, vol. 13, pp. 393-402, 2005.

[8] M. Woytasik, J. P. Grandchamp, E. Dufour-Gergam, E. Martincic, J. P. Gilles, S. Megherbi, V. Lavalley, and V. Mathet, “Fabrication of Planar and Three-Dimensional microcoils on flexible substrates,” *Microsystem Technology*, vol. 12, pp. 973-978, 2006.

[9] P. Park, C. S. Kim, M. Y. Park, S. D. Kim, and H. K. Yu, “Variable Inductance Multilayer Inductor with MOSFET Switch Control,” *IEEE Electron Device Letters*, vol. 25, pp. 144-146, 2004.

[10] S. Chang, S. Sivoththaman, “A Tunable RF MEMS Inductor on Silicon Incorporating an Amorphous Silicon Bimorph in a Low-Temperature Process,” *IEEE Electron Device Letters*, vol. 27, pp. 905-907, 2006.

[11] Y. Kaneko, K. Hashimoto, T. Horiuchi, "Fabrication of Micro-Coils using Laser Scan Lithography on Copper Pipes," *Microelectronic Engineering*, vol. 83, pp. 1249-1252, 2006.

[12] L. O. Sillerud, A. F. McDowell, N. L. Adolphi, R. E. Serda, D. P. Adams, M. J. Vasile, and T. M. Alam, "1H Detection of Superparamagnetic Nanoparticles at 1 T using a Microcoil and Novel Tuning Circuit," *Journal of Magnetic Resonance*, vo. 181, pp. 181-190, 2006.

[13] K. Williams, J. Maxwell, K. Larsson, and M. Boman, "Freeform Fabrication of Functional Microsolenoids, Electromagnets and Helical Springs using High-Pressure Laser Chemical Vapor Deposition," *Proceeding IEEE MEMS*, 1999, Orlando, USA, pp. 232–237.

[14] M. S. Mohamed Ali and K. Takahata, "Frequency-Controlled Wireless Shape-Memory-Alloy Microactuators Integrated using an Electroplating Bonding Process," *Sensors and Actuators A: Physical*, vol. 163, pp. 363-372, 2010.

[15] C. P. Yue and S. S. Wong, "On-Chip Spiral Inductors with Patterned Ground Shields for Si-Based RF IC's," *IEEE Journal of Solid State Circuits*, vol. 33, pp. 743-752, 1998.

# Appendix B

## Parameters used for $T_f$ Calculation in Chapter 2

**Table B1:** Numerical values used for steady state temperature, $T_{ss}$ calculation of coils with different $n$.

| $n$ | $L_c$ (m) | $T_{ss}$ (°C) |
|---|---|---|
| 5 | $5.06\times10^{-5}$ | 50.1 |
| 7 | $5.03\times10^{-5}$ | 66.6 |
| 9 | $5.02\times10^{-5}$ | 71.2 |
| 11 | $5.01\times10^{-5}$ | 79.5 |
| 13 | $5.01\times10^{-5}$ | 62.4 |

**Table B2:** Numerical values used for steady state temperature, $T_{ss}$ calculation of coils with different $l_w$.

| $L_w$ (μm) | $L_c$ (m) | $T_{ss}$ (°C) |
|---|---|---|
| 50 | $4.01\times10^{-5}$ | 52.2 |
| 75 | $4.65\times10^{-5}$ | 61.5 |
| 100 | $5.18\times10^{-5}$ | 69.3 |
| 125 | $6.67\times10^{-5}$ | 76.1 |
| 150 | $7.32\times10^{-5}$ | 84.6 |
| 175 | $8.28\times10^{-5}$ | 95.8 |